Slow-roll corrections in multi-field inflation : a separate universes approach

Karciauskas, Mindaugas

2018-05

Karciauskas , M , Kohri , K , Mori , T & White , J 2018 , ' Slow-roll corrections in multi-field inflation : a separate universes approach ' , Journal of Cosmology and Astroparticle Physics , vol. 2018 , no. 5 , 021 . https://doi.org/10.1088/1475-7516/2018/05/021

http://hdl.handle.net/10138/308366
https://doi.org/10.1088/1475-7516/2018/05/021

The Astrophysical Journal Supplement Series, 234:28 (31pp), 2018 February https://doi.org/10.3847/1538-4365/aaa3dd

The TOP-SCOPE Survey of *Planck* Galactic Cold Clumps: Survey Overview and Results of an Exemplar Source, PGCC G26.53+0.17

Tie Liu[1,2], Kee-Tae Kim[1], Mika Juvela[3], Ke Wang[4], Ken'ichi Tatematsu[5], James Di Francesco[6,7], Sheng-Yuan Liu[8], Yuefang Wu[9], Mark Thompson[10], Gary Fuller[11], David Eden[12], Di Li[13,14], I. Ristorcelli[15], Sung-ju Kang[1], Yuxin Lin[16], D. Johnstone[6,7], J. H. He[17,18,19], P. M. Koch[8], Patricio Sanhueza[5], Sheng-Li Qin[20], Q. Zhang[21], N. Hirano[8], Paul F. Goldsmith[22], Neal J. Evans II[1,23], Glenn J. White[24,25], Minho Choi[1], Chang Won Lee[1,26], L. V. Toth[27,28], Steve Mairs[6], H.-W. Yi[29], Mengyao Tang[20], Archana Soam[1], N. Peretto[30], Manash R. Samal[31], Michel Fich[32], Harriet Parsons[2], Jinghua Yuan[13], Chuan-Peng Zhang[13], Johanna Malinen[33], George J. Bendo[11], A. Rivera-Ingraham[34], Hong-Li Liu[35,36,37], Jan Wouterloot[2], Pak Shing Li[38], Lei Qian[13], Jonathan Rawlings[39], Mark G. Rawlings[2], Siyi Feng[40], Yuri Aikawa[41], S. Akhter[42], Dana Alina[43], Graham Bell[2], J.-P. Bernard[15], Andrew Blain[44], Rebeka Bőgner[27], L. Bronfman[19], D.-Y. Byun[1], Scott Chapman[45], Huei-Ru Chen[46], M. Chen[6], Wen-Ping Chen[31], X. Chen[47], Xuepeng Chen[48], A. Chrysostomou[10], Giuliana Cosentino[39], M. R. Cunningham[42], K. Demyk[15], Emily Drabek-Maunder[49], Yasuo Doi[50], C. Eswaraiah[46], Edith Falgarone[51], O. Fehér[27,52], Helen Fraser[24], Per Friberg[2], G. Garay[19], J. X. Ge[17], W. K. Gear[30], Jane Greaves[30], X. Guan[53], Lisa Harvey-Smith[42,54], Tetsuo HASEGAWA[5], J. Hatchell[55], Yuxin He[56], C. Henkel[16,57], T. Hirota[5], W. Holland[58], A. Hughes[15], E. Jarken[56], Tae-Geun Ji[29], Izaskun Jimenez-Serra[59], Miju Kang[1], Koji S. Kawabata[60], Gwanjeong Kim[5], Jungha Kim[29], Jongsoo Kim[1], Shinyoung Kim[1], B.-C. Koo[61], Woojin Kwon[1,62], Yi-Jehng Kuan[63], K. M. Lacaille[45,64], Shih-Ping Lai[8,46], C. F. Lee[8], J.-E. Lee[29], Y.-U. Lee[1], Dalei Li[56], Hua-bai Li[65], N. Lo[19], John A. P. Lopez[42], Xing Lu[5], A-Ran Lyo[1], D. Mardones[19], A. Marston[66], P. McGehee[67], F. Meng[53], L. Montier[15], Julien Montillaud[68], T. Moore[12], O. Morata[8], Gerald H. Moriarty-Schieven[6], S. Ohashi[5], Soojong Pak[29], Geumsook Park[1], R. Paladini[67], Kate M Pattle[69], Gerardo Pech[8], V.-M. Pelkonen[3,68], K. Qiu[70], Zhi-Yuan Ren[13], John Richer[71], M. Saito[5], Takeshi Sakai[72], H. Shang[8], Hiroko Shinnaga[73], Dimitris Stamatellos[69], Y.-W. Tang[8], Alessio Traficante[74], Charlotte Vastel[15], S. Viti[39], Andrew Walsh[75], Bingru Wang[13], Hongchi Wang[48], Junzhi Wang[47], D. Ward-Thompson[69], Anthony Whitworth[30], Ye Xu[48], J. Yang[48], Yao-Lun Yang[76], Lixia Yuan[13], A. Zavagno[77], Guoyin Zhang[13], H.-W. Zhang[9], Chenlin Zhou[48], Jianjun Zhou[56], Lei Zhu[13], Pei Zuo[13], and Chao Zhang[20]

[1] Korea Astronomy and Space Science Institute, 776 Daedeokdaero, Yuseong-gu, Daejeon 34055, Republic of Korea; liutiepku@gmail.com
[2] East Asian Observatory, 660 N. A'ohoku Place, Hilo, HI 96720, USA
[3] Department of Physics, P.O. Box 64, FI-00014, University of Helsinki, Finland
[4] European Southern Observatory, Karl-Schwarzschild-Str. 2, D-85748 Garching bei München, Germany
[5] National Astronomical Observatory of Japan, National Institutes of Natural Sciences, 2-21-1 Osawa, Mitaka, Tokyo 181-8588, Japan
[6] NRC Herzberg Astronomy and Astrophysics, 5071 West Saanich Rd., Victoria, BC V9E 2E7, Canada
[7] Department of Physics and Astronomy, University of Victoria, Victoria, BC V8P 1A1, Canada
[8] Institute of Astronomy and Astrophysics, Academia Sinica. 11F of Astronomy-Mathematics Building, AS/NTU No. 1, Section 4, Roosevelt Rd., Taipei 10617, Taiwan
[9] Department of Astronomy, Peking University, 100871, Beijing, People's Republic of China
[10] Centre for Astrophysics Research, School of Physics Astronomy & Mathematics, University of Hertfordshire, College Lane, Hatfield, AL10 9AB, UK
[11] UK ALMA Regional Centre Node, Jodrell Bank Centre for Astrophysics, School of Physics and Astronomy, The University of Manchester, Oxford Road, Manchester M13 9PL, UK
[12] Astrophysics Research Institute, Liverpool John Moores University, IC2, Liverpool Science Park, 146 Brownlow Hill, Liverpool L3 5RF, UK
[13] National Astronomical Observatories, Chinese Academy of Sciences, Beijing, 100012, People's Republic of China
[14] Key Laboratory of Radio Astronomy, Chinese Academy of Science, Nanjing 210008, People's Republic of China
[15] IRAP, Université de Toulouse, CNRS, UPS, CNES, Toulouse, France
[16] Max-Planck-Institut für Radioastronomie, Auf dem Hügel 69, D-53121, Bonn, Germany
[17] Key Laboratory for the Structure and Evolution of Celestial Objects, Yunnan Observatories, Chinese Academy of Sciences, P.O. Box 110, Kunming, 650011, Yunnan Province, People's Republic of China
[18] Chinese Academy of Sciences, South America Center for Astrophysics (CASSACA), Camino El Observatorio 1515, Las Condes, Santiago, Chile
[19] Departamento de Astronomía, Universidad de Chile, Las Condes, Santiago, Chile
[20] Department of Astronomy, Yunnan University, and Key Laboratory of Astroparticle Physics of Yunnan Province, Kunming, 650091, People's Republic of China
[21] Harvard-Smithsonian Center for Astrophysics, 60 Garden Street, Cambridge, MA 02138, USA
[22] Jet Propulsion Laboratory, California Institute of Technology, 4800 Oak Grove Drive, Pasadena, CA 91109, USA
[23] Department of Astronomy, The University of Texas at Austin, 2515 Speedway, Stop C1400, Austin, TX 78712-1205, USA
[24] Department of Physics and Astronomy, The Open University, Walton Hall, Milton Keynes, MK7 6AA, UK
[25] RAL Space, STFC Rutherford Appleton Laboratory, Chilton, Didcot, Oxfordshire, OX11 0QX, UK
[26] University of Science & Technology, 176 Gajeong-dong, Yuseong-gu, Daejeon, Republic of Korea
[27] Eötvös Loránd University, Department of Astronomy, Pázmány Péter sétány 1/A, H-1117, Budapest, Hungary
[28] Konkoly Observatory of the Hungarian Academy of Sciences, H-1121 Budapest, Konkoly Thege Miklósút 15-17, Hungary
[29] School of Space Research, Kyung Hee University, Yongin-Si, Gyeonggi-Do 17104, Republic of Korea
[30] School of Physics and Astronomy, Cardiff University, Cardiff CF24 3AA, UK
[31] Institute of Astronomy, National Central University, Jhongli 32001, Taiwan
[32] Department of Physics and Astronomy, University of Waterloo, Waterloo, ON N2L 3G1, Canada
[33] Institute of Physics I, University of Cologne, Zülpicher Str. 77, D-50937, Cologne, Germany
[34] European Space Astronomy Centre (ESA/ESAC), Operations Department, Villanueva de la Cañada (Madrid), Spain
[35] Department of Physics, The Chinese University of Hong Kong, Shatin, NT, Hong Kong SAR
[36] Departamento de Astronomía, Universidad de Concepción, Av. Esteban Iturra s/n, Distrito Universitario, 160-C, Chile
[37] Chinese Academy of Sciences South America Center for Astronomy, People's Republic of China
[38] Astronomy Department, University of California, Berkeley, CA 94720, USA

[39] Department of Physics and Astronomy, University College London, Gower Street, London, WC1E 6BT, UK
[40] Max-Planck-Institut für Extraterrestrische Physik, Giessenbachstrasse 1, D-85748 Garching, Germany
[41] Center for Computational Sciences, The University of Tsukuba, 1-1-1, Tennodai, Tsukuba, Ibaraki 305-8577, Japan
[42] School of Physics, University of New South Wales, Sydney, NSW 2052, Australia
[43] Department of Physics, School of Science and Technology, Nazarbayev University, Astana 010000, Kazakhstan
[44] University of Leicester, Physics & Astronomy, 1 University Road, Leicester LE1 7RH, UK
[45] Department of Physics and Atmospheric Science, Dalhousie University, Halifax, NS, B3H 4R2, Canada
[46] Institute of Astronomy and Department of Physics, National Tsing Hua University, Hsinchu, Taiwan
[47] Key Laboratory for Research in Galaxies, and Cosmology, Shanghai Astronomical Observatory, Chinese Academy of Sciences, 80 Nandan Road, Shanghai 200030, People's Republic of China
[48] Purple Mountain Observatory, Chinese Academy of Sciences, Nanjing 210008, People's Republic of China
[49] Imperial College London, Blackett Laboratory, Prince Consort Rd., London SW7 2BB, UK
[50] Department of Earth Science and Astronomy, Graduate School of Arts and Sciences, The University of Tokyo, 3-8-1 Komaba, Meguro, Tokyo 153-8902, Japan
[51] LERMA, Observatoire de Paris, PSL Research University, CNRS, Sorbonne Universités, UPMC Univ. Paris 06, Ecole normale supérieure, F-75005 Paris, France
[52] Konkoly Observatory, Research Centre for Astronomy and Earth Sciences, Hungarian Academy of Sciences, H-1121 Budapest, Konkoly Thege Miklós út 15-17, Hungary
[53] Physikalisches Institut, Universität zu Köln, Zülpicher Str. 77, D-50937 Köln, Germany
[54] CSIRO Astronomy and Space Science, P.O. Box 76, Epping NSW, Australia
[55] Physics and Astronomy, University of Exeter, Stocker Road, Exeter EX4 4QL, UK
[56] Xinjiang Astronomical Observatory, Chinese Academy of Sciences; University of the Chinese Academy of Sciences, People's Republic of China
[57] Astronomy Department, Abdulaziz University, P.O. Box 80203, 21589, Jeddah, Saudi Arabia
[58] UK Astronomy Technology Center, Royal Observatory, Blackford Hill, Edinburgh EH9 3HJ, UK; Institute for Astronomy, University of Edinburgh, Royal Observatory, Blackford Hill, Edinburgh EH9 3HJ, UK
[59] School of Physics and Astronomy, Queen Mary University of London, Mile End Road, London E1 4NS, UK
[60] Hiroshima Astrophysical Science Center, Hiroshima University, Kagamiyama, Higashi-Hiroshima, Hiroshima 739-8526, Japan; Department of Physical Science, Hiroshima University, Kagamiyama, Higashi-Hiroshima 739-8526, Japan
[61] Department of Physics and Astronomy, Seoul National University, Gwanak-gu, Seoul 08826, Republic of Korea
[62] Korea University of Science and Technology, 217 Gajeong-ro, Yuseong-gu, Daejeon 34113, Republic of Korea
[63] Department of Earth Sciences, National Taiwan Normal University, 88 Section 4, Ting-Chou Road, Taipei 116, Taiwan
[64] Department of Physics and Astronomy, McMaster University, Hamilton, ON L8S 4M1 Canada
[65] Department of Physics, The Chinese University of Hong Kong, Shatin, New Territory, Hong Kong, People's Republic of China
[66] ESA/STScI, 3700 San Martin Drive, Baltimore, MD 21218 USA
[67] Infrared Processing Analysis Center, California Institute of Technology, 770 South Wilson Ave., Pasadena, CA 91125, USA
[68] Institut UTINAM—UMR 6213—CNRS—Univ Bourgogne Franche Comte, France
[69] Jeremiah Horrocks Institute for Mathematics, Physics & Astronomy, University of Central Lancashire, Preston PR1 2HE, UK
[70] School of Astronomy and Space Science, Nanjing University, Nanjing 210023, People's Republic of China
[71] Astrophysics Group, Cavendish Laboratory, J. J. Thomson Avenue, Cambridge CB3 0HE, UK
[72] Graduate School of Informatics and Engineering, The University of Electro-Communications, Chofu, Tokyo 182-8585, Japan
[73] Department of Physics and Astronomy, Graduate School of Science and Engineering, Kagoshima University, 1-21-35 Korimoto, Kagoshima 890-0065, Japan
[74] IAPS-INAF, via Fosso del Cavaliere 100, I-00133, Rome, Italy
[75] International Centre for Radio Astronomy Research, Curtin University, GPO Box U1987, Perth, WA 6845, Australia
[76] The University of Texas at Austin, Department of Astronomy, 2515 Speedway, Stop C1400, Austin, TX 78712-1205, USA
[77] Aix Marseille Universit, CNRS, LAM (Laboratoire dAstrophysique de Marseille) UMR 7326, F-13388, Marseille, France
Received 2017 September 4; revised 2017 December 16; accepted 2017 December 19; published 2018 February 1

Abstract

The low dust temperatures (<14 K) of *Planck* Galactic cold clumps (PGCCs) make them ideal targets to probe the initial conditions and very early phase of star formation. "TOP-SCOPE" is a joint survey program targeting ~2000 PGCCs in $J = 1$–0 transitions of CO isotopologues and ~1000 PGCCs in 850 μm continuum emission. The objective of the "TOP-SCOPE" survey and the joint surveys (SMT 10 m, KVN 21 m, and NRO 45 m) is to statistically study the initial conditions occurring during star formation and the evolution of molecular clouds, across a wide range of environments. The observations, data analysis, and example science cases for these surveys are introduced with an exemplar source, PGCC G26.53+0.17 (G26), which is a filamentary infrared dark cloud (IRDC). The total mass, length, and mean line mass (*M/L*) of the G26 filament are ~6200 $M_\odot$, ~12 pc, and ~500 $M_\odot$ pc^{-1}, respectively. Ten massive clumps, including eight starless ones, are found along the filament. The most massive clump as a whole may still be in global collapse, while its denser part seems to be undergoing expansion owing to outflow feedback. The fragmentation in the G26 filament from cloud scale to clump scale is in agreement with gravitational fragmentation of an isothermal, nonmagnetized, and turbulent supported cylinder. A bimodal behavior in dust emissivity spectral index (β) distribution is found in G26, suggesting grain growth along the filament. The G26 filament may be formed owing to large-scale compression flows evidenced by the temperature and velocity gradients across its natal cloud.

Key words: ISM: abundances – ISM: clouds – ISM: kinematics and dynamics – stars: formation – surveys

1. Introduction

In the current paradigm, stars form within cold and dense fragments in the clumpy and filamentary molecular clouds. Recent studies of nearby clouds by *Herschel* have revealed a "universal" filamentary structure in the cold interstellar medium (ISM; André et al. 2014). A main filament surrounded by a network of perpendicular striations seems to be a very common pattern in molecular clouds. Within the filaments are compact (sizes of 0.1 pc or less), cold ($T_k \leqslant 10$ K), and dense ($n(\mathrm{H_2}) > 5 \times 10^4$ cm^{-3}) starless condensations, usually dubbed "prestellar cores," which are centrally concentrated and largely thermally supported (Caselli 2011). However, the way that filaments form in the cold ISM is still far from being

well characterized. Also, the properties of prestellar cores and the way how prestellar cores evolve to form stars are still not fully understood, due to a lack of statistical studies toward a large sample.

The roles of turbulence, magnetic fields, gravity, and external compression in shaping molecular clouds and producing filaments can only be thoroughly understood by investigating an all-sky sample that contains a representative selection of molecular clouds in different environments. Observations by *Herschel* revealed that more than 70% of the prestellar cores (and protostars) are embedded in the larger, parsec-scale filamentary structures in molecular clouds (André et al. 2010, 2014; Könyves et al. 2010). The fact that the cores reside mostly within the densest filaments with column densities exceeding $\sim 7 \times 10^{21}$ cm^{-2} strongly suggests a column density threshold for core formation (André et al. 2014). Such a column density threshold for core formation was also suggested before *Herschel* (Johnstone et al. 2004; Kirk et al. 2006). The (prestellar) core mass function being very similar in shape to the stellar initial mass function further suggests a connection to the underlying star formation process (e.g., Motte et al. 1998; Johnstone et al. 2000; Alves et al. 2007; André et al. 2014; Könyves et al. 2015).

While significant progress has been made in recent years, past high-resolution continuum and molecular line surveys have mostly focused on the Gould Belt clouds or the inner Galactic plane. There are hence still fundamental aspects of the initial conditions for star formation that remain unaddressed, which include but are not limited to the following:

(1) On smaller scales (∼pc), how and where do prestellar cores (i.e., future star-forming sites) form in abundance? Specifically, can prestellar cores form in less dense and high-latitude clouds or short-lived cloudlets? Is there really a "universal" column density threshold for core/star formation?

(2) On larger scales ($\sim \times 10$ pc), what controls the formation of hierarchical structure in molecular clouds? What is the interplay between turbulence, magnetic fields, gravity, kinematics, and external pressure in molecular cloud formation and evolution in different environments (e.g., spiral arms, interarms, high latitude, expanding H II regions, supernova remnants)? How common are filaments in molecular clouds? What is the role of filaments in generating prestellar cores?

1.1. *Planck* Galactic Cold Clumps

Planck was the third-generation mission to measure the anisotropy of the cosmic microwave background radiation, and it observed the entire sky in nine frequency bands (between 30 and 857 GHz). The high-frequency channels of *Planck* cover the peak of the thermal emission spectrum of dust colder than 14 K (Planck Collaboration et al. 2011b, 2016), indicating that *Planck* could probe the coldest parts of the ISM. The *Planck* team has cataloged 13,188 *Planck* galactic cold clumps (PGCCs), which are distributed across the whole sky, i.e., from the Galactic plane to high latitudes, following the spatial distribution of the main molecular cloud complexes. All 13188 PGCCs are overlaid on the *Planck* map in Figure 1.

The catalog of PGCCs was generated using the CoCoCoDeT algorithm (Montier et al. 2010). The method uses spectral information to locate sources of cold dust emission. Each of the *Planck* 857, 545, and 353 GHz maps is compared to the *IRAS* 100 μm data. The 100 μm maps and the local average ratio of the *Planck* and *IRAS* bands represent the distribution of warm dust emission. The spectrum of this extended component is estimated from an annulus between 5′ and 15′ from the center position. This also sets an upper limit to the angular size of the detected clumps. Once the template of warm dust emission is subtracted from the *Planck* data, the residual maps of cold dust emission can be used for source detection. The initial catalogs were generated for the three *Planck* bands separately and were then merged, requiring a detection and a signal-to-noise ratio (S/N) greater than 4 in all three bands.

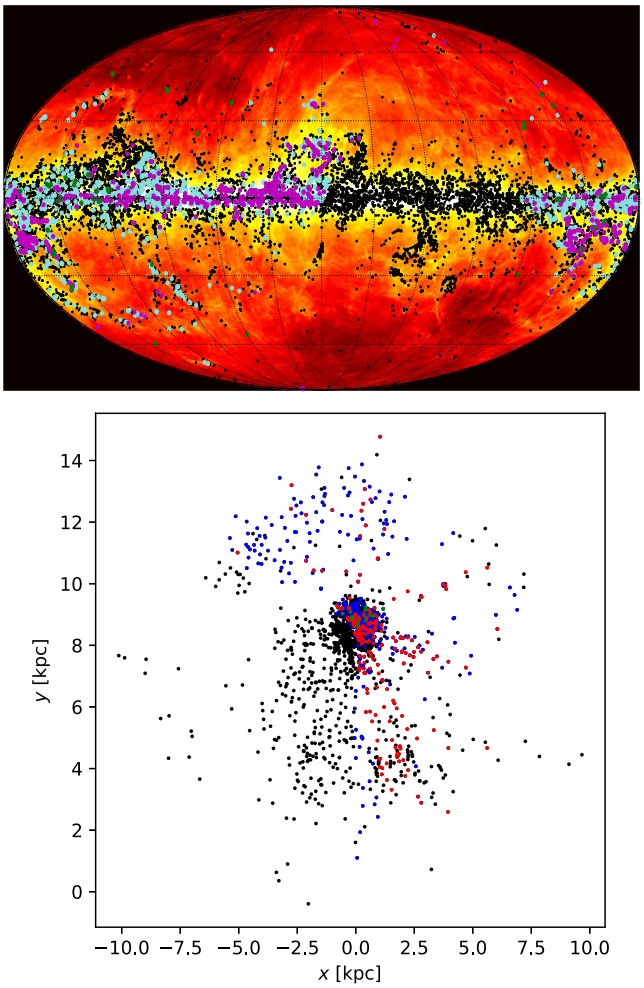

Figure 1. Top panel: all-sky distribution of the 13,188 PGCC sources (black dots), the 2000 PGCC sources (blue dots) selected for TOP, and the 1000 PGCC sources (magenta dots) selected for SCOPE overlaid on the 857 GHz *Planck* map. Bottom panel: face-on view of all-sky distribution of PGCCs with distances. The PGCCs in the initial PGCC sample, the TOP sample, and the SCOPE sample are shown with black dots, blue dots, and red dots, respectively. The green dots represent PGCCs observed in the SCUBA-2 Ambitious Sky Survey (SASSy) at the JCMT, as part of pilot studies of SCOPE.

The properties of the PGCC catalog are described in Planck Collaboration et al. (2016). The source spectral energy distributions (SEDs; based on the four bands used in the source detection) give color temperatures 6–20 K with a median value of ∼14 K. About 42% of the sources have reliable distance estimates that were derived with methods such as 3D extinction mapping, kinematic distances, and association with known cloud complexes. The distance distribution extends

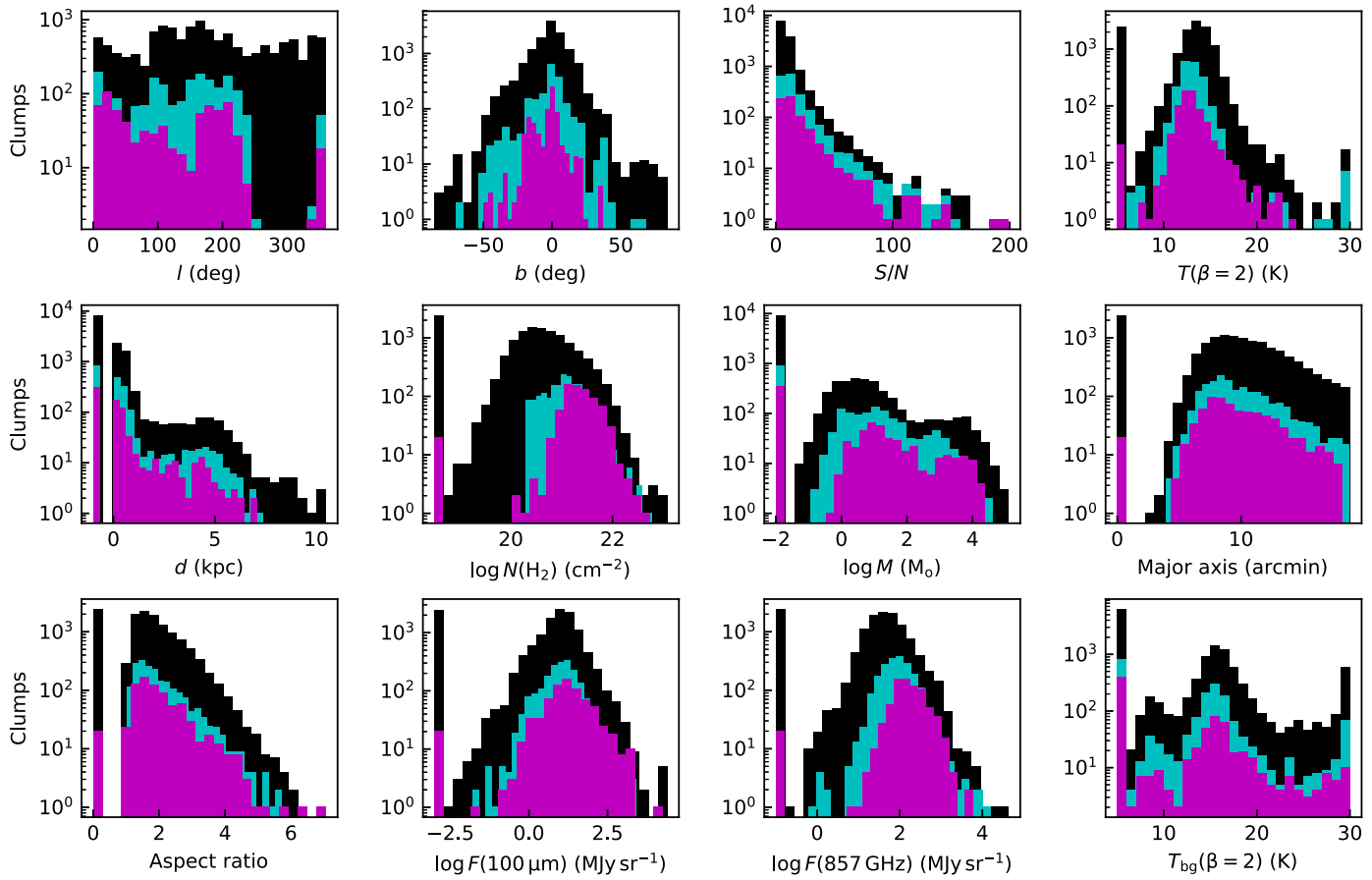

Figure 2. Statistics of the initial PGCC sample (black), the TOP sample (blue), and the SCOPE sample (magenta). The *y*-axis is number. From upper left to lower right: longitude, latitude, S/N, dust temperature, distance, column density, mass, major axis, aspect ratio, 100 μm flux density, 350 μm flux density, and background temperature. In the panels except for longitude, latitude, and S/N, the lowest bin corresponds to clumps for which the parameter value is unknown.

from 0.1 to 10 kpc with a median of ∼0.4 kpc. Because of the low angular resolution of the data (∼5′) and the wide distribution of distances, the PGCC catalog contains a heterogeneous set of objects from nearby low-mass clumps to distant massive clouds. This is reflected in the physical parameters where the object sizes range from 0.1 to over 10 pc and the masses from below 0.1 to over $10^4\,M_\odot$.

The PGCC catalog is the first homogeneous survey of cold and compact Galactic dust clouds that extends over the whole sky. The main common feature of the PGCC sources is the detection of a significant excess of cold dust emission. This is suggestive of high column densities, a fact that has also been corroborated by subsequent *Herschel* studies (Planck Collaboration et al. 2011b, 2016; Montillaud et al. 2015). The catalog covers a wide range of galactocentric distances (almost 0–15 kpc) and a wide range of environments from quiescent high-latitude clouds to active star-forming clouds and sites of potential triggered star formation. This makes the PGCC catalog a good starting point for many studies of the star formation process. Figure 2 shows the distributions of several parameters for the PGCC catalog sources.

A large fraction of PGCCs seem to be quiescent, not affected by ongoing star-forming activity (Wu et al. 2012; Liu et al. 2014). Those sources are prime candidates for probing how prestellar cores form and evolve, as well as the initial stages of star formation across a wide variety of Galactic environments. The detection of gravitationally bound CO gas clumps (Liu et al. 2012a; Meng et al. 2013; Zhang et al. 2016) and dense molecular line tracers (Yuan et al. 2016; Tatematsu et al. 2017) inside PGCCs strongly suggests that many PGCCs have the ability to form stars. Moreover, their low level of CO gas depletion indicates that the natal clouds of PGCCs are still in the early stages of molecular cloud evolution (Liu et al. 2013b). A number of PGCCs were purposely followed up with observations with the *Herschel* satellite. These higher-resolution data revealed great variety in the morphology of the PGCCs (Planck Collaboration et al. 2011a; Juvela et al. 2012; Montillaud et al. 2015). The clumps typically have significant substructure and are often (but not always) associated with cloud filaments (Rivera-Ingraham et al. 2016). Further clues to the nature of the clumps are provided by the dust emission properties, the PGCCs showing particularly high values for submillimeter opacity and the spectral index β (Juvela et al. 2015a, 2015b). Prestellar cores and extremely young Class 0 objects have been detected in PGCCs (Liu et al. 2016b; Tatematsu et al. 2017), indicating that some PGCCs can be used to trace the initial conditions when star formation commences.

Because of the uniqueness and importance of PGCC sources to understanding the earliest stages of star formation, we have been conducting a series of surveys to characterize the physical and dynamical state of PGCCs. These surveys are described in the following sections.

2. The "TOP-SCOPE" Survey of PGCCs

2.1. TRAO Observations of PGCCs (TOP)

"TOP" is a Key Science Program (KSP) of the Taeduk Radio Astronomy Observatory (TRAO). It is a survey of the $J = 1$–0 transitions of ^{12}CO and ^{13}CO toward ~2000 PGCCs. Some interesting PGCCs were also mapped in the C^{18}O (1–0) line. The "TOP" survey was initiated in 2015 December. The main aims of "TOP" are to find CO dense clumps; to study the universality and ubiquity of filamentary structures in the cold ISM; to study cloud evolution in conjunction with H I surveys; to investigate how CO abundances change with the evolutionary status of the cloud, and across a range of different environments; to investigate the roles of turbulence, magnetic fields, and gravity in structure formation; and to investigate the dynamical effect of stellar feedback and/or cloud–cloud collisions on star formation.

(1) *The TRAO 14 m telescope*

The Taeduk Radio Astronomy Observatory (TRAO[78]) was established in 1986 October with the 14 m radio telescope located on the campus of the Korea Astronomy and Space Science Institute (KASI) in Daejeon, South Korea. The surface accuracy of the primary reflector is <130 μm rms, and the telescope pointing accuracy is better than 10″ rms. The main FWHM beam sizes for the ^{12}CO (1–0) and ^{13}CO (1–0) lines are 45″ and 47″, respectively. The new receiver system, SEQUOIA-TRAO, is equipped with high-performance 16-pixel MMIC preamplifiers in a 4 × 4 array, operating in the 85–115 GHz frequency range. The noise temperature of the receiver is 50–80 K over most of the band. The system temperature ranges from 150 K (86–110 GHz) to 450 K (115 GHz; ^{12}CO). The second IF modules with a narrow band and the eight channels with four fast Fourier transform (FFT) spectrometers allow simultaneous observations at two frequencies within the 85–100 GHz or 100–115 GHz bands for all 16 pixels of the receiver. The backend system (an FFT spectrometer) provides 4096 × 2 channels with fine velocity resolution of 0.04 km s^{-1} (15 kHz) per channel and full spectral bandwidth of 60 MHz (~160 km s^{-1} for ^{12}CO).

(2) *Source selection*

The TOP survey has a target list that probes the early stages of star formation across a wide range of Galactic environments. The starting point is the PGCC catalog, which contains all cold dust clouds detected by *Planck*, in combination with the *IRAS* 100 μm data. Given the very high sensitivity of the *Planck* measurements, the PGCC catalog is currently the most complete unbiased all-sky catalog of cold clumps.

The TOP target list was constructed according to the following selection criteria. We excluded regions targeted as part of the previous Galactic plane (Moore et al. 2015) or Gould Belt surveys (Ward-Thompson et al. 2007) at the James Clerk Maxwell Telescope (JCMT[79]) because these locations have been extensively observed by other telescopes (e.g., JCMT, NRO 45 m, and PMO 14 m) both by molecular line and by dust continuum emission observations. The TOP survey is therefore highly complementary to these previous surveys. The PGCCs in these excluded regions will also be investigated in our statistical studies using the archived data.

To ensure a representative study of the full PGCC population, the sources were divided into bins of Galactic longitude (every 30°), latitude (divided by $|b| = 0°$, 4°, 10°, and 90°), and distance (divided by $d = 0$, 200, 500, 1000, 2000, and 8000 pc and unknown), and targets were selected from each bin. Similarly, we cover the full range of source temperatures and column densities in *Planck* measurements. The sampling is weighted toward the very coldest sources. The sample includes 787 very cold sources for which the PGCC catalog only gives a temperature upper limit. To ensure a good detection rate, the sampling is weighted toward higher column densities. Within the constraints listed above, preference is given to regions covered previously by *Herschel* observations, which can further confirm the presence of compact sources and give more reliable estimates of their column densities. Figure 1 shows our target list of 2000 sources, sufficient to sample well the whole TRAO-visible sky and enable meaningful statistical studies of targets with different physical characteristics and in different environments.

About one-third of the 2000 sources have *Herschel* data at 70/100–500 μm. A large fraction of these data come from the *Herschel* Galactic Cold Cores survey (PI: M. Juvela), where the targets were also selected from the PGCC catalog, employing a random sampling similar to the one outlined above. The TOP sample covers widely different Galactic environments as shown in Figure 1. Among the 2000 sources, 219 are located in the Galactic plane with $|b| < 1°$ and 154 at high latitudes with $|b| > 30°$. Based on positional correlations, a sizable fraction of the targets in the Galactic plane are expected to be influenced by nearby H II regions (Planck Collaboration et al. 2016). For example, 50 PGCCs in the λ Orionis complex were included in the TOP sample. The λ Orionis Complex containing the nearest giant H II region has a moderately enhanced radiation field, and the molecular clouds therein seem to be greatly affected by stellar feedback (Goldsmith et al. 2016; Liu et al. 2016b). Among the 1181 sources with known distances in the TOP sample, 997 are within 2 kpc and 99 are beyond 4 kpc. Out of the 2000 sources, 753 have axial ratios larger than 2, suggestive of extended filamentary structures.

In Figure 2, we show the distributions of parameters for the TOP sample and the initial PGCC sample. In general, the TOP sample has similar distributions in longitude, latitude, and sizes to the initial PGCC sample. However, the TOP sample tends to have lower temperature and higher column density than the initial PGCC sample.

(3) *Observation strategy*

We first conduct single-pointing observations in the ^{12}CO (1–0) and ^{13}CO (1–0) lines simultaneously, to determine the systemic velocity of each target and also to find suitable reference positions for mapping. The on- and off-source integration time in the single-pointing survey is 30 s. For mapping observations, we applied the on-the-fly (OTF) mode to map the PGCCs in the ^{12}CO (1–0) and ^{13}CO (1–0) lines simultaneously. A small fraction (<10%) of interesting "TOP" targets will also be mapped in the C^{18}O (1–0) line. The map size is set to 15′ × 15′. Since the PGCC sources have average angular sizes of 8′ (Planck Collaboration et al. 2016), the map size is large enough to well cover most PGCCs. We did, however, obtain larger (e.g., 30′) OTF maps for some extended PGCCs. The FWHM beam sizes (θ_B) for the ^{12}CO (1–0) and ^{13}CO (1–0) lines are 45″ and 47″, respectively. The main-beam efficiencies (η_B) for the ^{12}CO (1–0) and ^{13}CO (1–0) lines are

[78] http://radio.kasi.re.kr/trao/main_trao.php
[79] http://www.eaobservatory.org/jcmt/about-jcmt/

54% and 51%, respectively. The typical system temperatures for the ^{12}CO (1–0) and ^{13}CO (1–0) lines were ∼500 K and ∼250 K, respectively. We can achieve a typical sensitivity of ∼0.5 and 0.2 K in T_A^* for the ^{12}CO (1–0) and ^{13}CO (1–0) lines, respectively, at a spectral resolution of 0.33 km s^{-1} over the mapping field in ∼40 minutes of integration time. The OTF data are regridded into Class format files with a pixel size of 24″ with an OTFtool at TRAO. The OTF data were smoothed to 0.33 km s^{-1} and baseline removed with Gildas/Class with a first- or third-order polynomial. Then the Class format files were converted to FITS format files for analysis with the MIRIAD and CASA packages.

2.2. SCUBA-2 Continuum Observations of Pre-protostellar Evolution (SCOPE)

The "SCOPE"[80] is one of the eight large programs at the JCMT of the East Asian Observatory (EAO) in the 2015 call. It is a survey of ∼1000 PGCCs at 850 μm continuum. The "SCOPE" project was launched in 2015 December. The main aims of the "SCOPE" survey are to obtain a census of dense clumps distributed in widely different environments, to study the roles of filaments in dense core formation, to investigate dust properties, and to detect rare populations of dense clumps (e.g., first hydrostatic cores; massive starless cores; pre-/proto-brown dwarfs; extremely cold cores).

(1) *The SCUBA-2 bolometer camera at the JCMT 15 m telescope*

With a diameter of 15 m, the JCMT is the largest single-dish astronomical telescope in the world designed specifically to operate in the submillimeter wavelength region of the spectrum. SCUBA-2 (Submillimetre Common-User Bolometer Array 2[81]) is an array operating simultaneously at 450 and 850 μm with a total of 5120 bolometers per wavelength (Holland et al. 2013). The instrument has a field of view of 45 arcmin^2. The instrument is cooled by three pulse tube coolers and a dilution refrigerator. The dilution fridge has a base temperature of about 50 mK. The focal plane that is the heat bath for the bolometers is temperature controlled at 75 mK. The main FWHM beam size of SCUBA-2 is 7.″9 at 450 μm and 14.″1 at 850 μm (Dempsey et al. 2013).

(2) *Source selection*

The 1000 "SCOPE" targets are selected from the 2000 PGCCs in the "TOP" survey sample. Preference is given to regions covered by *Herschel* observations or high column density (>1 × 10^{21} cm^{-2} in *Planck* measurements) clumps. From our pilot study of 300 PGCCs (see Figure 3), we found that the dense core detection rates in SCUBA-2 observations drastically drop toward PGCCs with higher latitude and lower column density. Therefore, the "SCOPE" sample is further selected biased to high column density PGCCs in each parameter bin of the "TOP" survey sample. However, to ensure a good representation of the Galactic distribution of the full PGCC population, we also included many lower column density (>5 × 10^{20} cm^{-2} in *Planck* measurements) clumps at high latitudes as well. As shown in Figure 2, the SCOPE sample has similar distributions in most parameters (except column density, mass, and flux) to the TOP sample and the initial PGCC sample. The SCOPE sample tends to have larger

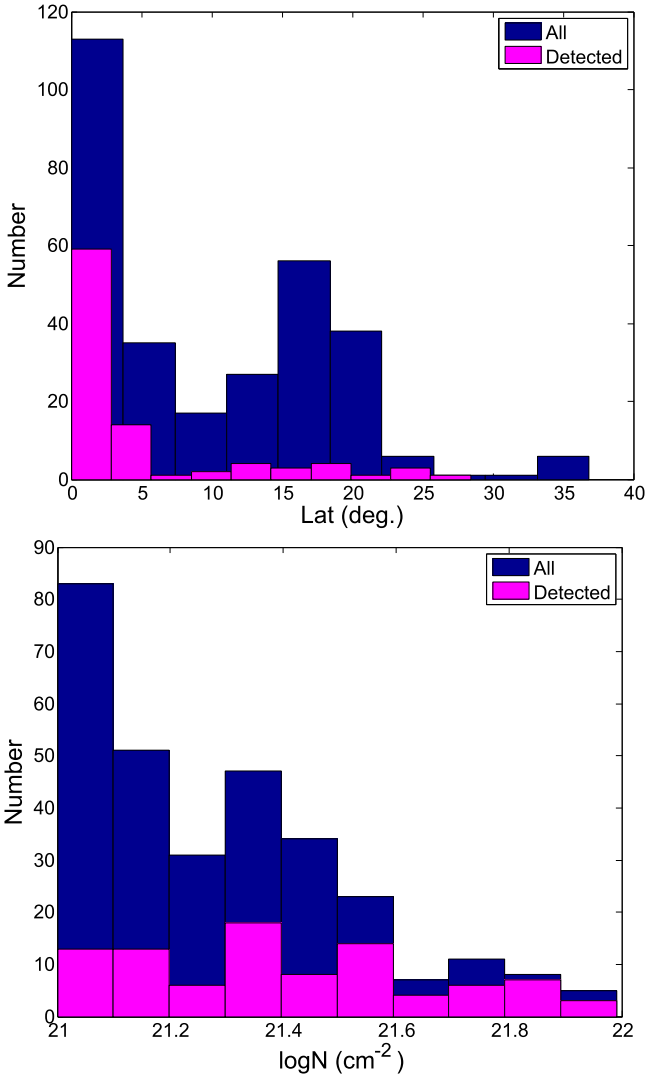

Figure 3. SCUBA-2 detections as a function of latitude (top panel) and column density (bottom panel) for PGCCs in the pilot study. The 300 PGCCs in pilot studies are shown in blue, while those with SCUBA-2 detections are shown in pink.

column density and masses than the TOP sample and the initial PGCC sample. About half of the SCOPE sources have distances within 2 kpc. The high resolution of SCUBA-2 at 850 μm can easily resolve dense cores (with sizes of ∼0.1 pc) inside these PGCCs with distances smaller than ∼2 kpc.

(3) *Observation strategy*

Since the PGCC sources have average angular sizes of 8′ (Planck Collaboration et al. 2016), as noted above, the "SCOPE" observations were conducted primarily using the CV Daisy mode.[82] The CV Daisy is designed for small compact sources providing a deep 3′ (in diameter; the same as below) region in the center of the map but coverage out to beyond 12′ (Bintley et al. 2014). All the SCUBA-2 850 μm continuum data were reduced using an iterative mapmaking technique (Chapin et al. 2013). Specifically, the data were all run with the same reduction tailored for compact sources, filtering out scales larger than 200″ on a 4″ pixel scale, for the

[80] SCOPE: https://www.eaobservatory.org/jcmt/science/large-programs/scope/.
[81] http://www.eaobservatory.org/jcmt/instrumentation/continuum/scuba-2/
[82] http://www.eaobservatory.org/jcmt/instrumentation/continuum/scuba-2/observing-modes/

first data release to the team. We also, however, tried different filtering and external masks in the data reduction for individual sources, which will be discussed below. The flux conversion factor (FCF) varies with time. A mean FCF of 554 Jy pW^{-1} $beam^{-1}$ was used to convert data from pW to Jy $beam^{-1}$ in the pipeline for the first data release. The FCF is higher than the canonical value derived by Dempsey et al. (2013). This higher value reflects the impact of the data reduction technique and pixel size used by us. The observations were conducted under grade 3/4 weather conditions with 225 GHz opacities between 0.1 and 0.15. With 16 minutes of integration time per map, we reach an rms noise of ~6–10 mJy $beam^{-1}$ in the central 3′ region. The rms noise increases to 10–30 mJy $beam^{-1}$ out to 12′, which is better than the sensitivity (50–70 mJy $beam^{-1}$) in the 870 μm continuum ATLASGAL survey (Contreras et al. 2013).

3. Other Joint Surveys and Follow-up Observations

Besides the "TOP-SCOPE" survey, we are also conducting joint surveys and follow-up observations with other telescopes (e.g., SMT 10 m, KVN 21 m, NRO 45 m, and SMA; see Liu et al. 2016b; Tatematsu et al. 2017).

3.1. SMT "All-sky" Mapping of PLanck Interstellar Nebulae in the Galaxy (SAMPLING)

"SAMPLING[83]" is an ESO public survey to map up to 600 PGCCs in the $J = 2$–1 transition of ^{12}CO and ^{13}CO using the SMT 10 m telescope (Wang et al. 2018). The "SAMPLING" project was also launched in 2015 December. The typical map size in the "SAMPLING" survey is 5′ × 5′ with an rms level of ~0.2 K at a spectral resolution of 0.34 km s^{-1}. The beam size and main-beam efficiency are 36″ and 0.7, respectively. In conjunction with the "TOP-SCOPE" survey, the "SAMPLING" survey aims to resolve the clump structure, to derive the internal variations of column density and turbulent and chemical properties, and also to make a connection to Galactic structure. We observed the exemplar source, PGCC G26.53 +0.17, in the ^{13}CO (2–1) line with the SMT telescope. The observational parameters are summarized in Table 4 in Appendix A.

3.2. KVN Survey of SCUBA-2 Dense Clumps

The Korean VLBI Network (KVN) is a three-element Very Long Baseline Interferometry (VLBI) network working at millimeter wavelengths. Three 21 m radio telescopes are located in Seoul, Ulsan, and Jeju Island, Korea. We use the single-dish mode of the three 21 m radio telescopes to observe the dense clumps detected in the "SCOPE" survey. The antenna pointing accuracy of the KVN telescopes is better than 5″. The KVN telescopes can operate at four frequency bands (i.e., 22, 44, 86, and 129 GHz) simultaneously. The beam sizes at the four bands are ~126″, ~63″, ~32″, and ~23″ at 22, 44, 86, and 129 GHz, respectively. The main-beam efficiencies are ~50% at 22 and 44 GHz and ~40% at 86 and 129 GHz.

A key science proposal for single-pointing molecular line observations of ~1000 "SCOPE" dense clumps with KVN telescopes will be submitted in 2018. The main target lines are the 22 GHz water maser, 44 GHz Class I methanol maser, and other dense molecular lines, which are listed in Table 4 in Appendix A. The 22 GHz water maser and 44 GHz Class I methanol maser are indicators of outflow shocks. SiO thermal lines are also good tracers for outflow shocks or shocks induced by cloud–cloud collisions. Dense gas tracers (e.g., $J = 1$–0 transitions of N_2H^+, $H^{13}CO^+$, $HN^{13}C$) can be used to determine the systemic velocities and the amount of turbulence in dense clumps. Optically thick lines (e.g., $J = 1$–0 transitions of HCN and HCO^+) can be used to trace infall and outflow motions. $H_2CO 2_{1,2} - 1_{1,1}$ is a dense gas tracer and can also be used to reveal infall and outflow motions (Liu et al. 2016b). The deuteration of H_2CO will be determined from observations of H_2CO ($2_{1,2} - 1_{1,1}$) and HDCO ($2_{0,2} - 1_{0,1}$) lines. The [HDCO]/[H_2CO] ratios will be used to trace the early phase of dense core evolution (Kang et al. 2015). Pilot surveys of ~200 "SCOPE" dense clumps with the KVN telescopes were conducted in 2016 (e.g., Liu et al. 2016b; S.-J. Kang et al., 2018, in preparation; H.-W. Yi et al. 2018, in preparation). In the single-pointing molecular line observations, it takes about 20 minutes (on+off) to achieve an rms level of <0.1 K in brightness temperature with dual polarization at a spectral resolution of ~0.2 km s^{-1} under normal weather conditions. The KVN observations of the exemplar source, PGCC G26.53 +0.17, are summarized in Table 4 in Appendix A.

The KVN data are also reduced with the Gildas/Class package. All the scans were averaged to get the final averaged spectra, and the baselines of the averaged spectra were removed with a linear fit.

3.3. NRO 45 m Follow-up Survey

By using the 45 m telescope of Nobeyama Radio Observatory (NRO), we plan to carry out a comprehensive study of cores selected from the JCMT SCOPE survey to scrutinize the initial conditions of star formation in widely different environments, including massive star-forming regions. We will observe 100 cores in various environments in DNC, $HN^{13}C$, N_2D^+, and cyclic-C_3H_2 with receiver T70 in single-pointing mode. Among the 100 cores, 35 cores will also be mapped in ^{12}CO, ^{13}CO ,$C^{18}O$, N_2H^+, HC_3N, and CCS with the FOREST receiver. The FWHM beam size of the NRO 45 m telescope at 86 GHz is ~18.″8, and the main-beam efficiency is ~54%. Adding 115 Orion cores already observed in single-pointing mode, we will have data for 215 single-pointing positions. By using DNC and N_2D^+ intensities and the chemical evolution factor (CEF) for DNC/$HN^{13}C$, we will select the best targets of 35 cores for OTF mapping with the four-beam 2SB 2-polarization receiver FOREST. By applying CEF we developed (Tatematsu et al. 2017), we should be able to identify cores on the verge of massive star formation. From deuterium fractionation, we can identify the earliest protostellar phase. We will confirm/revise CEF by observing Orion cores having similar distances. The chemical nature of cores including deuterium fractionation will be investigated. Core stability will be investigated to see how star formation starts. Dynamics of parent filaments will be investigated to see whether there is accretion onto cores. Coefficients of the line width–size relation will be compared among different environments to see its meaning in star formation. Specific angular momentum will be compared among regions.

The large proposal requesting 350 hr over 2 yr since 2017 December was accepted for such follow-up observations. The NRO 45 m observations of the exemplar source, PGCC G26.53

[83] http://sky-sampling.github.io

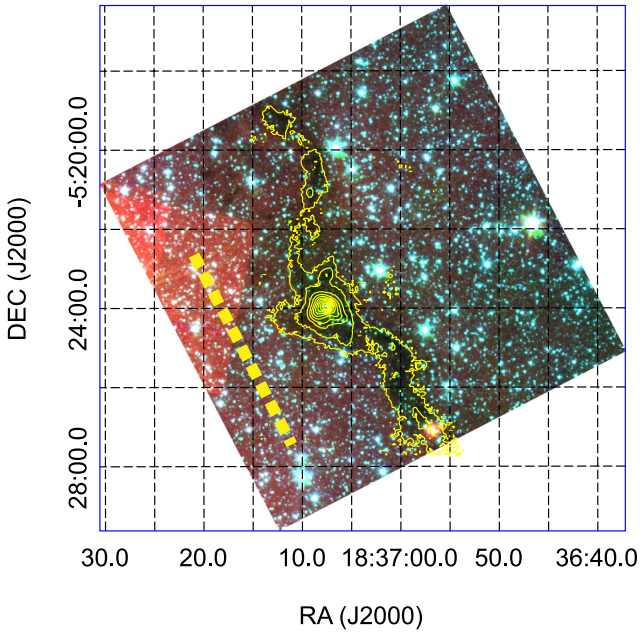

Figure 4. *Spitzer*/IRAC three-color (3.6 μm in blue, 4.5 μm in green, and 8 μm in red) composite image of PGCC G26.53+0.71. The yellow contours represent the SCUBA-2 850 μm continuum emission, filtering out scales of >200″. The contour levels are [0.03, 0.05, 0.1, 0.2, 0.4, 0.6, 0.8] × 1.38 Jy beam^{-1}. The yellow dashed line shows the direction of the Galactic plane.

+0.17, have not yet been conducted. Therefore, no results from NRO 45 m observations of PGCC G26.53+0.17 will be presented in this paper. Some pilot studies with the NRO 45 m telescope toward SCUBA-2 dense cores in PGCCs were presented in Tatematsu et al. (2017).

4. Example Science with an Exemplar Source, PGCC G26.53+0.17

Through the TOP-SCOPE survey and follow-up observations with other telescopes (e.g., SMT, KVN, and NRO 45 m), we aim to statistically investigate the physical and chemical properties of thousands of dense clumps in widely different environments. Those studies will help answer the questions raised at the beginning of this paper. The full scientific exploitation of the TOP-SCOPE survey data will only be possible upon the completion of the survey. In this paper, we introduce the survey data, data analysis, and example science cases of the above surveys with an exemplar source, PGCC G26.53+0.17 (hereafter denoted as G26). Located at a distance of 4.2 ± 0.3 kpc, G26 has a mass of ∼5200 $M_\odot$ and a very low luminosity-to-mass ratio of ∼1.4 $L_\odot/M_\odot$ (Planck Collaboration et al. 2016). The distance is estimated using the near-infrared extinction (Planck Collaboration et al. 2016). The kinematic distance is 3.2–3.4 kpc (Planck Collaboration et al. 2016; N. Peretto et al. 2018, in preparation). In this paper, we adopt the distance of 4.2 kpc to be consistent with Planck Collaboration et al. (2016). The spatial resolution of SCUBA-2 at 850 μm is ∼0.3 pc at this distance, which is high enough to resolve massive clumps with sizes of ∼1 pc. As shown in Figure 4, G26 is a filamentary IRDC (Peretto & Fuller 2009) with a length of ∼10′, corresponding to ∼12 pc at a distance of 4.2 kpc. G26 was observed as part of the "TOP," "SCOPE," "SAMPLING," and KVN surveys. The observations of G26 are summarized in Table 4 in Appendix A. The data reduction of JCMT/SCUBA-2 data will be presented in Section A.2. The methods used for G26 JCMT/SCUBA-2 data analysis in this work will also be applied to other targets in the "TOP-SCOPE" survey.

4.1. SEDs Using Filtered Herschel and SCUBA-2 Maps

The high-resolution SCUBA-2 850 μm data filtered out large-scale extended emission and thus are sensitive to the denser structures (filaments, cores, or clumps) in molecular clouds. The 850 μm data are also important in providing high-resolution information about the dust emission at a wavelength that lies in the regime between the far-infrared part (e.g., *Herschel*) and the millimeter part of the dust emission spectrum. One of the main goals of the "SCOPE" survey is to provide high-quality 850 μm data to constrain better the dust emission spectrum of dense structures in molecular clouds.

In this section, we fit the SEDs pixel by pixel with a modified blackbody function using four or five bands, combining SCUBA-2 measurements and fluxes extracted from *Herschel* maps that have been run through the SCUBA-2 pipeline. The algorithm of the SED fit is the same as in Section 6.1 in Appendix A. The *Herschel* and SCUBA-2 data with the subtraction of the local background were fitted with modified blackbody spectra with $\beta = 1.8$ to estimate color correction factors and to derive estimates of the dust optical depth at a common spatial resolution of 40″. In Section 4.3, we fit the SEDs with free β to investigate the dust grain properties. The details of the SED fits using filtered *Herschel* and SCUBA-2 maps will be discussed in Juvela et al. (2017). In this paper, we performed four individual SCUBA-2 data reductions labeled *R1, R2, R3,* and *R4* with different external masks and spatial filters (see Section 6.2 in Appendix A for details). *R1* with a spatial filter of 200″ is very efficient at identifying dense clumps/cores and is used for creating dense core/clump catalogs in our first data release to the team. However, here we fit the SEDs with data sets obtained from two other data reduction methods (*R2, R4*), which use larger spatial filters (300″ and 600″) and thus can recover more flux. We applied two sets of SED fits (*S1* and *S2*) using different data sets.

(1) *S1:Herschel* 160–500 μm data and SCUBA-2 850 μm data in the *R2* data reduction (see Section 6.2 in Appendix A) were used. The extended emission larger than 300″ in the *Herschel* and SCUBA-2 maps was filtered out.

(2) *S2:Herschel* 160–500 μm data and SCUBA-2 850 μm data in the *R4* data reduction (see Section 6.2 in Appendix A) were used. The extended emission larger than 600″ in the *Herschel* and SCUBA-2 maps was filtered out.

Figures 5(a) and (b) show the dust temperature (T_d) and 250 μm optical depth (τ_{250}) maps from the two SED fits. The T_d values across the filament ridge are around 10–14 K, except for the dense clumps located in the central region (∼17 K) and the southern end (∼19 K), where protostars have formed and heated their local surroundings. The less dense region to the east of the filament ridge has higher T_d than the dense filament, indicating that the filament is externally heated from its eastern side.

The T_d and τ_{250} maps are quite different from SED fits with different effective spatial filters. In Figures 5(c)–(d), we compare the T_d and τ_{250} values from SED fits *S1* and *S2* for pixels with S/N > 5 in the SCUBA-2 map from the *R2* imaging scheme. The mean dust temperature from *S1* and *S2* is 13.7 and 14.3 K, respectively. In comparison, the mean τ_{250} (or column density N) in *S1* and *S2* is 6.5×10^{-3} (or $N \sim 1.0 \times 10^{22}$ cm^{-2}) and 8.3×10^{-3} (or $N \sim 1.3 \times 10^{22}$ cm^{-2}), respectively. In contrast to *S1*, *S2* increases the T_d in cold

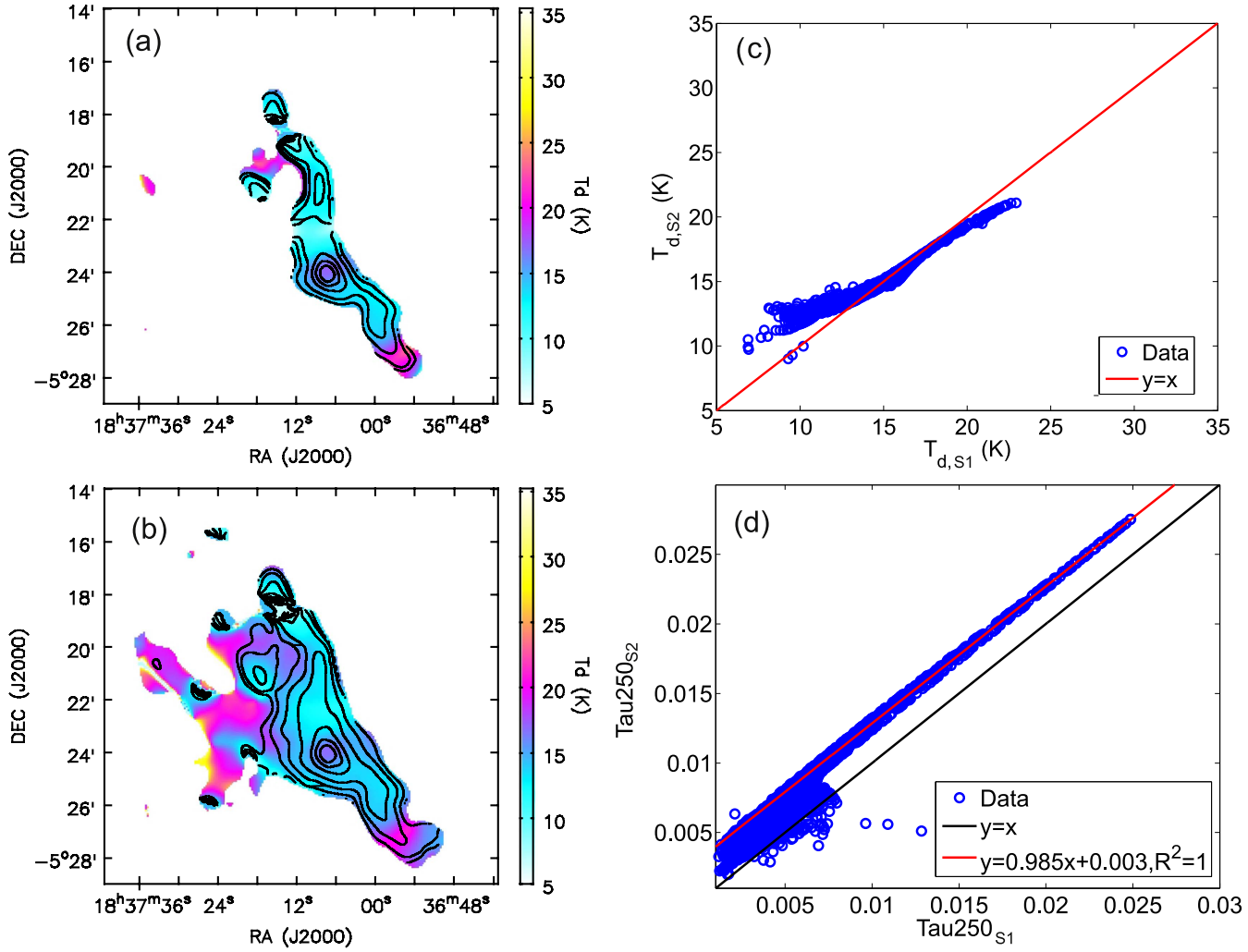

Figure 5. (a) Dust temperature map in the *S1* SED fit shown in color scale. The 250 μm optical depth is shown with contours. The contour levels are [0.03, 0.05, 0.1, 0.2, 0.4, 0.6, 0.8] × 0.0270. (b) Dust temperature map in the *S2* SED fit shown in color scale. The 250 μm optical depth is shown with contours. The contour levels are [0.03, 0.05, 0.1, 0.2, 0.4, 0.6, 0.8] × 0.0275. (c) Comparison of the dust temperature values in *S1* and *S2*. Only data points with S/N > 5 in the SCUBA-2 map are considered. (d) Comparison of the 250 μm optical depth in *S1* and *S2*. Only data points with S/N > 5 in the SCUBA-2 map are considered. The red line shows the linear fit toward the data points with 250 μm optical depth larger than 0.01 in *S4*.

regions (with $T_d < 15$ K), whereas in warmer regions (with $T_d > 15$ K), the T_d determined in *S1* and *S2* does not vary too much. *S2* significantly increases τ_{250} by 0.003 more (or $N \sim 4.6 \times 10^{21}$ cm^{-2}) than *S1* in dense regions (with $\tau_{250} \sim 0.01$ or $N \sim 1.5 \times 10^{22}$ cm^{-2} in the *S2*map). The peak column densities in *S1* and *S2* are 3.8×10^{22} cm^{-2} and 4.2×10^{22} cm^{-2}, respectively. In less dense regions, *S2* also significantly increases τ_{250}, but not as much as in dense regions.

SED fits with large effective spatial filters (600″; Figure 5(b)) recovered more extended structure and thus more mass. The total mass of the G26 filament revealed in *S2* is ~6200 $M_\odot$. Given the length ($L \sim 12$ pc) of the filament, the mean line mass (*M/L*) of the filament is ~500 $M_\odot$ pc^{-1}. For comparison, both the length and line mass of G26 are comparable to those ($L \sim 8$ pc; $M/L \sim 400$ $M_\odot$ pc^{-1}) of the integral shaped filament in the Orion A cloud (Bally et al. 1987; Kainulainen et al. 2017).

4.2. Dense Clumps

The "SCOPE" survey aims to obtain a census of "all-sky" distributed dense clumps and cores. Since PGCC sources trace some of the coldest ISM in the Galaxy, an extensive survey of PGCC sources is able to provide us with a number of candidates of clumps and cores at their earliest evolutionary phases. In nearby clouds, we expect to discover a population of prestellar core candidates or extremely young (e.g., Class 0) protostellar objects (Liu et al. 2016b; Tatematsu et al. 2017). In Galactic plane PGCCs, we are particularly interested in searching for massive clumps or cores that may represent the initial conditions of high-mass star formation. Below, we demonstrate the source extraction process based on the G26 SCUBA-2 images. The properties of clumps identified in G26 will also be investigated.

Extraction of the dense clumps was done using the FELLWALKER (Berry 2015) source extraction algorithm, part of the Starlink CUPID package (Berry et al. 2007). The core of the FellWalker algorithm is a gradient-tracing scheme consisting of following many different paths of steepest ascent in order to reach a significant summit, each of which is associated with a clump (Berry et al. 2007). FellWalker is less dependent on specific parameter settings than CLUMPFIND (Berry et al. 2007). The source extraction process with FellWalker in the SCOPE survey is the same as that used by the JCMT Plane Survey, and details can

be found in Moore et al. (2015) and Eden et al. (2017). A mask constructed above a threshold of 3σ (i.e., three times the pixel-to-pixel noise) in the S/N map is applied to the intensity map as input for the task CUPID:EXTRACTCLUMPS, which extracts the peak and integrated flux density values of the clumps. A further threshold for CUPID:FINDCLUMPS was the minimum number of contiguous pixels, which was set at 12, corresponding to the number of pixels expected to be found in an unresolved source with a peak S/N of 5σ, given a 14″ beam and 4″ pixels. The cores close to the map edges that are associated with artificial structures were further removed manually.

In total, 10 clumps were identified from the SCUBA-2 images. Those 10 clumps can be identified in at least two of the SCUBA-2 data reductions (*R1*, *R2*, *R3*, and *R4*; see Section 6.2 in Appendix A). Figure 6(a) presents the distributions of these 10 clumps on the 850 μm image from the *R2* reduction. From checking *Spitzer* (see Figure 4) and the *Herschel*/PACS 70 μm data, we found that clumps "6" and "10" are associated with young stellar objects, while the others are likely starless. The parameters of these clumps are summarized in Table 1. The effective radius is defined as $R_{\rm eff} = \sqrt{ab}$, where a and b are the deconvolved FWHM sizes of the clump major and minor axes. The clump masses (M) are derived with Equation (4) in Appendix A with total fluxes of 850 μm continuum emission from the SCUBA-2 images. The radii and masses are listed in the seventh and 12th columns of Table 1, respectively. The particle number density (n) and column density (N) were calculated as $n = M/\frac{4}{3}\pi R_{\rm eff}^3\ \mu {\rm m_H}$ and $N = M/\pi\ R_{\rm eff}^2\ \mu {\rm m_H}$, respectively, where $\mu = 2.37$ is the mean molecular weight per "free particle" (H_2 and He) and $m_{\rm H}$ is the atomic hydrogen mass.

Figure 6(b) compares the peak fluxes of the dense clumps in different imaging schemes. In general, applying larger spatial filters increase the peak fluxes particularly for less dense clumps. The peak flux of the most massive clump "6" does not change too much (<10%) in different imaging schemes. In contrast to *R1*, however, the peak fluxes of other less dense clumps increased by ~20%–50% in *R2* and by 50%–100% in *R3* and *R4*. Imaging scheme *R1* is used in the first data release of the SCOPE survey. *R1* is very efficient to detect dense clumps but cannot well recover flux from extended structures. Therefore, we suggest to use external masks and larger spatial filtering in SCUBA-2 data reduction to recover more flux if *Herschel* data are available.

Figure 6(c) presents the mass–radius relation for the dense clumps. In general, larger scales kept by spatial filtering lead to larger masses and radii. The red dashed line shows a density threshold for high-mass star formation (Kauffmann & Pillai 2010). Except for clump "6," all the other clumps in *R1* are below this threshold. Most clumps, however, will move above the empirical threshold when larger scales are kept by the spatial filtering, as in *R2*, *R3*, and *R4*. Most clumps (revealed in *R2*, *R3*, and *R4*) are above the predicted mass–radius relation for clumps undergoing quasi-isolated gravitational collapse in a turbulent medium (Li 2017). The clumps in G26, especially the dense and massive ones, are very likely bounded by gravity and have the ability to form high-mass stars.

We derived the thermal Jeans masses $M_J = 0.877\ M_\odot \left(\frac{T}{10\ K}\right)^{3/2} \left(\frac{n}{10^5\ {\rm cm^{-3}}}\right)^{-1/2}$ following Wang et al. (2014). The resulting n, N, and M_J are listed in the last three columns of

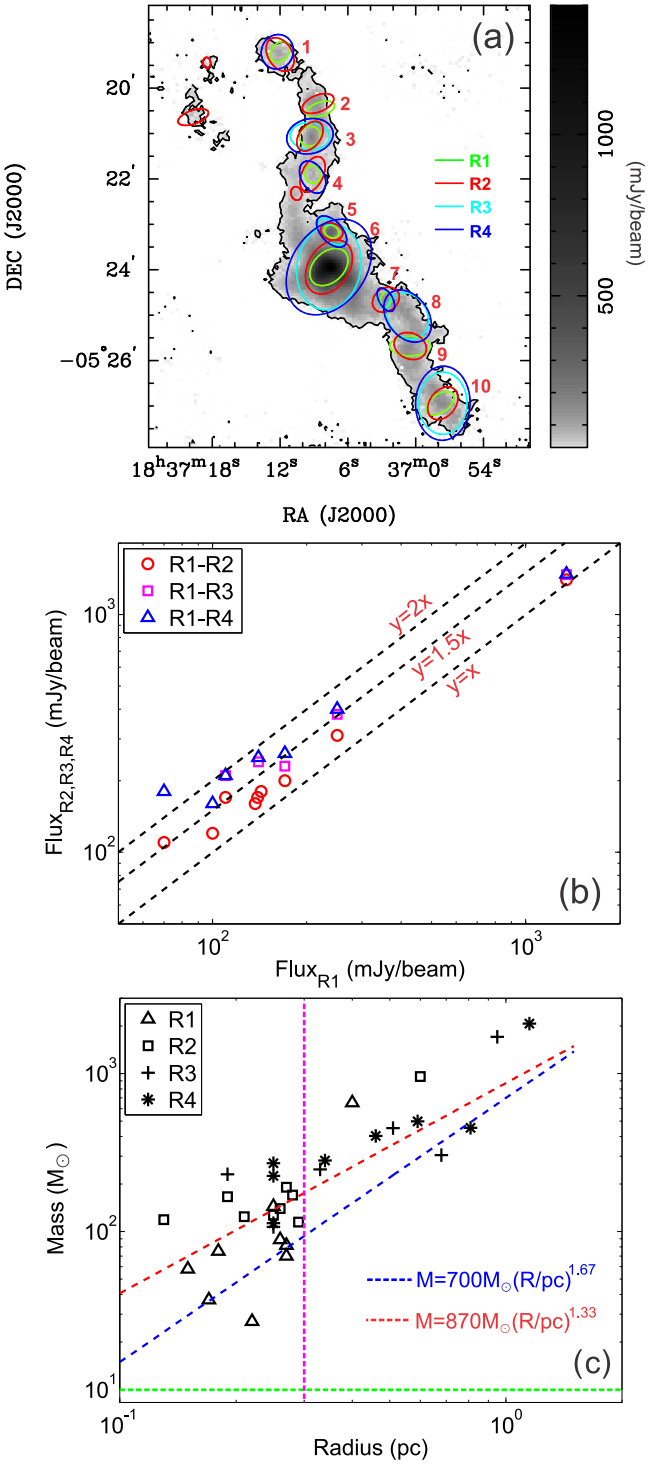

Figure 6. (a) 850 μm continuum emission in the *R2* reduction, shown in gray scale and black contours. The contour levels are the same as in the bottom panel of Figure 24. The green, red, cyan, and blue ellipses represent the dense clumps identified in the 850 μm continuum emission maps from the *R1*, *R2*, *R3*, and *R4* reductions, respectively. (b) Comparison of the peak fluxes of dense clumps in different data reductions. (c) Mass–radius relation of the dense clumps. The red dashed line shows a threshold to form high-mass protostars (Kauffmann & Pillai 2010). The blue dashed line shows the radius–mass relation for the clumps that undergo quasi-isolated gravitational collapse in a turbulent medium (Li 2017). Here we remind readers that the spatial resolution (beam size; magenta dashed line) of SCUBA-2 at 850 μm is ~0.3 pc and the 3σ mass sensitivity (black dashed line) is ~10 $M_\odot$ (assuming $T_d = 10$ K) at the distance of 4.2 kpc.

Table 1
Parameters of Dense Clumps

Clump No.	R.A. (J2000)	Decl. (J2000)	θ_{maj} (arcsec)	θ_{min} (arcsec)	P.A. (deg)	R_{eff} (pc)	F_{peak} (Jy beam^{-1})	F_{int} (Jy)	S/N	T_d[a] (K)	M ($M_\odot$)	n (10^4 cm^{-3})	N (10^{22} cm^{-2})	M_{Jeans} ($M_\odot$)
							R1							
1	18:37:12.00	−05:19:12.0	15	11	142	<0.26	0.10(0.01)	0.23(0.01)	7	10	89	>2.1	>2.2	<2
2	18:37:08.40	−05:20:27.6	19	9	108	<0.27	0.14(0.02)	0.35(0.02)	11	13	82	>1.7	>1.9	<3
3	18:37:09.36	−05:21:03.6	14	13	108	<0.27	0.17(0.02)	0.30(0.02)	13	13	70	>1.5	>1.6	<3
4	18:37:09.12	−05:21:54.0	12	10	191	<0.22	0.07(0.01)	0.10(0.01)	5	12	27	>1.1	>1.0	<4
5	18:37:07.44	−05:23:09.6	10	8	242	<0.18	0.25(0.03)	0.32(0.02)	20	13	75	>5.3	>3.9	<2
6	18:37:07.68	−05:23:56.4	29	20	133	0.40	1.35(0.14)	4.38(0.22)	103	17	654	4.2	7.0	3
7	18:37:02.64	−05:24:39.6	10	7	167	<0.17	0.11(0.01)	0.16(0.01)	9	13	37	>3.2	>2.2	<2
9	18:37:00.48	−05:25:40.8	27	13	90	0.25	0.14(0.01)	0.70(0.04)	11	14	144	3.8	3.9	2
10	18:36:57.84	−05:26:56.4	21	12	125	0.15	0.14(0.01)	0.46(0.02)	11	19	58	7.1	4.4	3
							R2							
1	18:37:12.00	−05:19:15.6	24	16	211	0.28	0.12(0.01)	0.44(0.02)	8	10	170	3.2	3.7	2
2	18:37:08.64	−05:20:20.4	22	11	112	0.13	0.16(0.02)	0.51(0.03)	10	13	119	22.5	12.0	1
3	18:37:09.36	−05:21:03.6	22	14	143	0.21	0.20(0.03)	0.53(0.03)	13	13	124	5.6	4.8	2
4	18:37:09.12	−05:21:54.0	25	14	155	0.25	0.11(0.01)	0.47(0.02)	7	12	127	3.4	3.5	2
5	18:37:07.44	−05:23:09.6	15	11	254	<0.26	0.31(0.04)	0.60(0.03)	20	13	140	>3.3	>3.5	<2
6	18:37:07.68	−05:23:56.4	39	27	147	0.60	1.40(0.12)	6.41(0.32)	88	17	957	1.8	4.5	5
7	18:37:02.64	−05:24:39.6	19	15	126	0.19	0.17(0.01)	0.71(0.04)	11	13	166	10.0	7.8	1
9	18:37:00.48	−05:25:40.8	22	17	247	0.27	0.17(0.02)	0.93(0.05)	10	14	191	4.0	4.5	2
10	18:36:57.60	−05:26:56.4	24	17	142	0.29	0.18(0.01)	0.91(0.05)	11	19	115	1.9	2.3	5
							R3							
3	18:37:09.36	−05:21:03.6	26	18	266	0.33	0.23(0.03)	1.20(0.06)	7	14	247	2.8	3.9	3
5	18:37:07.44	−05:23:09.6	22	13	230	0.19	0.38(0.05)	1.12(0.06)	12	14	230	13.9	10.9	1
6	18:37:07.68	−05:23:56.4	57	42	170	0.95	1.47(0.12)	11.44(0.57)	47	17	1708	0.8	3.2	7
7	18:37:02.64	−05:24:39.6	15	10	213	<0.25	0.21(0.02)	0.52(0.03)	7	14	107	>2.8	>2.9	<3
8	18:37:00.72	−05:25:01.2	32	26	209	0.51	0.22(0.02)	2.20(0.11)	7	14	452	1.4	3.0	4
10	18:36:57.60	−05:26:56.4	41	32	179	0.68	0.24(0.01)	2.42(0.12)	8	19	305	0.4	1.1	11
							R4							
1	18:37:12.24	−05:19:12.0	23	21	160	0.34	0.16(0.01)	1.04(0.05)	5	12	281	3.0	4.2	2
3	18:37:09.36	−05:21:03.6	31	23	103	0.46	0.26(0.03)	1.96(0.10)	9	14	403	1.7	3.2	4
4	18:37:09.12	−05:21:57.6	23	15	210	0.25	0.18(0.02)	0.96(0.05)	6	13	225	6.0	6.1	2
5	18:37:07.44	−05:23:09.6	25	14	223	0.25	0.40(0.05)	1.32(0.07)	13	14	271	7.2	7.4	2
6	18:37:07.68	−05:23:56.4	69	49	145	1.15	1.48(0.12)	13.87(0.69)	49	17	2071	0.6	2.7	8
7	18:37:02.64	−05:24:39.6	17	9	210	<0.25	0.21(0.02)	0.55(0.03)	7	14	113	>3.0	>3.1	<3
8	18:37:00.72	−05:25:01.2	38	27	217	0.59	0.23(0.02)	2.43(0.12)	8	14	499	1.0	2.4	5
10	18:36:57.60	−05:26:56.4	49	36	178	0.81	0.25(0.01)	3.60(0.18)	8	19	453	0.4	1.2	12

Note.
[a] T_d in *R1* and *R2* is derived from SED fit *S1*. T_d in *R3* and *R4* is derived from SED fit *S2*.

Table 2
Derived Parameters of Molecular Lines

Line	$\int T_b dv$[a] (K km s^{-1})	V_{LSR}[a] (km s^{-1})	FWHM[a] (km s^{-1})	T_{mb} (K)	T_{ex}[b] (K)	τ[b]	N[b] (cm^{-2})	X[c]
$C^{18}O$ $J = 1–0$	5.05(0.25)	48.23(0.05)	2.22(0.12)	2.14	18.2	0.1	4.6E15	1.0E–07
CH_3OH $7_0 - 6_1A+$	0.48(0.06)	47.90(0.02)	0.39(0.04)	1.16				
	0.64(0.07)	48.66(0.04)	0.79(0.11)	0.76				
HCO^+ $J = 1–0$	3.34(0.16)	50.95(0.04)	1.85(0.11)	1.70				
	2.51(0.20)	47.06(0.11)	3.15(0.36)	0.75				
$H^{13}CO^+$ $J = 1–0$	0.59(0.11)	49.78(0.12)	1.37(0.28)	0.40	3.9	0.5	1.9E13	4.2E–10
	0.86(0.12)	47.91(0.09)	1.46(0.23)	0.55	4.0	0.6	3.6E13	8.0E–10
HC_3N $J = 10–9$	2.43(0.18)	49.03(0.11)	3.07(0.27)	0.75	5.4	0.4	9.2E14	2.0E–08
HC_3N $J = 14–13$	1.18(0.19)	49.12(0.25)	3.07(0.55)	0.36	6.0	0.1		
HC_3N $J = 15–14$	0.52(0.13)	49.29(0.31)	2.37(0.55)	0.21	6.6	0.1		
SiO $J = 2–1$	1.57(0.40)	48.54(0.61)	7.28(1.23)	0.20	4.8	4.0	1.3E13	2.9E–10
	1.44(0.44)	37.16(2.29)	14.05(4.13)	0.10				
SiO $J = 3–2$	3.12(0.52)	44.34(1.75)	22.01(2.79)	0.13				
	0.63(0.24)	48.66(0.49)	4.44(1.45)	0.14	3.2	0.5	8.6E13	1.9E–09
$HN^{13}C$ $J = 1–0$	1.56(0.14)	49.06(0.14)	3.08(0.30)	0.48	3.5	1.0	2.5E14	5.6E–09
H_2CO $2_{1,2} - 1_{1,1}$	2.35(0.10)	50.81(0.04)	2.38(0.13)	0.93				
	1.32(0.09)	47.42(0.06)	1.87(0.17)	0.66				
	T_{ex}[d]	V_{LSR}[d]	FWHM[d]	τ	T_{ex}	τ	N	
CCH $N = 1–0$	4.4(0.3)	49.00(0.08)	3.02(0.20)	0.43(0.13)	4.5	0.4	1.5E14	3.3E–09
N_2H^+ $J = 1–0$	5.58(0.59)	47.72(0.03)	0.58(0.03)	1.88(0.54)	4.1	2.2	2.4E13	5.3E–10
	5.53(0.79)	50.05(0.03)	0.57(0.04)	1.66(0.62)	4.0	2.0	2.0E13	4.4E–10

Notes.
[a] From Gaussian fits with Gildas/Class.
[b] The values for $H^{13}CO^+$, HC_3N, and $HN^{13}C$ are derived by assuming a source size of 11″. The others are derived by assuming a filling factor of 1.
[c] $N_{H_2} = 4.5 \times 10^{22}$ cm^{-2}.
[d] From hyperfine structure fits with Gildas/Class.

Table 1. The clump masses are also about one order of magnitude larger than the corresponding thermal Jeans masses. The clumps are all located along the filament with a mean separation of ∼1.3 pc, which is much larger than the thermal Jeans length (∼0.1 pc for $T = 14$ K and the mean volume density $n = 6.2 \times 10^4$ cm^{-3} for clumps in *R2*), indicating that fragmentation in G26 is not governed by thermal instability but determined by other factors like turbulence or magnetic fields, as revealed in other IRDCs (e.g., Wang et al. 2011, 2014; Contreras et al. 2016).

The so-called "sausage instability" of a gas cylinder, proposed by Chandrasekhar & Fermi (1953) and promoted by many others (e.g., Stodólkiewicz 1963; Ostriker 1964; Inutsuka & Miyama 1992; Fiege & Pudritz 2000; Fischera & Martin 2012), has often been applied for studies of fragmentation in filamentary clouds (e.g., Jackson et al. 2010; Wang et al. 2011, 2014; Liu et al. 2017). In this scenario, an isothermal, hydrostatic, nonmagnetized, infinite filament becomes unstable and fragments into a chain of equally spaced fragments if its mass per unit length along the cylinder (or linear mass density) is close enough to the critical value so that perturbations in the filament have time to grow. In G26, the mean spacing and mass of clumps in G26 are ∼1.3 pc and ∼540 $M_\odot$, respectively, which were derived for clumps in *R4* reduction. The fragment mass in cylindrical fragmentation can be estimated as $M_{cl} = 575.3\ M_\odot \left(\frac{\sigma}{1\ \mathrm{km\ s^{-1}}}\right)^3 \left(\frac{n_c}{10^5\ \mathrm{cm^{-3}}}\right)^{-1/2}$; the typical spacing in cylindrical fragmentation is $\lambda_{cl} = 1.24\ \mathrm{pc} \left(\frac{\sigma}{1\ \mathrm{km\ s^{-1}}}\right) \left(\frac{n_c}{10^5\ \mathrm{cm^{-3}}}\right)^{-1/2}$ (Wang et al. 2014). σ is the 1D velocity dispersion and n_c is the volume density at the center of the cylinder. Here we take n_c as the mean number density (6.2×10^4 cm^{-3}) for clumps identified in *R2* reduction because *R2* filtered more extended emission than *R4*, and thus the mean number density for clumps in *R2* is much closer to the volume density at the center of the cylinder. If we only consider thermal pressure (assuming $T = 14$ K), the σ, M_{cl}, and λ_{cl} are 0.22 km s^{-1}, 7.8 $M_\odot$, and 0.35 pc, respectively. The M_{cl} and λ_{cl} are much smaller than the observed values in G26, indicating that thermal pressure alone cannot govern the fragmentation. However, if we also consider turbulent support, the σ, M_{cl} and λ_{cl} will become ∼0.94 km s^{-1} (estimated from $C^{18}O$ line width; see Table 2), 600 $M_\odot$, and 1.5 pc, respectively. The M_{cl} and λ_{cl} derived from turbulence-dominated cylindrical fragmentation are very consistent with the observed values (∼540 $M_\odot$ and ∼1.3 pc), suggesting that the fragmentation in G26 from cloud (at ∼10 pc scale) to clumps (at ∼1 pc scale) is very likely dominated by turbulence in the absence of magnetic fields. Limited by the spatial resolution (∼0.3 pc at the distance of 4.2 kpc) and mass sensitivity (3σ mass sensitivity is ∼10 $M_\odot$), we cannot study fragmentation from clump scale to core scale (at ∼0.1 pc scale) with the present data. Further fragmentation below the completeness and resolution limit of the present data is very likely to take place as seen in other IRDCs (Wang et al. 2011, 2014). The hierarchical fragmentation in G26 at all spatial scales can only be studied from higher spatial resolution interferometric observations.

4.3. Evidence for Grain Growth

Observationally, dust properties (e.g., opacity) greatly affect the determination of density and temperature profiles of dense cores and therefore influence the estimation of core masses. The dust grain size distributions in molecular clouds and cores can change with time because of grain sputtering, shattering, coagulation, and growth (Ormel et al. 2009). Grain growth in the densest and coldest

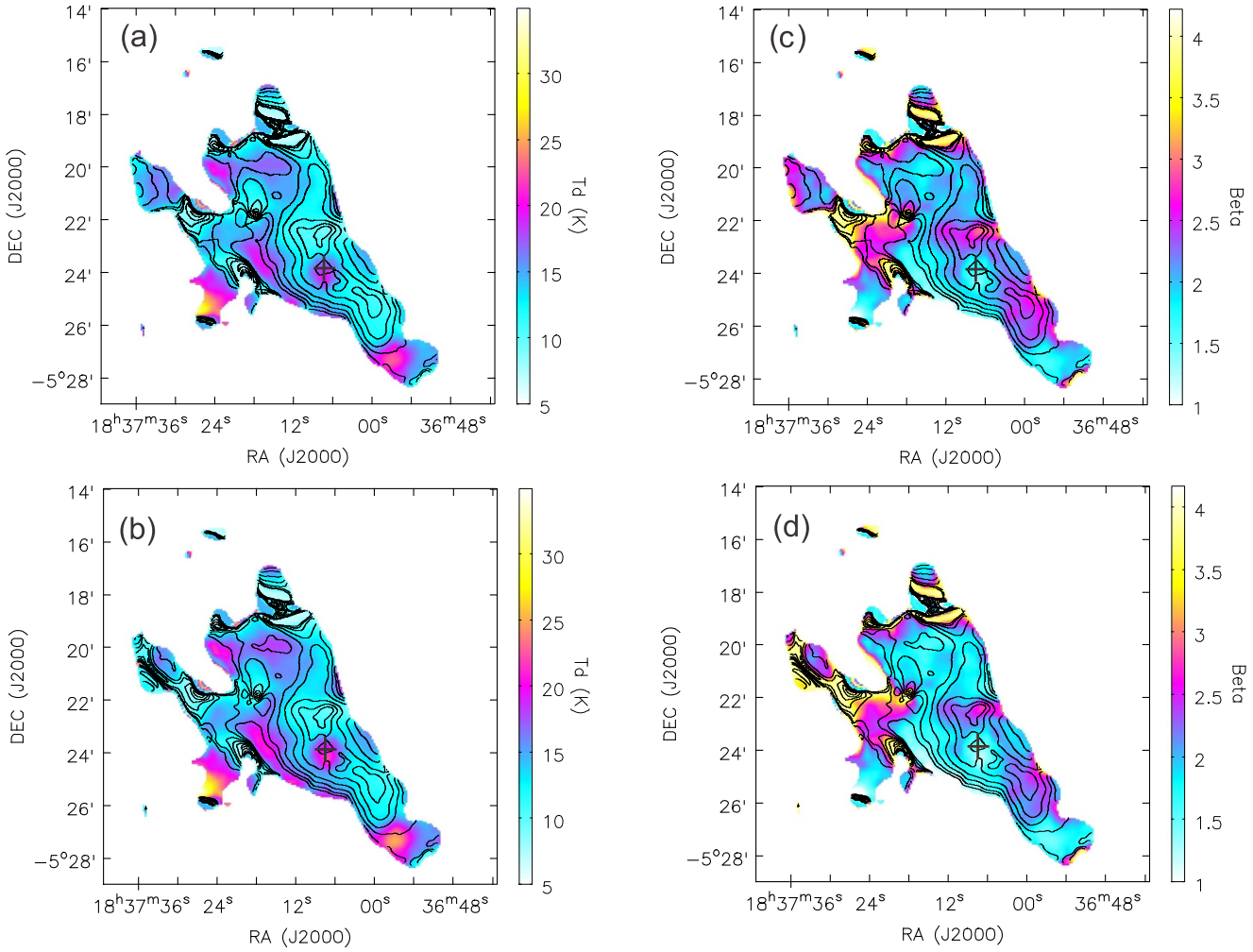

Figure 7. (a) Dust temperature map in the SED fit with free β using the *Herschel* data only shown in color scale. The 250 μm optical depth is shown with contours. The contour levels are [0.03, 0.05, 0.1, 0.2, 0.4, 0.6, 0.8] $\times$ 0.0282. (b) Dust temperature map in the SED fit with free β using both the *Herschel* and SCUBA-2 data shown in color scale. The 250 μm optical depth is shown with contours. The contour levels are [0.03, 0.05, 0.1, 0.2, 0.4, 0.6, 0.8] $\times$ 0.0211. (c) β map in the SED fit with free β using the *Herschel* data only, shown in color scale. The 250 μm optical depth is shown with contours. The contour levels are the same as in panel (a). (d) β map in the SED fit with free β using both the *Herschel* and SCUBA-2 data shown in color scale. The 250 μm optical depth is shown with contours. The contour levels are the same as in panel (b). The plus signs in the four panels mark the position of the most massive clump.

regions of interstellar clouds has been evidenced by an increase in the far-infrared opacity (Juvela et al. 2015a). Indeed, the dust spectral index (β) and its temperature (T_d) dependence can provide additional information on the chemical composition, structure, and size distribution of interstellar dust grains (Juvela et al. 2011). This dust emissivity change has been attributed to the formation of fluffy aggregates in the dense medium, resulting from grain coagulation.

Recently, Juvela et al. (2015a) studied dust optical depths by comparing measurements of submillimeter dust emission and the reddening of the light of background stars in the near-infrared (NIR) for a sample of 116 PGCCs in *Herschel* fields. In their studies, there are indications that β increases toward the coldest regions and decreases strongly near internal heating sources. Although NIR reddening is an independent and reliable measure of column density, NIR extinction could not, however, trace the densest portion of the cloud, due to low resolution. Additionally, the *Herschel* 250 μm band is less sensitive to very cold dust and may completely miss the highest column density peak (see Figure 2 in Pagani et al. 2015). *Herschel* 500 μm data could trace cold dust well but have relatively low angular resolution (35″). Adding high-resolution photometric data at longer wavelengths (e.g., 850 μm from SCUBA-2) could help more accurately derive the dust spectral index, dust temperature, and column density (N_{H_2}) simultaneously (Sadavoy et al. 2013; Chen et al. 2016).

For PGCC sources having *Herschel* data in the "SCOPE" survey, we will determine the dust emissivity spectral index (β), dust temperature (T_d), and column density (N_{H_2}) simultaneously by combining 850 μm data with spatially filtered *Herschel* photometric data. Since the PGCC sources are at different stages of cloud evolution from starless clumps to protostellar cores and are located in different Galactic environments, we will search for variations of β that might be attributed to the evolutionary stage of the sources or to environmental factors, including the location within the Galaxy and stellar feedback. A pilot study of dust properties toward ~100 PGCCs with *Herschel* data and SCUBA-2 data will be presented in Juvela et al. (2017). Below we investigate the dust properties of G26 as an example.

In Figure 7, we present the T_d, β, and τ_{250} maps of G26 from SED fits with free β and T_d. The extended emission larger than 600″ in the *Herschel* and SCUBA-2 maps (from imaging scheme *R4*; see Section 6.2 in Appendix A) was filtered out. In general, the β map is anticorrelated with the T_d map. The most massive core, marked with a black plus sign, clearly shows higher temperature and lower β than its surroundings. The low β may indicate grain

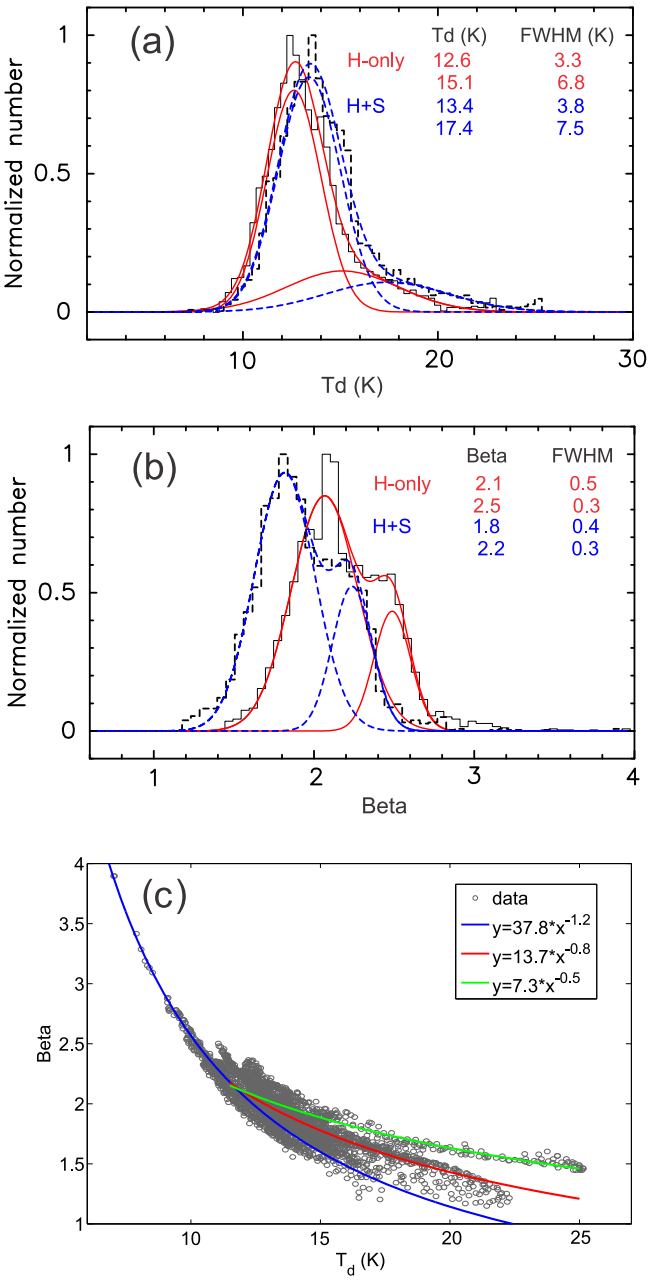

Figure 8. (a) Histograms of T_d. The T_d in the SED fit with free β using the *Herschel* data only is shown with solid lines, while the T_d in the SED fit with free β using both the *Herschel* and SCUBA-2 data is shown with dashed lines. The red and blue color lines show the normal distribution fits. (b) Histograms of β. The β in the SED fit with free β using the *Herschel* data only is shown with solid lines, while the β in the SED fit with free β using both the *Herschel* and SCUBA-2 data is shown with dashed lines. The red and blue color lines show the normal distribution fits. (c) Spectral index β vs. dust temperature T_d in the SED fit with free β using both the *Herschel* and SCUBA-2 data. The blue line shows the power-law fit toward the data with $T_d < 10$ K. The red line shows the power-law fit toward the data with $T_d > 10$ K. The green line outlines the trend for the data with $T_d > 15$ K and high β.

growth during core or star formation. Figures 8(a) and (b) show histograms of T_d and β. Only the data points with S/N > 10 in the SCUBA-2 map, corresponding to the ridge region of the filament, are included in the statistics. In general, including 850 μm data tends to increase the T_d by ~1 K and lower β by ~0.3. The dust temperature histograms show a high-temperature tail, which is caused by ongoing star formation. Interestingly, the β histograms can be well fitted with two normal distributions regardless of whether or not 850 μm data were included in the SED fits. Such a bimodal behavior in β distribution may suggest grain growth along the filament.

Figure 8(c) presents the correlation between T_d and β. β is generally anticorrelated with T_d. Interestingly, the β versus T_d correlations can be roughly depicted with three power laws, which again indicates the existence of different kinds of dust grains in the filament. Such an anticorrelation between T_d and β was also found in all Perseus clumps (Chen et al. 2016). Chen et al. (2016) also found that these anticorrelations cannot be solely accounted for by anticorrelated T_d and β uncertainties associated with SED fitting. The anticorrelation may be partially explained by the dust grains' intrinsic β dependency on temperature, but more likely by the sublimation of surface ice mantles, which can increase β when present on a dust grain (Chen et al. 2016). A thorough investigation of the correlation between T_d and β is beyond the scope of this paper. We will systematically study this issue in the future with more "SCOPE" objects.

4.4. Cloud Structure

To understand better the star or core formation process, it is crucially important to study their parent molecular cloud properties. SCUBA-2 has better resolution and longer wavelengths than *Herschel*/SPIRE bands and thus is more suitable to trace the cold ISM. Due to variations of the atmosphere that mimic emission from extended astronomical objects, SCUBA-2 data are not well suited to capture the extended structures in molecular clouds. The loss of the filtered emission by SCUBA-2, however, can be somewhat corrected based on the *Planck* data. The combined *Planck* 353 GHz data and the SCUBA-2 850 μm data will be used to investigate the density distribution and structures at various cloud scales. Below we use G26 to demonstrate the combination of the *Planck* and SCUBA-2 data.

We combined the *Planck* 353 GHz image with the SCUBA-2 850 μm images in the *R2* and *R4* reductions following the same procedure as in Lin et al. (2016, 2017). In principle, the data combination was performed in the Fourier domain, yielding high-resolution (14″) combined data that have little or no loss of extended structure (Lin et al. 2016, 2017). The combined images are shown in Figure 9(a). In general, the two images show very similar morphology and flux density. From these combined images, we find that the dense filament resides in a cloud with very smooth structures. The cloud boundary is well enclosed by the 10% contours in Figure 9(a). Particularly, the dense filament is close to the cloud edge, indicating possible dynamical clues to its formation (e.g., external compression).

Figure 9(b) presents the dust temperature and column density maps obtained from SED fits with *Herschel*/PACS 160 μm, *SPIRE* 250/350 μm and combined *Planck*+SCUBA-2 850 μm data in *R2* reduction. The final dust temperature and column density maps have an angular resolution of 25″. The temperature map clearly reveals a temperature gradient from southeast to northwest.

To quantify the dense gas distributions systematically, we perform analyses of the column density probability distribution functions (N-PDF) following Lin et al. (2016, 2017). The natural logarithm of the ratio of column density and mean column density is $\eta = ln(N_{H_2}/\langle N_{H_2}\rangle)$, and the normalization of the probability function is given by $\int_{-\infty}^{+\infty} p(\eta)d\eta = \int_{0}^{+\infty} p(N_{H_2})d(N_{H_2}) = 1$. Figure 9(c) shows the column density probability distribution functions (N-PDF). The N-PDF in molecular clouds is usually

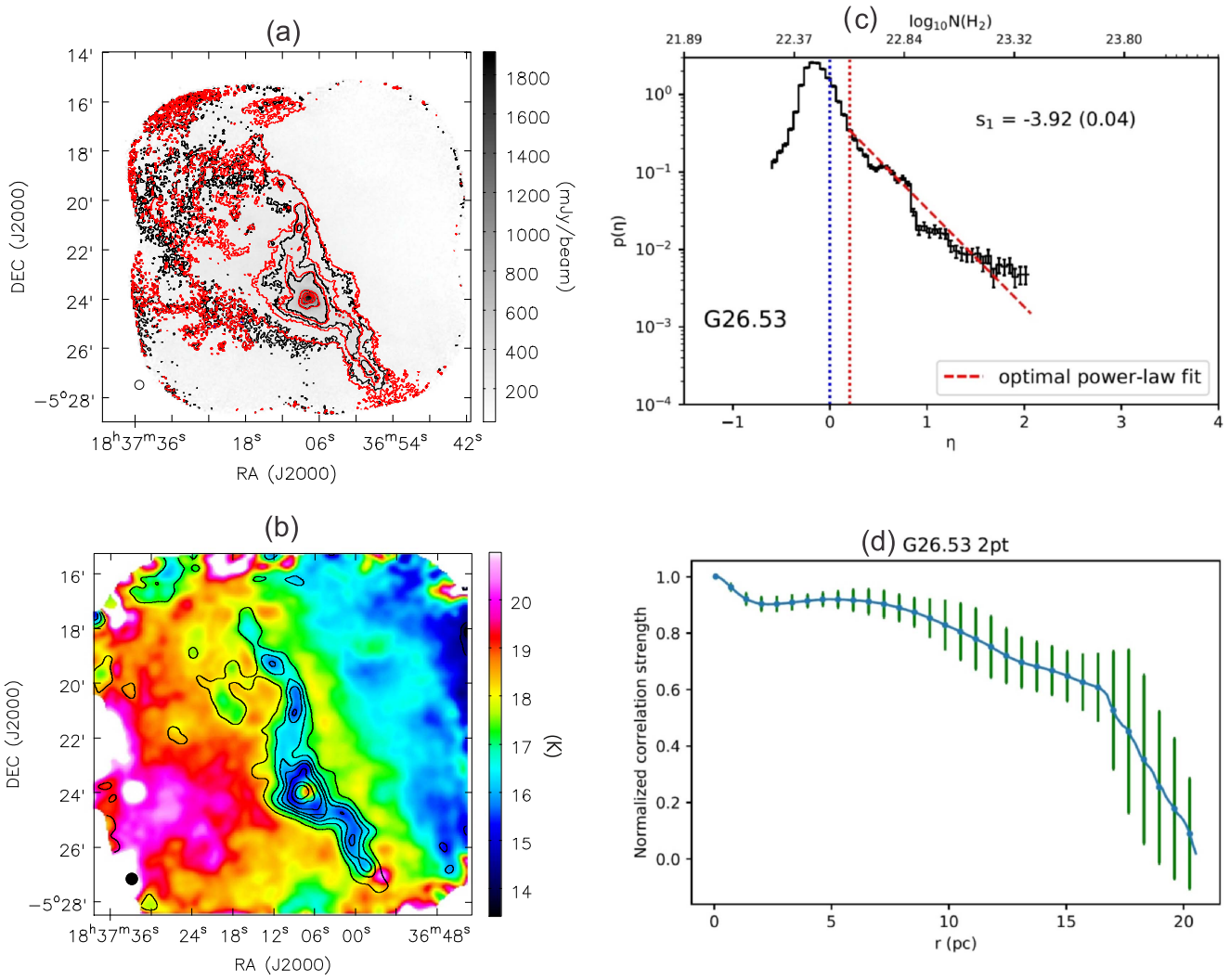

Figure 9. (a) Grayscale image and black contours show the 850 μm continuum emission from combined *Planck* data and SCUBA-2 data in *R2*. The contour levels are [0.1, 0.15, 0.2, 0.4, 0.6, 0.8] $\times$ 1.92 Jy beam^{-1}. The red contours show the 850 μm continuum emission from combined *Planck* data and SCUBA-2 data in *R4*. The contour levels are [0.1, 0.15, 0.2, 0.4, 0.6, 0.8] $\times$ 1.97 Jy beam^{-1}. (b) Dust temperature map from SED fits with *Herschel* and combined *Planck* and SCUBA-2 850 μm data in *R2*, shown in color scale. The column density map is shown with contours. The contour levels are [0.15, 0.2, 0.4, 0.6, 0.8] $\times$ 2.76 $\times$ 10^{23} cm^{-2}. (c) Column density probability distribution function (N-PDF). The blue vertical dashed line marks the mean column density of $\sim$3.3 $\times$ 10^{22} cm^{-2}. The red vertical dashed line shows the starting column density ($\sim$4 $\times$ 10^{22} cm^{-2}) of the power-law fit. (d) Two-point correlation functions of the column density distribution.

found to consist of a lognormal like part at low column density and a power-law-like part at high column density (Klessen 2000; Kritsuk et al. 2011; Schneider et al. 2012, 2015; Federrath & Klessen 2013; Lin et al. 2016, 2017). The N-PDF power-law tail is usually linked to the effects of gravity (Klessen 2000; Kritsuk et al. 2011; Federrath & Klessen 2013; Lin et al. 2016, 2017). We tried to fit the tail with a power law for the N-PDF of G26. Although the power-law fit is poor, its slope ($-$3.9) is comparable to those of IRDCs G28.34+0.06 ($-$3.9) and G14.225–0.506 ($-$4.1) but smaller than those of protoclusters (Lin et al. 2016, 2017), indicating that G26 is still at a very young evolutionary stage and is not greatly affected by star formation activities as in high-mass protoclusters.

To diagnose the characteristic spatial scales in G26, we determine the two-point correlation functions (2PT) of gas column density following Lin et al. (2016, 2017). Figure 9(d) shows the two-point correlation (2PT) function of column densities in the observed field. The correlation strength at a separation scale (lag) of l is calculated by

$$S_{tr}(l) = \frac{\langle X(\boldsymbol{r})X(\boldsymbol{r}+\boldsymbol{l})\rangle_l}{\langle X(\boldsymbol{r})X(\boldsymbol{r})\rangle_l}, \quad (1)$$

where $X(\boldsymbol{r})$ denotes the column density value at position $\boldsymbol{r}$, and the angle brackets are an average over all pairs of positions with a separation of l. The final form of the correlation function is normalized by the peak correlation strength to enable comparisons between different fields. For a more detailed description, see Lin et al. (2016, 2017).

In general, the 2PT function shows a smooth decay of correlation strengths over all spatial scales up to $\sim$15 pc. Such a flat profile in the 2PT correlation is also witnessed toward IRDCs like G11.11–0.12 (see Figure 5 in Lin et al. 2017) but is in contrast with most of the active OB-cluster-forming regions, which have a steep decay of correlation strength at small spatial scales (Lin et al. 2016). The flat 2PT correlation indicates that the column density distribution of G26 is very homogeneous over all spatial scales

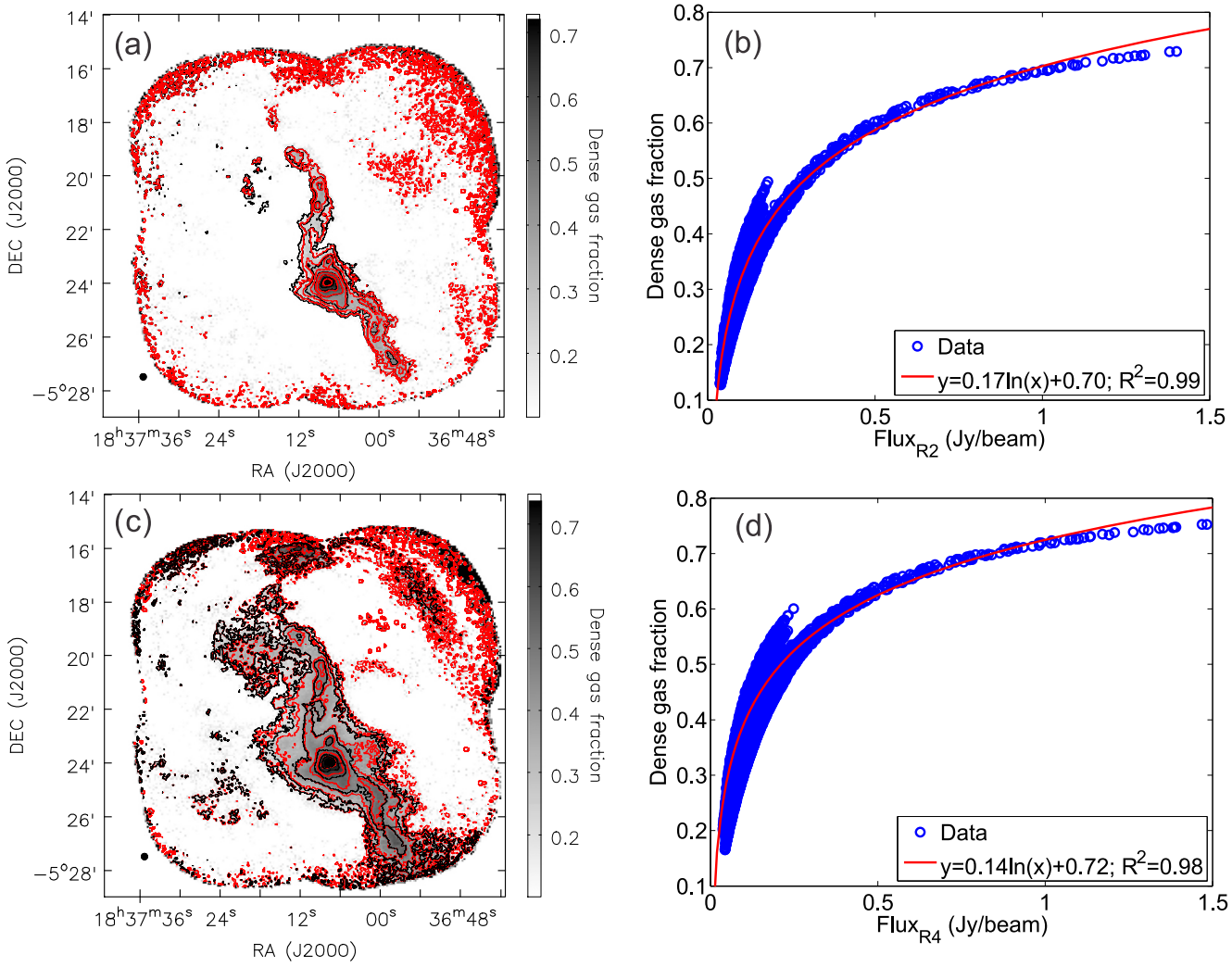

Figure 10. (a) Dense gas fraction in *R2* reduction shown in gray scale and red contours. The contour levels are [0.2, 0.3, 0.4, 0.5, 0.6, 0.7]. The 850 μm continuum emission in *R2* reduction is shown in black contours. The contour levels are the same as in the bottom panel of Figure 24. (b) Dense gas fraction vs. the 850 μm continuum flux density in the *R2* reduction. The red line shows the logarithmic function fit toward the pixels with flux density larger than 200 mJy beam^{-1} in the SCUBA-2 image. (c) Dense gas fraction in *R4* reduction shown in gray scale and red contours. The contour levels are [0.2, 0.3, 0.4, 0.5, 0.6, 0.7]. The 850 μm continuum emission in *R4* reduction is shown with black contours. The contour levels are the same as in Figure 25(b). (d) Dense gas fraction vs. the 850 μm continuum flux density in the *R4* reduction. The red line shows the logarithmic function fit toward the pixels with flux density larger than 300 mJy beam^{-1} in the SCUBA-2 image.

larger than 1 pc and the mass is less concentrated overall than in high-mass protoclusters.

The N-PDF and 2PT are powerful tools to investigate the cloud structure evolution and should be applied to other SCOPE fields.

4.5. Dense Gas Fraction

The empirical power-law relation between the star formation rate (SFR), surface density ($\Sigma_{\rm SFR}$), and surface density of cold gas ($\Sigma_{\rm gas}$) pioneered in the works of Schmidt (1959) and Kennicutt (1998), the so-called Kennicutt–Schmidt (KS) law, is of great importance as an input for theoretical models of galaxy evolution. Recently, nearly linear correlations between star formation rates and line luminosities of dense molecular gas tracers (e.g., HCN and CS) have been found toward both Galactic dense clumps and galaxies (Gao & Solomon 2004; Wu et al. 2005, 2010; Lada et al. 2010; Zhang et al. 2014; Liu et al. 2016a; Stephens et al. 2016), strongly suggesting that star formation is mainly related to dense gas in molecular clouds. Therefore, it is important to evaluate the proportions of dense gas in molecular clouds. As discussed in Liu et al. (2016a), the relation between star formation rates and clump masses (traced by filtered continuum maps) is as tight as correlations between star formation rates and line luminosities of dense gas tracers (e.g., HCN, CS). Particularly, filtered continuum maps have advantages to trace the total dense gas masses rather than dense gas tracers (e.g., HCN, HCO$^+$, CS), whose emissions are usually optically thick (Liu et al. 2016a). Since the filtered SCUBA-2 images intrinsically filter the large-scale diffuse gas and are most sensitive to the high volume densities ($\sim 10^4$ cm^{-3} for G26) in clouds, the flux ratio between the SCUBA-2 data and the *Planck*+SCUBA-2 combined data is well representative of the dense gas fraction in the cold dust ($f_{\rm DG}$), as also suggested in Csengeri et al. (2016).

Figures 10(a) and (c) show the dense gas fraction maps for G26. In general, the dense gas fraction increases with column density. In panels (b) and (d), we investigate the relationship between the dense gas fraction and flux density for the pixels with S/N > 5 in the SCUBA-2 images. The correlations can be well fitted with logarithmic functions toward high flux density points. The logarithmic function fits can also extend to low flux density points even though the low flux density points

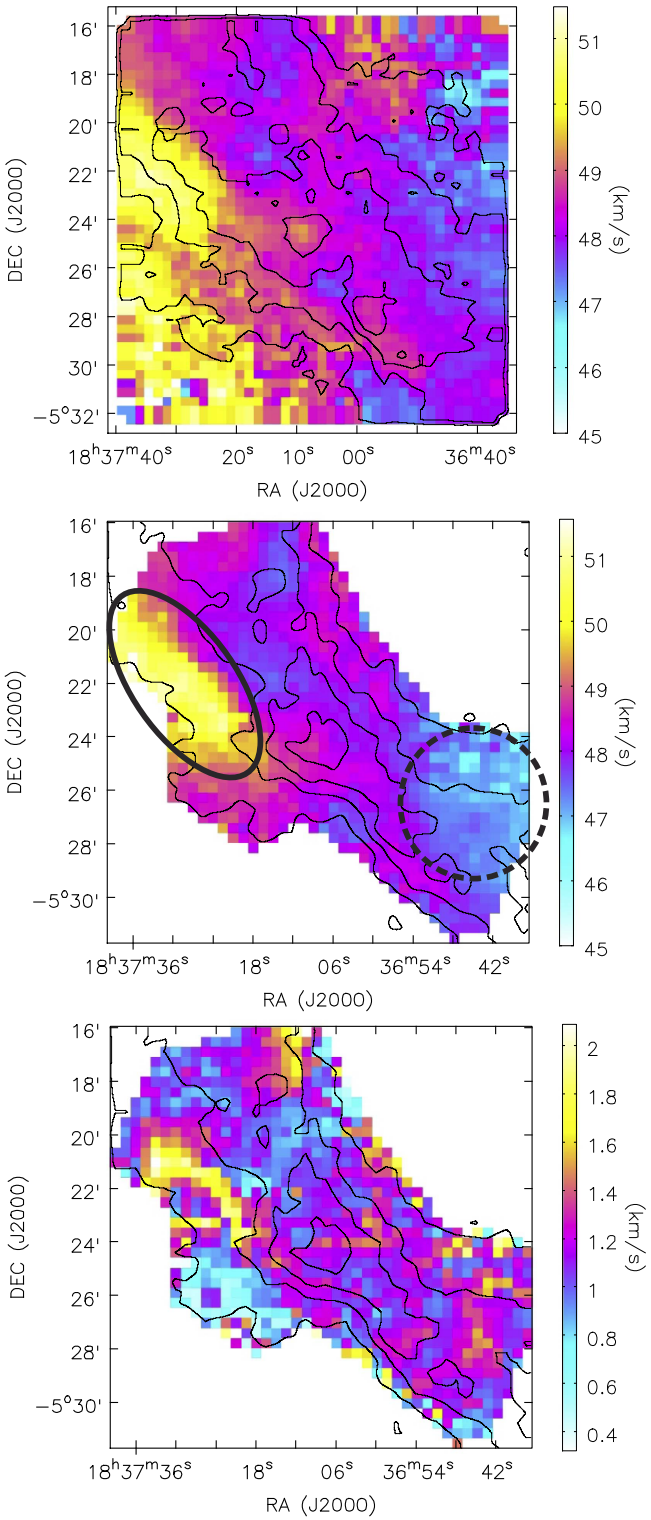

Figure 11. Top panel: ^{12}CO (1–0) integrated intensity contours overlaid on its first-moment map. Middle panel: ^{13}CO (1–0) integrated intensity contours overlaid on its first-moment map. The dashed circle and solid ellipse mark the regions that show large velocity gradients. Bottom panel: ^{13}CO (1–0) integrated intensity contours overlaid on its second-moment map. The contours for both ^{12}CO (1–0) and ^{13}CO (1–0) are from 20% to 80% in steps of 20% of the peak values. The peak integrated intensities of ^{12}CO (1–0) and ^{13}CO (1–0) are 56 and 20 K km s^{-1}, respectively.

show much larger scatter. The $f_{\rm DG}$ in the image from *R2* reduction range from 0.13 to 0.73 with a median value of 0.30, while the $f_{\rm DG}$ in the image from *R4* reduction range from 0.17

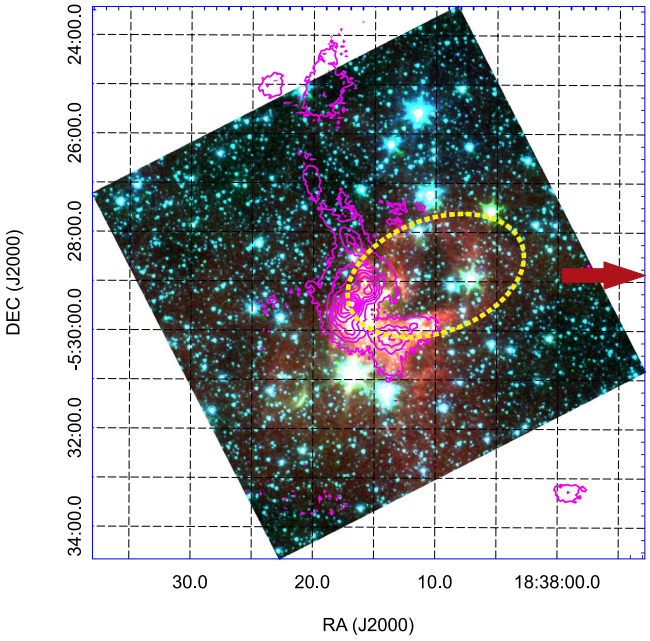

Figure 12. *Spitzer*/IRAC three-color (3.6 μm in blue, 4.5 μm in green, and 8 μm in red) composite image of the G26 bubble region. The magenta contours represent the SCUBA-2 850 μm continuum emission. The contour levels are [0.1, 0.2, 0.3, 0.4, 0.5, 0.6, 0.7, 0.8, 0.9] × 958.6 mJy beam^{-1}. The yellow dashed ellipse outlines the infrared bubble. The red arrow marks the direction of G26.

to 0.75 with a median value of 0.37. The dense gas fractions determined from images with different spatial filters are slightly different but only vary less than ∼10%. It seems that only 30%–40% of the cloud gas in G26 is dense.

4.6. On the Origin of the Dense Filament

4.6.1. Evidence for Large-scale Compression Flows

The origin of dense filaments in giant clouds still remains a puzzle to astronomers (André et al. 2014). Filaments have been well predicted in simulations of supersonic turbulence in the absence of gravity, which can produce hierarchical structure with a lognormal density distribution seen in observations (Vázquez-Semadeni 1994). Filaments in strongly magnetized turbulent clouds (e.g., B211/3, Musca; Cox et al. 2010; Palmeirim et al. 2013) are oriented preferentially perpendicular to the magnetic field lines, suggesting an important role of magnetic fields in filament formation. Filamentary structures in the Galaxy are preferentially aligned parallel to the Galactic midplane and therefore with the direction of large-scale Galactic magnetic field, suggesting a possible connection between large-scale Galactic dynamics and filament formation (Wang et al. 2015, 2016; Li et al. 2016). The formation of filaments by self-gravitational fragmentation of sheet-like clouds has been seen in simulations of 1D compression (e.g., by an expanding H II region, an old supernova remnant, or the collision of two clouds; Inutsuka et al. 2015; Federrath 2016; Li et al. 2018). For example, the asymmetric column density profiles of filaments in the Pipe Nebula are most likely the result of large-scale compressive flows generated by the winds of the nearby Sco OB2 association (Peretto et al. 2012).

The "SCOPE" survey aims to resolve *Planck* cold clumps and reveal their substructures. We will assess the detection rate of filaments in *Planck* cold clumps in different environments (e.g., spiral arms, interarms, high latitude, expanding H II regions, supernova remnants). In conjunction with molecular line data from the "TOP" and "SAMPLING" surveys, which provide

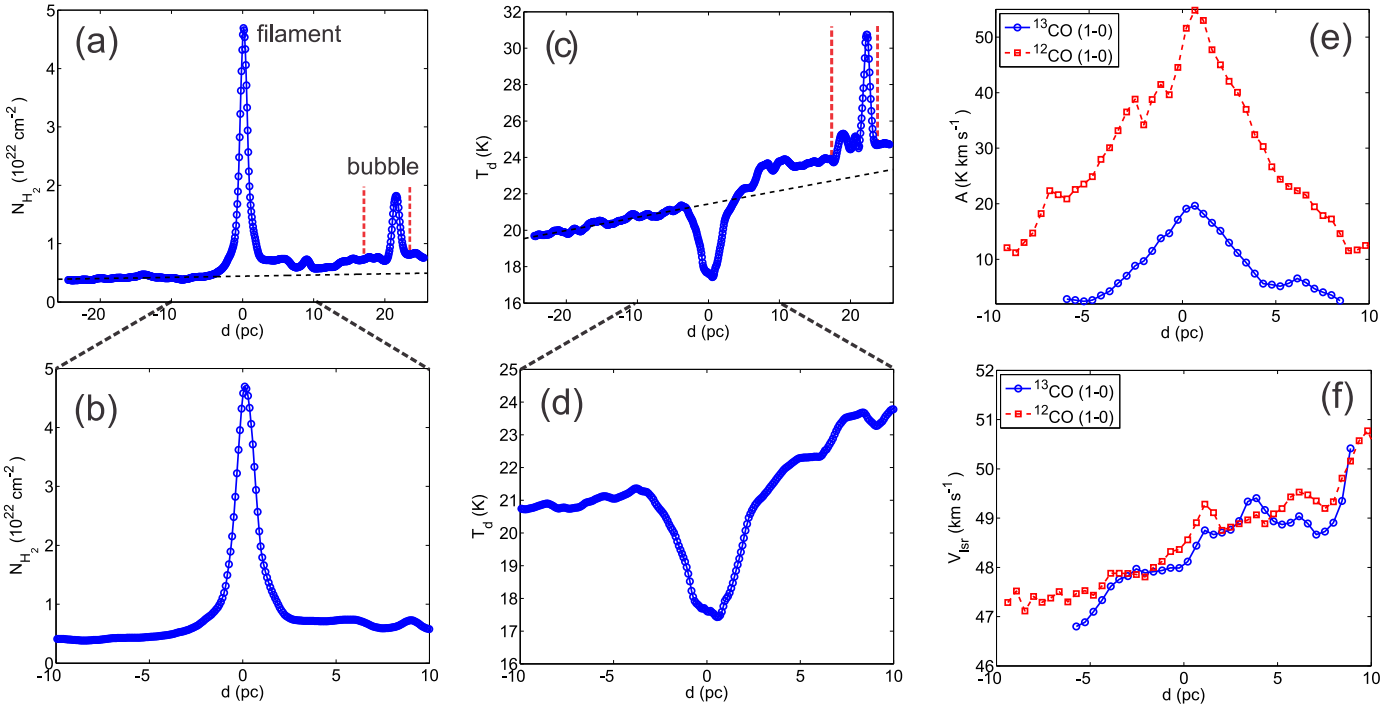

Figure 13. Variation of (a, b) column density, (c, d) dust temperature, (e) integrated intensity, and (f) intensity-weighted velocity of ^{12}CO (1–0) and ^{13}CO (1–0), along the yellow dashed line across the filament seen in the top panel of Figure 23. The distances are calculated with respect to the peak of the filament. The black dashed lines in panels (a) and (c) are linear fits toward the positions (−25 to 5 pc) behind the filament. The red dashed lines in panels (a) and (c) mark the bubble region.

kinematic information, we will be able to study the formation mechanisms of dense filaments in widely different environments. Below we present evidence of compression flows that may be responsible for the formation of the G26 filament.

As shown in the top panel of Figures 23 and 9(b), the temperature gradient on large scales is perpendicular to the dense filament G26. Figures 11(a)–(b) present maps of the first moment of ^{12}CO (1–0) and ^{13}CO (1–0), respectively. The maps reveal large-scale velocity gradients along the NW–SE direction across the whole map. The temperature gradient suggests an asymmetric heating source. Together with the velocity gradient, one can think of compression flows from the left.

The origin of the large-scale compression flows is unclear. To the east of G26, we found an infrared bubble. Figure 12 shows a three-color composite *Spitzer*/IRAC image of the infrared bubble region overlaid with SCUBA-2 850 μm continuum emission in contours. As shown in Figure 13, the locations between the bubble and the filament have higher column density (∼1.6 times higher) and higher temperature (∼3 K higher) than the locations west of the filament, suggesting that a pressure gradient exists from the southeast to northwest. Also, the filament shows an asymmetric column density profile (panels (a) and (b)), again indicating that it may be compressed by external pressure from its southeast side. Panels (e) and (f) present the variance of the integrated intensity and intensity-weighted velocity of ^{12}CO (1–0) and ^{13}CO (1–0) line emission, respectively. Both ^{12}CO (1–0) and ^{13}CO (1–0) line emissions reveal a large-scale velocity gradient (∼0.16 km s^{-1} pc^{-1}) perpendicular to the filament, again suggesting the existence of compression flows.

Note that the infrared bubble only has an extent of ∼5 pc and is ∼15 pc away in projection from the filament G26 (see Figures 23(a) and 26(a) in Appendix A). Hence, the bubble may not have the ability to generate the large-scale compression flows. Since the G26 filament is parallel to the Galactic plane (see Figure 4), the large-scale compression flow may originate from the ram pressure from the OB associations in the Galactic plane. In any case, the higher pressure to the southeast of G26 can continuously sweep up the interstellar gas to feed the dense filament.

Although the infrared bubble seems not to be responsible for the origin of the filament, it may have great impact on its surroundings. The clumps (shown in magenta contours in Figure 12) adjacent to its east seem to be compressed by the bubble and the star formation in those clumps may be triggered by the bubble as revealed near other infrared bubbles (e.g., Liu et al. 2012b, 2015, 2016). More detailed studies of those clumps adjacent to the bubble will be present in another work.

4.6.2. Collisions of Subfilaments?

Figure 14 presents channel maps of the $J = 1$–0 transitions of ^{12}CO, ^{13}CO, and C^{18}O lines. In contrast to the 850 μm continuum emission, the molecular line emission reveals more complicated structures. Several velocity coherent subfilaments (F1 to F6) can be identified from the channel maps. The position angles of F1, F2, F3, F4, F5, and F6 are about 45°, 115°, 0°, 44°, 80°, and 20°, respectively. The subfilaments F3, F4, and F6 are also seen in SMT ^{13}CO (2–1) channel maps (see Figure 15). Those subfilaments have noticeable differences in velocity because they emerge in different velocity channels.

F4 and F6 form the main gas subfilament, most of whose emission is in the 47–48 km s^{-1} channels. F1, which has the most redshited velocities among the subfilaments, is located to the northwest and only appears in the 51–53 km s^{-1} channels. F1 seems to interact with the main filament (F6), as well as another sub-filament (F2). The interface between F1 and F6 shows much larger velocity dispersion, as revealed in the second-moment map of ^{13}CO (1–0) emission (see the bottom panel of Figure 14). F5 has more blueshifted velocities than other subfilaments. It is connected to F4. The G26 filament as revealed

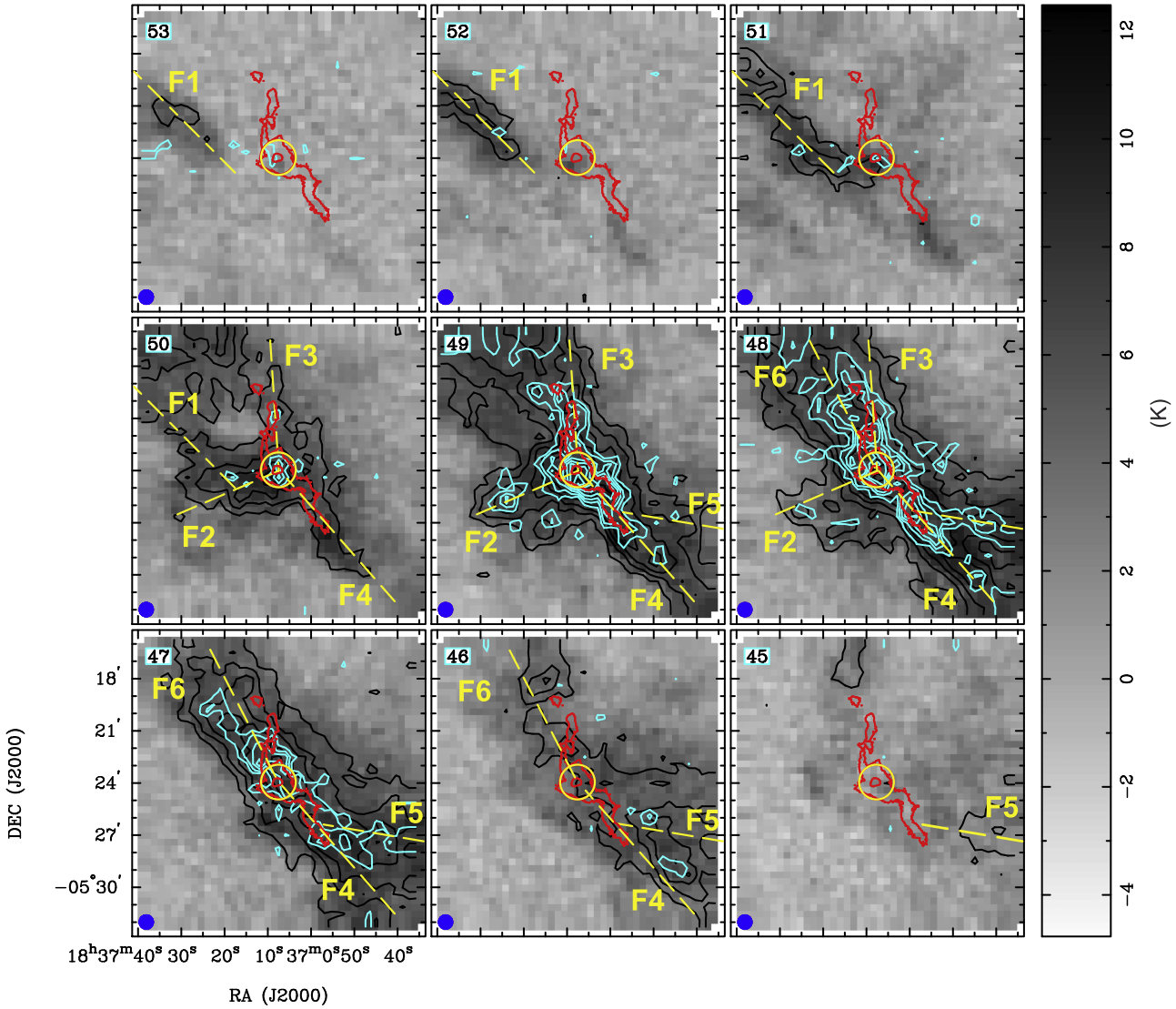

Figure 14. Channel maps of $J = 1$–0 transitions of ^{12}CO (grayscale images), ^{13}CO (black contours), and C^{18}O (blue contours). The contour levels for ^{13}CO are from 10% to 90% in steps of 10% of the peak intensity (8.2 K). The contour levels for ^{13}CO are from 10% to 90% in steps of 10% of the peak intensity (3.0 K). The yellow circles mark the central massive clump. The yellow lines outline the subfilaments. The red contours show the SCUBA-2 850 μm continuum emission in the *R2* data reduction. The contour levels are [0.05, 0.5] $\times$ 1.40 Jy beam^{-1}.

by SCUBA-2 850 μm continuum has a curved (or "S"-type) shape, suggesting that it may be dynamically interacting with its surroundings (Wang et al. 2015, 2016). The continuum filament is mainly associated with the F3 and F4 gas subfilaments. Interestingly, F3 is clearly offset from the axis of the main gas filament (F6) and has redshifted velocities with respect to F6. F3 may be compressed owing to a collision between F1 and F6. The collision may have reshaped the continuum filament into a curved shape. F5 may also collide with F4 and reshape the southern arm of the continuum filament. With the detection of several subfilaments in G26 and because IRDCs are at the very early stages of star formation, we add further support to the idea that IRDCs are in a stage in which they are still being assembled (Jiménez-Serra et al. 2010; Sanhueza et al. 2013).

4.6.3. Filament Accretion

Figure 16 presents position–velocity diagrams of ^{13}CO (2–1) line emission along subfilaments F3, F4, and F6. The peak emission of clump 6 is significantly blueshifted with respect to the systemic velocity and the main subfilament. As denoted by yellow dashed lines, the subfilaments connected to the central clump show clear velocity gradients with respect to the peak emission of the central clump. The velocity gradients are ~0.4, ~0.6, and 0.5 km s^{-1} pc^{-1} for "F3," "F4," and "F6," respectively, which are similar to the values found in other Galactic long filaments (Wang et al. 2016).

One interpretation of velocity gradients is that they are caused by inflows along the subfilaments as also seen in other filamentary clouds (Kirk et al. 2013; Peretto et al. 2013; Liu et al. 2016c; Yuan et al. 2018). The velocity differences (δV) between the subfilaments and central clump become larger as they approach the central clump (i.e., $\delta V \propto \delta R^{-1}$, where δR is the distance to the central clump), suggesting that the inflows along the subfilaments are likely driven by the gravity of the central clump MM6.

We can estimate the mass inflow rate ($\dot{M}_{\parallel}$) along filaments following Kirk et al. (2013):

$$\dot{M}_{\parallel} = \frac{\nabla V_{\parallel,\rm obs} M}{\tan(\alpha)}, \quad (2)$$

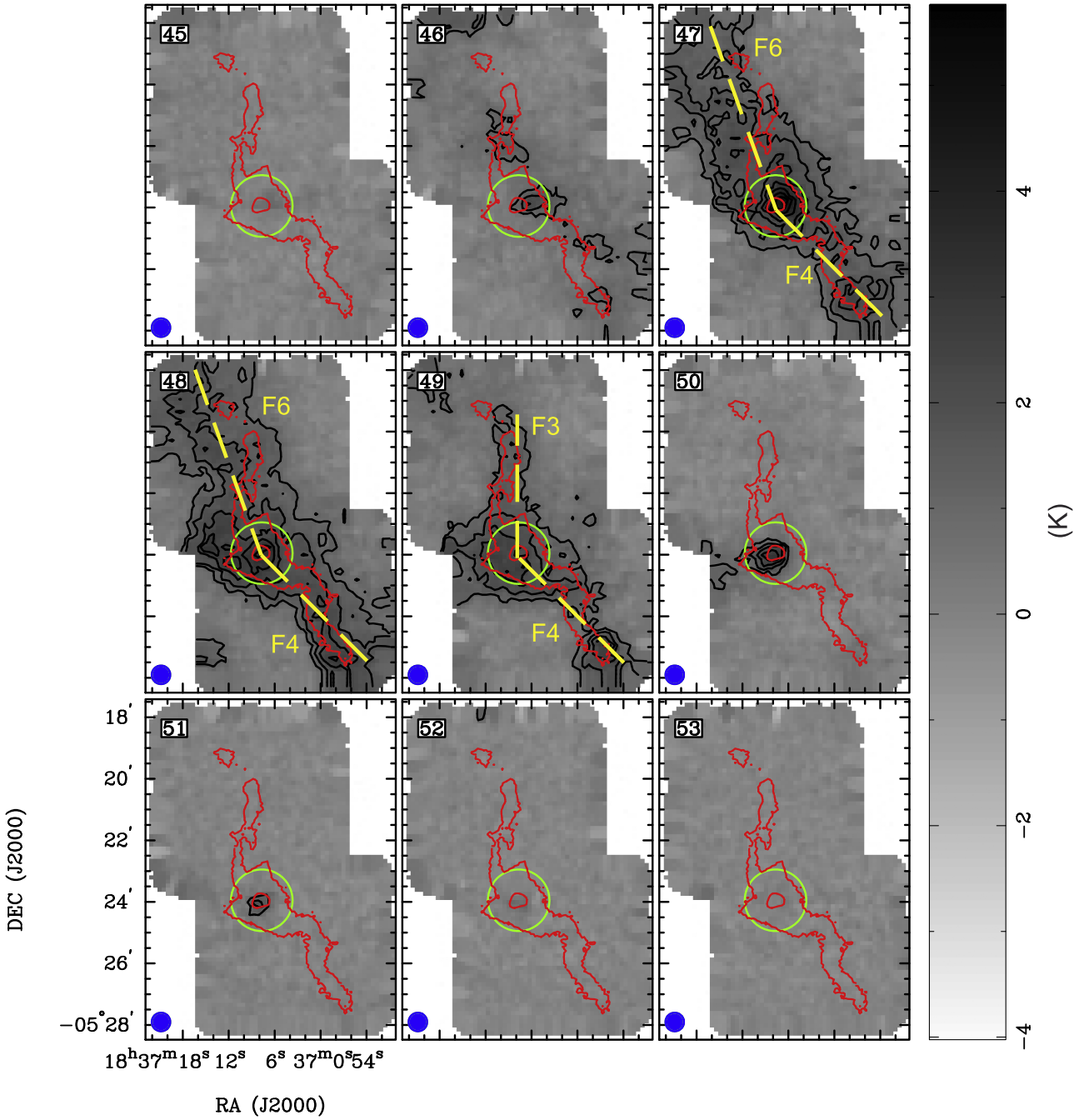

Figure 15. Channel maps of ^{13}CO (2–1) line emission. The contour levels for ^{13}CO are from 20% to 90% in steps of 10% of the peak intensity (5.8 K). The yellow dashed lines outline the directions of position–velocity cuts in Figure 16. The green circles mark the central massive clump. The red contours show the SCUBA-2 850 μm continuum emission in the *R2* data reduction. The contour levels are [0.05, 0.5] × 1.40 Jy beam^{-1}.

where $\nabla V_{\parallel,\rm obs}$, M, and α are the velocity gradient, mass, and inclination angle with respect to the plane of the sky of a filament, respectively. Since most gas is bounded in dense clumps, only a small fraction of free gas may be accreted along the filament. We estimated the mass of the free gas as the difference (∼1900 $M_\odot$) between the total filament mass (∼6200 $M_\odot$) and the sum of the clump masses (∼4300 $M_\odot$) from the *R4* imaging scheme. We take a mean velocity gradient of $\sim\nabla V_{\parallel,\rm obs} = 0.5$ km s^{-1} pc^{-1} to estimate the net mass inflow rate. Assuming $\alpha = 45°$, the inflow rate along the filaments to the central clump is $\sim 1 \times 10^{-3}$ $M_\odot$ yr^{-1}.

4.7. Chemical Properties of Filaments and Dense Clumps

The CO molecular line data from the "TOP" and "SAMPLING" surveys will be used to study the gaseous CO properties (e.g., abundances, CO-to-H_2 conversion factors, CO depletion) of a large sample of PGCCs through joint analysis with the continuum emission data. The KVN survey is designed to observe dozens of dense gas lines toward dense clumps and cores detected in the "SCOPE" survey and characterize their chemical properties. Below, we will investigate the CO depletion of the G26 filament and the dense gas abundances in clump 6.

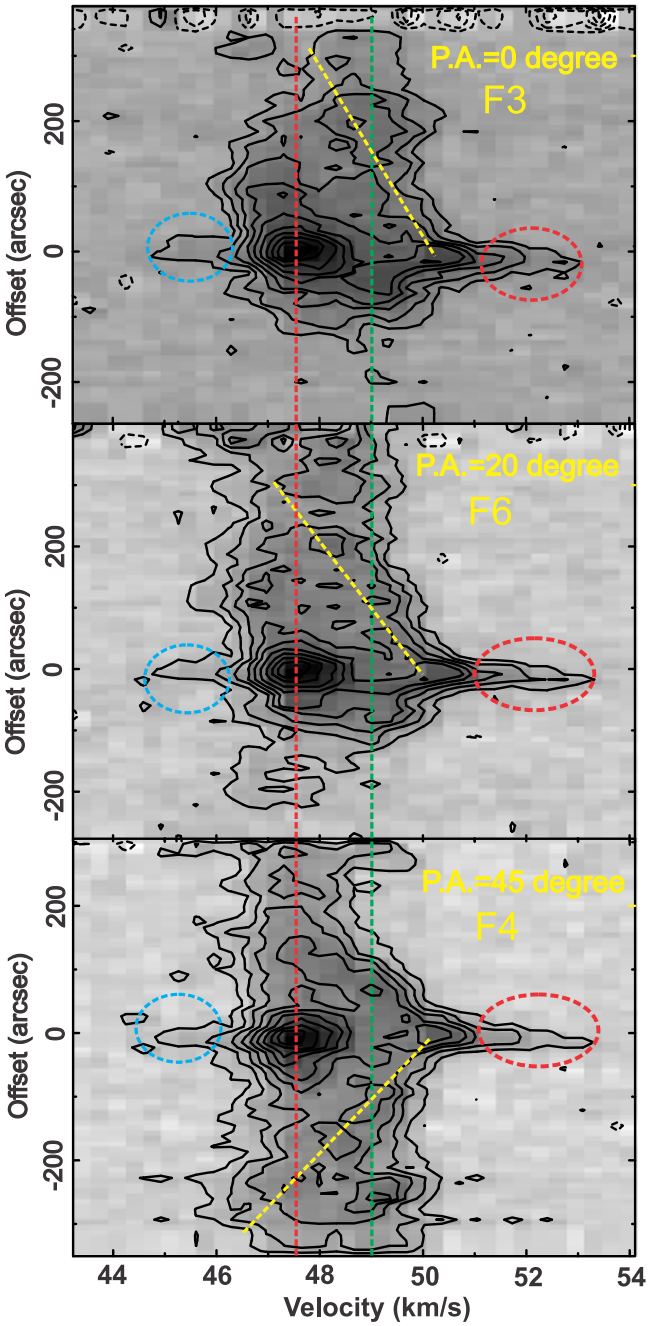

Figure 16. Position–velocity diagrams of ^{13}CO (2–1) line emission. The contour levels are from 10% to 90% in steps of 10% of the peak value (5.3 K). The green dashed vertical line marks the systemic velocity of 49 km s^{-1}. The blueshifted and redshifted high-velocity emission is marked with blue and red dashed ellipses, respectively. The red vertical dashed line depicts the peak emission. The yellow dashed lines show the velocity gradients along the filaments.

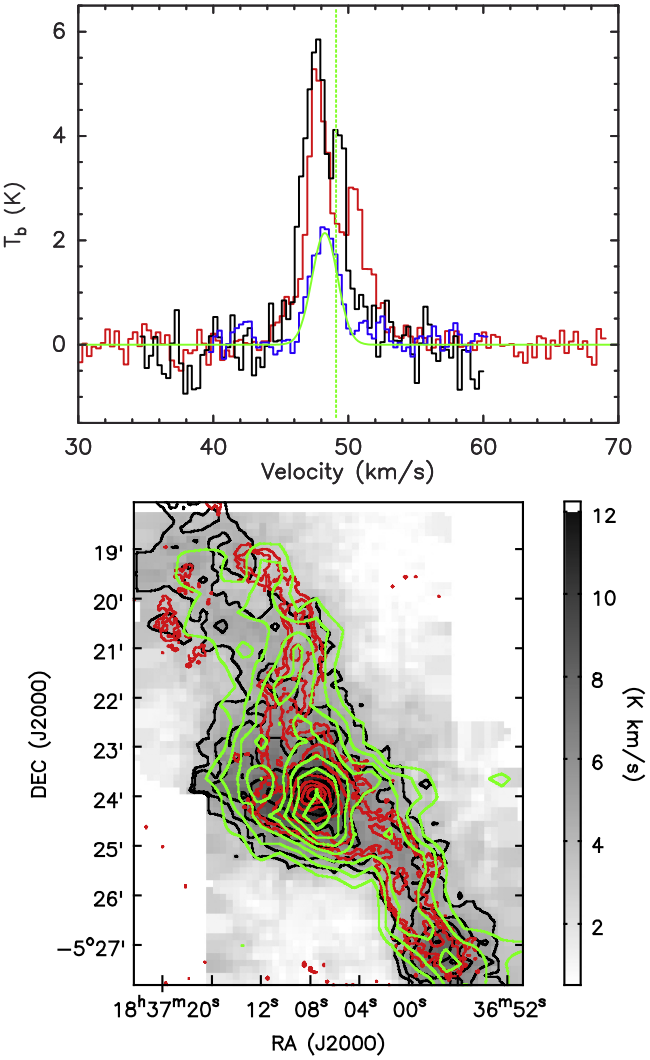

Figure 17. Top panel: spectra of ^{13}CO (1–0) and ^{13}CO (2–1) at the continuum peak, shown in black and red, respectively. The spectrum of C^{18}O (1–0) averaged over an region of $1' \times 1'$ is shown in blue. The Gaussian fit of C^{18}O (1–0) is shown in green. The green dashed vertical line marks the systemic velocity of 49 km s^{-1}. Bottom panel: integrated intensity (47–50 km s^{-1}) map of ^{13}CO (2–1), shown in gray scale and with black contours. The contour levels are from 30% to 90% in steps of 10% of the peak value (12.9 K km s^{-1}). The integrated intensity (47–50 km s^{-1}) map of C^{18}O (1–0) is shown with green contours. The contour levels are from 30% to 90% in steps of 10% of the peak value (6.4 K km s^{-1}). The SCUBA-2 850 μm continuum emission in the *R2* data reduction is shown with red contours. The contour levels are [0.03, 0.05, 0.1, 0.2, 0.4, 0.6, 0.8] × 1.40 Jy beam^{-1}.

4.7.1. CO Depletion

Gaseous CO significantly freezes out onto grain surfaces when densities exceed $\sim 3 \times 10^4$ cm^{-3} (Bacmann et al. 2002). As CO is a major destroyer of molecular ions, CO depletion leads to a change in the relative abundances of major charge carriers (e.g., H_3^+, N_2, H^+, and HCO^+; Bergin & Tafalla 2007; Caselli 2011). In addition, the abundances of the nitrogen hydrides and deuterated molecules are strongly enhanced, and these species are probing the gas where CO (and other carbon-bearing species) is depleted (Bergin & Tafalla 2007; Caselli 2011). Therefore, studies of CO depletion are very important for understanding the chemical processes in star formation. Through statistical studies of a sample of 674 PGCCs, Liu et al. (2013b) found that the CO abundance is strongly (anti)correlated to other physical parameters (e.g., dust temperature, dust emissivity spectral index, column density, volume density, and luminosity-to-mass ratio), suggesting that the gaseous CO abundance can be used as an evolutionary tracer for molecular clouds. Similarly, Giannetti et al. (2014) also found that less evolved ATLASGAL-selected high-mass clumps seem to show larger values for the CO depletion than their more evolved counterparts, and CO depletion increases for denser sources. However, both studies in Liu et al. (2013b)

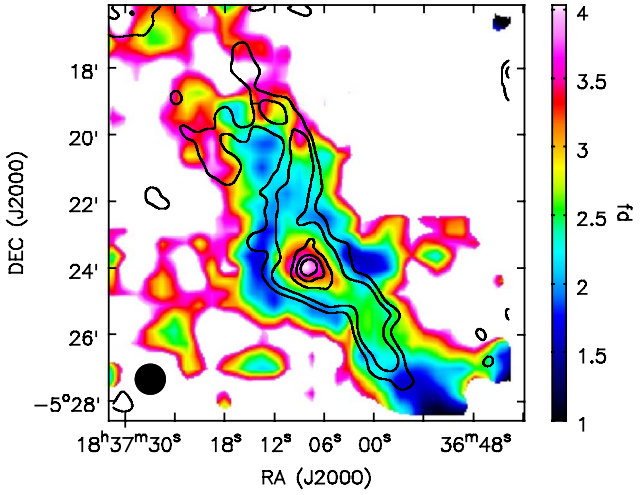

Figure 18. CO gas depletion factor, shown in color scale. The column density map from SED fits with *Herschel* and combined *Planck* and SCUBA-2 850 μm data in *R2* is shown with contours. The contour levels are [0.15, 0.2, 0.4, 0.6, 0.8] × 2.76 × 10^{23} cm^{-2}.

and Giannetti et al. (2014) used single-pointing molecular CO data, which limited the accurate determination of CO depletion in molecular clouds. The molecular CO mapping survey data in the TOP survey are more suitable for investigating how CO abundances or CO depletion varies inside individual molecular clouds and changes in different kinds of molecular clouds.

The top panel of Figure 17 presents the spectra of ^{13}CO (1–0), ^{13}CO (2–1), and C^{18}O (1–0) at the continuum peak for G26. The ^{13}CO (2–1) and C^{18}O (1–0) emissions have a spatial distribution similar to that of the SCUBA-2 850 μm continuum as shown in the bottom panel of Figure 17.

C^{18}O (1–0) emission is optically thin in G26 (see Table 2). We derived C^{18}O column densities following Liu et al. (2013b) by assuming that the excitation temperature of C^{18}O (1–0) is equal to the dust temperature. The C^{18}O abundance ($X_{C^{18}O}$) was derived by comparing the C^{18}O column densities with the H_2 column density map from the SED fits with *Herschel* data and *Planck*+SCUBA-2 data. The C^{18}O column density map and H_2 column density map were smoothed to the same resolution of ∼52″. The CO gas depletion factor (f_D) is defined as $f_D = \frac{\max(X_{C^{18}O})}{X_{C^{18}O}}$, where max($X_{C^{18}O}$) is the maximum C^{18}O abundance (∼1.5 × 10^{-7}) across the map with C^{18}O emission larger than 3σ. The CO gas depletion factor map is presented in Figure 18. The highest depletion (f_D ∼5) occurs at the central massive clump ("6") owing to its largest column density and relatively low temperature. However, since MM6 hosts a relatively strong IR source (bright at 24 and 70 μm), the higher CO depletion means that the star formation process inside MM6 is really new and most of the clump gas is still cold. Due to the large beam of TRAO observations, we see most of the bulk, cold gas rather than the small, localized hot region, further suggesting that the IRDC G26 is still very young.

The CO gas in the surroundings of the central clump MM6 is less depleted (f_D ∼ 1.5–2.5). The outskirts of the filament also show higher apparent CO depletion, which reflects the lower CO abundance therein. The low CO abundance in the outskirts suggests that CO gas is released from dust grains owing to external heating from interstellar radiation and then photodissociated.

4.7.2. Molecular Lines from KVN 21 m Single-pointing Observations

We observed the massive clump "6" in molecular lines that trace dense gas with the KVN 21 m single dishes to characterize its chemical properties. Figure 19 presents the spectra from KVN 21 m single-pointing observations. HCO$^+$ J = 1–0 and H_2CO $2_{1,2} - 1_{1,1}$ lines show "red asymmetry profile" morphology with line wings, indicating that their emission is affected by outflows. H^{13}CO$^+$ J = 1–0 and N_2H^+ J = 1–0 spectra show two velocity components. Since the H^{13}CO$^+$ J = 1–0 and the isolated hyperfine components of N_2H^+ J = 1–0 lines are usually optically thin in IRDCs (Sanhueza et al. 2012), their two velocity components should not be the result of self-absorption. Indeed, the two velocity components may indicate the existence of converging flows inside the clump as resolved in other high-mass clumps (e.g., SDC 335, G10.6–0.4, G33.92+0.11, AFGL 5142; Liu et al. 2013a, 2015, 2016c; Peretto et al. 2013) or interacting subfilaments (e.g., G028.23–00.19; Sanhueza et al. 2013).

We did not detect the 22 GHz water maser but detected the 44 GHz methanol maser. The 44 GHz methanol maser has two velocity components peaked at ∼47.9 and ∼48.7 km s^{-1}, respectively. The 44 GHz methanol maser is blueshifted with respect to the systemic velocity (∼49 km s^{-1}) and has much smaller line widths than other lines that trace denser gas.

SiO emission shows broad lines and two velocity components. The blueshifted component in SiO emission has much broader line widths than the central component, which may be caused by outflow shocks. CCH N = 1–0 and N_2H^+ (1–0) each have hyperfine structures. Their hyperfine lines were fitted assuming LTE to obtain their line widths and optical depths. HCN (1–0) shows a very complicated line profile, which is likely caused by its hyperfine structures and self-absorption. We did not fit the HCN (1–0) spectrum. The other lines were fitted with a Gaussian function. The line parameters are summarized in Table 2. The systemic velocity (∼49 km s^{-1}) is obtained from averaging the peak velocities of the optically thin lines (C^{18}O, HC_3N, and HN^{13}C). The HDCO $2_{0,2} - 1_{0,1}$ line was not detected at an rms level of 0.06 K.

We estimated the column densities from molecular lines with the RADEX[84] radiation transfer code by fixing the kinetic temperature to 17 K, i.e., the dust temperature. For C^{18}O, C_2H, and N_2H^+, the H_2 volume density of clump 6 is set to 6 × 10^3 cm^{-3} from the *R4* imaging scheme. For the other lines (H^{13}CO$^+$, HN^{13}C, and HC_3N), the H_2 volume density of clump 6 is set as 1.8 × 10^4 cm^{-3} from the *R2* imaging scheme since their effective excitation densities are about one order of magnitude higher than that of N_2H^+ (Shirley 2015).

As shown in Figure 20, with three transitions, the source size (θ_S) of the HC_3N-emitting area can be well determined, i.e., 11″. We applied the same filling factor $\left(f = \frac{\theta_S^2}{\theta_S^2 + \theta_{beam}^2}\right)$ for the H^{13}CO$^+$ and HN^{13}C calculations. We assume a filling factor of 1 in the RADEX calculations for the other lines. The RADEX-derived excitation temperature, optical depth, column density, and abundance from each transition are listed in the last four columns of Table 2.

As a major destroyer of N_2H^+, the absence of CO in the gas phase could enhance the abundance of N_2H^+. In warm regions, however, CO evaporation could destroy N_2H^+ and enhance the

[84] RADEX is a one-dimensional non-LTE radiative transfer code that uses the escape probability formulation assuming an isothermal and homogeneous medium without large-scale velocity fields (Van der Tak et al. 2007).

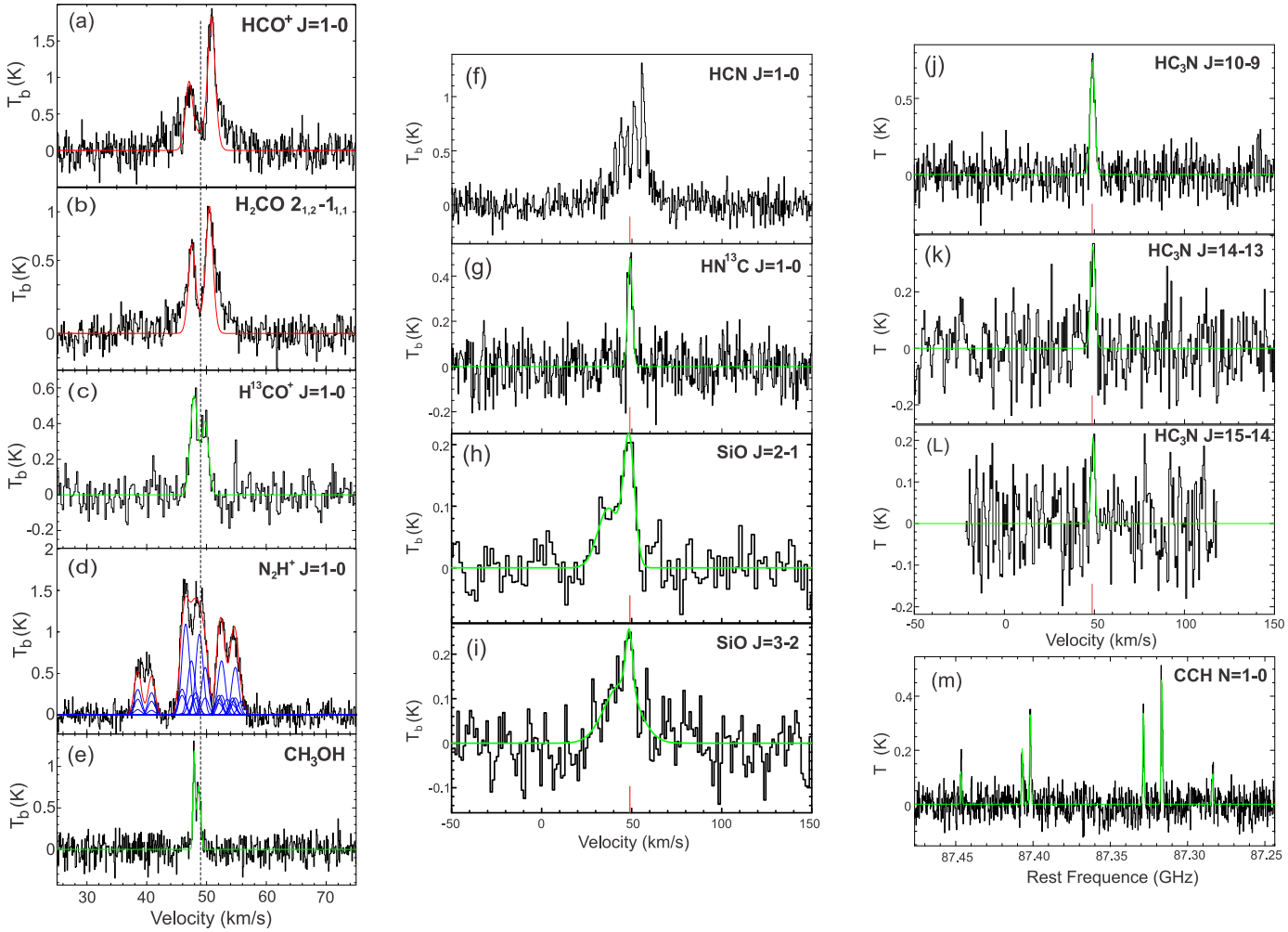

Figure 19. Spectra of the central clump from KVN 21 m single-dish observations. The observed spectra are shown in black. The red lines in panels (a) and (b) show the two-layer model fits. The blue lines in panel (d) show the hyperfine structure fit toward the N_2H^+ (1–0) line spectrum. The red line is the sum of the hyperfine structures. The green line in panel (m) shows the hyperfine structure fit toward the CCH (N = 1–0) line. The green lines in other panels (a) to (l) show the Gaussian fits of the spectra. The line transition name is labeled in the upper right corner of each panel. The black dashed vertical lines in panels (a)–(e) and the red vertical lines in panels (f)–(l) mark the systemic velocity of 49 km s^{-1}.

abundance of HCO^+ by the following reaction (Lee et al. 2004; Busquet et al. 2011):

$$N_2H^+ + CO \rightarrow HCO^+ + N_2. \quad (3)$$

Therefore, a small N_2H^+-to-$H^{13}CO^+$ abundance ratio may indicate that clumps are warm and thus chemically evolved. Feng et al. (2016) recently observed a sample of four 70 μm dark IRDC clumps, whose CO seems to be heavily depleted with depletion factors in the range of 14–50, i.e., about 3–10 times larger than that of G26 clump 6. They also derived high [N_2 H^+]/[$H^{13}CO^+$] abundance ratios (~400–10,000) in the 70 μm dark young IRDC clumps, which are more than two orders of magnitudes larger than that of clump 6 in G26 (~0.8). Therefore, clump 6 in G26 is more chemically evolved than those IRDC clumps. In addition, the abundance of HC_3N, a hot core tracer, is about two orders of magnitude larger in clump 6 than in the 70 μm dark IRDC clumps, indicating that G26 clump 6 may be in a more chemically evolved phase.

4.8. Dynamical Properties of Dense Clumps

The CO molecular line data from the "TOP" and "SAMPLING" mapping surveys can be used to study large-scale kinematics (e.g., collisions, filament accretion, outflows). The HCO^+ $J = 1–0$ and H_2CO $2_{1,2} - 1_{1,1}$ lines in the KVN survey are also good tracers of kinematics like infall and outflows associated with dense clumps/cores. Below, we study the kinematics of G26 based on the ^{13}CO (2–1) line emission from the "SAMPLING" survey and the HCO^+ $J = 1–0$ and H_2CO $2_{1,2} - 1_{1,1}$ lines from KVN observations.

4.8.1. High-velocity Outflows

Outflow wings can be easily identified in the position–velocity diagrams in Figure 16. Figure 21 shows the integrated intensity maps of the outflow emission. Since the blue and red outflow lobes are well separated and have very high flow velocities; neither the very low (pole-on) inclination nor the very high (edge-on) inclination is likely. Therefore, we take 45° as the inclination angle for the outflows with respect to the line of sight. The radii of the blueshifted and redshifted lobes are

Table 3
Parameters of the Two-layer Model

Line	τ_0	Φ	J_c (K)	J_f (K)	J_r (K)	V_{cont} (km s^{-1})	σ (km s^{-1})	V_{out} (km s^{-1})
HCO^+ $J = 1$–0	3.56	0.74	15.70	11.69	19.60	48.98	1.04	0.15
H_2CO $2_{1,2} - 1_{1,1}$	2.21	0.79	15.44	12.03	19.54	49.07	0.93	0.06

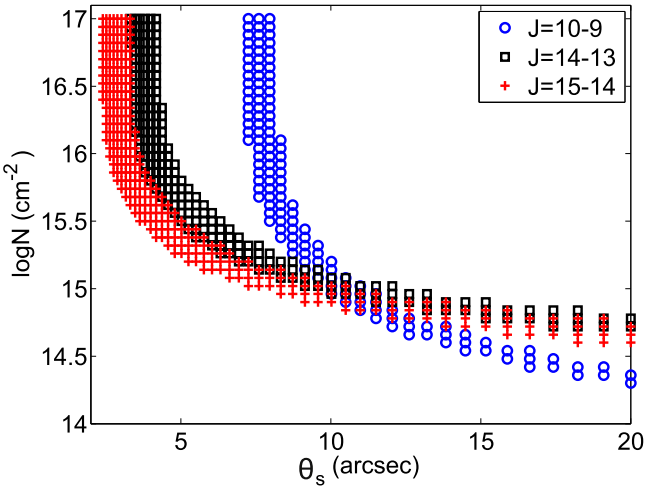

Figure 20. Source size vs. column density in RADEX calculations of HC_3N transitions. The kinetic temperature and H_2 number density in RADEX calculations are fixed to 17 K and 1.8×10^4 cm^{-3}, respectively. The source size and column density of HC_3N in the best fit are 11″ (~0.22 pc) and 9.2×10^{14} cm^{-2}, respectively.

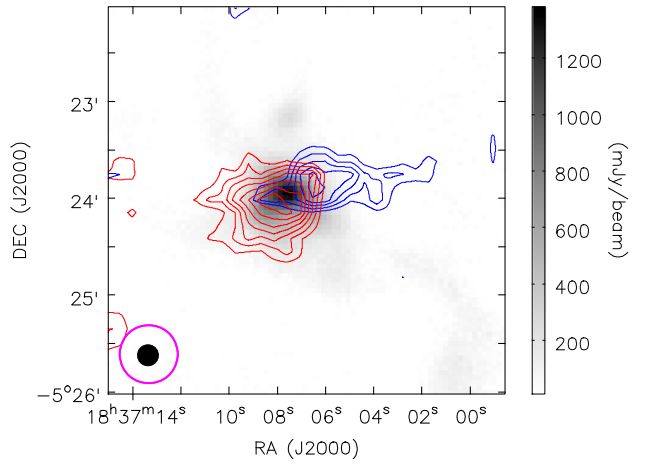

Figure 21. Blueshifted (43–46.5 km s^{-1}) and redshifted (51–55 km s^{-1}) ^{13}CO (2–1) outflow emission in clump 6 are shown in blue and red contours, respectively. The contour levels of blueshifted outflow emission are [0.5, 0.6, 0.7, 0.8, 0.9] × 3.06 K km s^{-1}. The contour levels of redshifted outflow emission are [0.3, 0.4, 0.5, 0.6, 0.7, 0.8, 0.9] × 5.65 K km s^{-1}. The SCUBA-2 850 μm continuum emission is shown in gray scale.

~1.6 and ~1.1 pc, respectively. The characteristic outflow velocities of the blueshifted and redshifted lobes are ~5.1 and ~3.3 km s^{-1}, respectively. Assuming that the excitation temperature of ^{13}CO (2–1) line wing emission is 17 K, i.e., the dust temperature, the integrated intensity can be converted to the outflow masses following Garden et al. (1991). The ^{13}CO abundance (7×10^{-7}) is converted from $C^{18}O$ abundance (1×10^{-7}) with a [$^{13}CO/C^{18}O$] abundance ratio (~7) derived from empirical relations between molecular abundances and the galactocentric distance (Wilson & Rood 1994; Giannetti et al. 2014). The masses of the blueshifted and redshifted lobes are ~67 and ~97 $M_\odot$, respectively. The momentum of the blueshifted and redshifted lobes is ~342 and ~314 $M_\odot$ km s^{-1}, respectively. The energies of the blueshifted and redshifted lobes are ~1.7×10^{46} and ~1.1×10^{46} erg, respectively. The dynamical timescales $\left(t_{dyn} = \frac{2R}{V_{flow}}\right)$ of the blueshifted and redshifted lobes are 6.2×10^5 yr and 6.8×10^5 yr, respectively. The total outflow mass-loss rate is ~2.5×10^{-4} $M_\odot$ yr^{-1}.

4.8.2. Outflow-driven Expansion

The HCO^+ $J = 1$–0 and H_2CO $2_{1,2} - 1_{1,1}$ lines show "red asymmetric profiles" morphologies, suggesting expansion. We apply a simple "two-layer model" to fit the lines. The model is described in Appendix B. The results are presented in Table 3. The expansion velocities inferred from the HCO^+ $J = 1$–0 and H_2CO $2_{1,2} - 1_{1,1}$ lines are ~0.15 and ~0.06 km s^{-1}, respectively. Assuming that the whole clump (with $M \sim 2100$ $M_\odot$) is expanding with a velocity of 0.1 km s^{-1}, the total momentum and energy of the expanding clump are 210 $M_\odot$ km s^{-1} and ~2.1×10^{44} erg, respectively. Since it is unlikely that the whole clump is in expansion, these momentum and energy values should be treated as upper limits. Even in this extreme case, however, both the momentum and energy are smaller than those of the low-velocity outflows, indicating that the outflows have enough energy themselves to drive the envelope expansion.

The virial mass of the clump MM6 considering turbulent support can be derived as $\frac{M_{vir}}{M_\odot} = 210\left(\frac{R}{pc}\right)\left(\frac{\Delta V}{km\ s^{-1}}\right)^2$ (MacLaren et al. 1988; Zhang et al. 2015), where R is the radius (1.15 pc) and ΔV is the line width (2.22 km s^{-1}) of $C^{18}O$ (1–0). The virial mass is ~1200 $M_\odot$, which is much smaller than the clump mass (~2100 M_{Sun}), indicating that the whole clump may still be in collapse. Therefore, the expansion revealed by HCO^+ $J = 1$–0 and H_2CO $2_{1,2} - 1_{1,1}$ lines should be very localized.

Figure 22 shows a cartoon to describe the PGCC G26 based on the results from the present data. Our findings of G26 are as follows: (i) the G26 filament may be formed as a result of large-scale compression flows evidenced by the temperature and velocity gradients across its natal cloud, (ii) subfilaments in G26 have different velocities and may interact with each other, (iii) the central massive clump where massive stars are forming may still accrete gas along subfilaments, and (iv) the entire massive clump may still be in global collapse while its inner part seems to be undergoing expansion due to outflow feedback.

5. Summary

We introduce here the survey strategy, observations, data reduction, and example science for a joint survey program "TOP-SCOPE," targeting 1000–2000 PGCCs at TRAO 14 m and

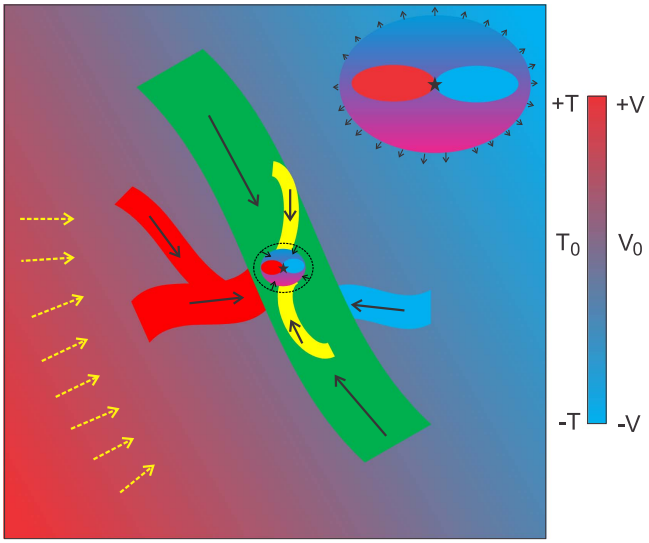

Figure 22. Cartoon showing the environment of PGCC G26.53+0.17. The main gas filament is shown in green. The SCUBA-2 filament is shown in yellow. Other small subfilaments are shown in red, green, and blue. PGCC G26.53+0.17 is located in a parent cloud with velocity and temperature gradients along the east–west direction. The central clump MM6 (dashed ellipse) may still be in collapse, while its inner part (color filled ellipse) is undergoing expansion due to outflow feedback from the protostars. The zoomed-in picture of the central clump is shown in the upper right corner. The red and blue ellipses represent the outflow lobes. The arrows show the directions of gas flows.

JCMT 15 m telescopes. "TOP," standing for "TRAO Observations of Planck cold clumps," is a ^{12}CO/^{13}CO $J = 1$–0 line survey of 2000 PGCCs with the Taeduk Radio Astronomy Observatory 14 m telescope. "SCOPE," standing for "SCUBA-2 Continuum Observations of Pre-protostellar Evolution," is a legacy survey using SCUBA-2 on the James Clerk Maxwell Telescope (JCMT) at the East Asian Observatory (EAO) to survey 1000 PGCCs at 850 μm continuum. Follow-up observations toward SCUBA-2-detected dense clumps/cores with other ground-based telescopes (NRO 45 m, SMT, KVN, SMA, ALMA) are ongoing.

We introduced the example science of the "TOP-SCOPE" survey and other joint survey programs with an exemplar source, PGCC G26.53+0.17 (i.e., G26). The main findings for G26 are as follows:

(1) The total mass, the length, and the mean line mass (M/L) of the G26 filament revealed are ~6200 $M_\odot$, ~12, and ~500 $M_\odot$ pc^{-1}, respectively. Both the length and line mass of G26 are comparable to those of the integral-shaped filament in the Orion A cloud (Kainulainen et al. 2017).

(2) Ten clumps are found along the filament with a mean separation of ~1.3 pc. Only two of them (MM6, MM10) are associated with protostars. The others seem to be starless. The clumps in G26, especially the dense and massive ones, are very likely bounded by gravity and have the ability to form high-mass stars. The typical spacing and mass of clumps in G26 are comparable to the predictions in gravitational fragmentation of an isothermal, nonmagnetized, and turbulent supported cylinder, suggesting that the fragmentation in G26 from cloud (at ~10 pc scale) to clump (at ~1 pc scale) is very likely dominated by turbulence.

(3) Evidence for grain growth along the filament is found. The histograms of dust emissivity spectral index β can be well fitted with two normal distributions regardless of whether or not 850 μm data were included in the SED fits. Such a bimodal behavior in β distribution suggests grain growth along the filament.

(4) The N-PDF and two-point correlation functions (2PT) of the natal cloud harboring the G26 filament are investigated. The slope (−3.9) of the power-law tail is comparable to those of IRDCs G28.34+0.06 (−3.9) and G14.225–0.506 (−4.1). The 2PT function shows a smooth decay of correlation strengths over all spatial scales up to ~15 pc. The flat 2PT correlation indicates that the column density distribution of G26 is very homogeneous over all spatial scales and the mass is less concentrated overall than in high-mass protoclusters.

(5) From comparing the SCUBA-2 images with *Planck* +SCUBA-2 combined images, we found that only 30%–40% of the cloud gas in G26 is dense gas.

(6) The G26 filament may be formed owing to large-scale compression flows evidenced by the temperature and velocity gradients across its natal cloud. Subfilaments in G26 have different velocities and may interact with each other. The central massive clump where massive stars are forming may still accrete gas along subfilaments with a natal mass inflow rate of ~1×10^{-3} $M_\odot$ yr^{-1}.

(7) The mass of the most massive clump MM6 is much larger than its virial mass, suggesting that it may still be in global collapse. Its inner part traced by HCO^+ $J = 1$–0 and H_2CO $2_{1,2} - 1_{1,1}$ lines, however, seems to be undergoing expansion due to outflow feedback. The total mass and total outflow mass-loss rate of the outflows are ~164 $M_\odot$ and ~2.5×10^{-4} $M_\odot$ yr^{-1}, respectively.

(8) The most massive clump, MM6, has a much smaller CO gas depletion factor, much smaller $[N_2H^+]/[H^{13}CO^+]$ abundance ratio, and much larger HC_3N abundance than 70 μm dark young IRDC clumps, indicating that clump 6 is more chemically evolved and may be in a more chemically evolved phase.

All the example science discussed for G26 will be fully explored through more statistical studies with the "TOP-SCOPE" data and other follow-up survey data toward larger samples.

Tie Liu is supported by the KASI fellowship and EACOA fellowship. Ke Wang is supported by grant WA3628-1/1 of the German Research Foundation (DFG) through the priority program 1573 ("Physics of the Interstellar Medium"). S.-.L.Q. is supported by the Joint Research Fund in Astronomy (U1631237) under cooperative agreement between the National Natural Science Foundation of China (NSFC) and Chinese Academy of Sciences (CAS), by the Top Talents Program of Yunnan Province (2015HA030). M.J. and V.-M.P. acknowledge the support of the Academy of Finland grant no. 285769. J.Ma. acknowledges the support of ERC-2015-STG No. 679852 RADFEEDBACK. C.W. L. was supported by the Basic Science Research Program though the National Research Foundation of Korea (NRF) funded by the Ministry of Education, Science, and Technology (NRF-2016R1A2B4012593). Miju Kang was supported by the Basic Science Research Program through the National Research Foundation of Korea (NRF) funded by the Ministry of Science, ICT, and Future Planning (no. NRF-2015R1C1A1A01052160). The James Clerk Maxwell Telescope is operated by the East Asian Observatory on behalf of the National Astronomical Observatory of Japan, Academia Sinica Institute of Astronomy and Astrophysics, the Korea Astronomy and Space Science Institute, the National Astronomical Observatories of China, and the Chinese Academy of Sciences (grant no. XDB09000000), with additional funding support from the Science and Technology Facilities

Council of the United Kingdom and participating universities in the United Kingdom and Canada. The data presented in this paper are based on the ESO-ARO program ID 196.C-0999(A). D.M., G.G., and L.B. acknowledge support from CONICYT Project PFB-06. S.P.L. acknowledges support from the Ministry of Science and Technology of Taiwan with grants MOST 105-2119-M-007-024 and MOST 106-2119-M-007-021-MY3. J.E.L. was supported by the Basic Science Research Program through the National Research Foundation of Korea (grant No. NRF-2015R1A2A2A01004769) and the Korea Astronomy and Space Science Institute under the R&D program supervised by the Ministry of Science, ICT and Future Planning. V.-M.P. acknowledges the financial support from the European Research Council, Advanced grant No. 320773 SAEMPL. D.L. is part of the CAS Interdisciplinary Innovation Team team.

Software: Starlink software (Chapin et al. 2013; Jenness et al. 2013; Currie et al. 2014), GILDAS (http://www.iram.fr/IRAMFR/GILDAS/), RADEX (Van der Tak et al. 2007), MIRIAD (https://www.cfa.harvard.edu/sma/miriad/) and CASA (https://casa.nrao.edu/).

Appendix A
Observations and Data Reduction for PGCC G26.53+0.17

The JCMT/SCUBA-2, TRAO 14 m, SMT 10 m, and KVN 21 m observations of PGCC G26.53+0.17 are summarized in Table 4.

A.1. Herschel Archival Data

G26 was mapped with *Herschel* as part of the Hi-GAL project (Molinari et al. 2010). The observations include 70,

Table 4
Observations of PGCC G26.53+0.17

JCMT/SCUBA-2 850 μm Continuum Observations							
Date	Mode	τ_{225}		$\theta_B(")$	FCF	rms (mJy beam^{-1})	Tracer
2016 Apr 21	CV Daisy	0.057		14.1	543.3	8.3	dense clumps/filaments
2017 May 13	Pong1800	0.090		14.1	513.2	18.7	dense clumps/filaments
2017 May 14	Pong1800	0.115		14.1	556.7	17.5	dense clumps/filaments
2017 May 16	Pong1800	0.071		14.1	547.0	25.7	dense clumps/filaments
2017 May 23	Pong1800	0.122		14.1	561.6	30.7	dense clumps/filaments
2017 May	Pong1800	⋯		14.1		10.7	dense clumps/filaments
TRAO 14 m OTF Observations on 2017 Jan 09[a]							
Line	Frequency (GHz)	T_{sys} (K)	Δv (km s^{-1})	$\theta_B(")$	B_{eff}	rms (K)	Tracer
^{12}CO (1–0)	115.27120	551	0.32	45	0.51	1.1	large-scale structure and kinematics
^{13}CO (1–0)	110.20135	244	0.33	47	0.54	0.4	large-scale structure and kinematics
C^{18}O (1–0)	109.78217	233	0.33	47	0.54	0.2	dense clumps/filament
SMT 10 m OTF Observations[a]							
Line	Frequency (GHz)	T_{sys} (K)	Δv (km s^{-1})	$\theta_B(")$	B_{eff}	rms (K)	Tracer
^{13}CO (2–1)	220.39868	250	0.34	36	0.70	0.2	large-scale structure and kinematics
KVN 21 m Single-pointing Observations on 2017 May 27[a]							
Line	Frequency (GHz)	T_{sys} (K)	Δv (km s^{-1})	$\theta_B(")$	B_{eff}	rms (K)	Tracer
H_2O $6_{1,6} - 5_{2,3}$[b]	22.23508	110	0.42	126	0.46	0.08	maser and shock tracer
CH_3OH $7_0 - 6_1A+$	44.06941	117	0.11	63	0.48	0.12	maser and shock tracer
HCN $J = 1$–0	88.63185	287	0.42	32	0.41	0.09	outflow and infall
HCO$^+$ $J = 1$–0	89.18852	203	0.21	32	0.41	0.10	outflow and infall
H^{13}CO$^+$ $J = 1$–0	86.75429	200	0.22	32	0.41	0.08	dense gas, V_{lsr} and σ
HC_3N $J = 10$–9	90.97902	308	0.41	32	0.41	0.10	hot core
HC_3N $J = 14$–13	127.36767	496	0.59	23	0.39	0.09	hot core
HC_3N $J = 15$–14	136.46441	437	0.55	23	0.39	0.07	hot core
SiO $J = 2$–1	86.84696	240	1.73	32	0.41	0.03	shock tracer
SiO $J = 3$–2	130.26861	345	1.15	23	0.39	0.04	shock tracer
HN^{13}C $J = 1$–0	87.09085	240	0.86	32	0.41	0.05	dense gas, V_{lsr} and σ
CCH $N = 1$–0	87.31692	206	0.43	32	0.41	0.07	photodissociation tracer
N_2H^+ $J = 1$–0	93.17340	236	0.10	32	0.41	0.09	dense gas, V_{lsr} and σ
H_2CO $2_{1,2} - 1_{1,1}$	140.83950	282	0.13	23	0.39	0.09	outflow and infall
HDCO $2_{0,2} - 1_{0,1}$[b]	128.81286	477	1.15	23	0.39	0.06	deuterium fraction

Notes.
[a] For molecular line observations, the columns are line name, line frequency, system temperature, velocity resolution, beam size, main-beam efficiency, rms level in brightness temperature, and tracers. The spectra are usually slightly smoothed to get a better S/N level. The velocity resolutions are thus different from original ones. The rms levels were estimated from smoothed spectra.
[b] These lines were not detected toward PGCC G26.53+0.17.

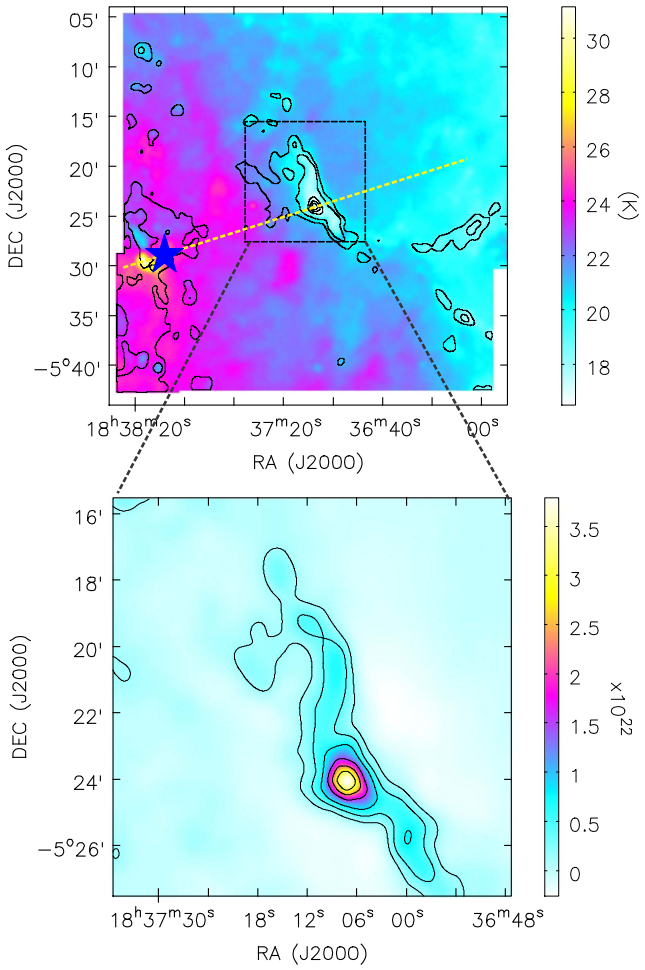

Figure 23. Top panel: from *Herschel* data, column density contours overlaid on a dust temperature color image. The contour levels are [0.15, 0.2, 0.4, 0.6, 0.8] × 4.8 × 10^{22} cm^{-2}. The blue star marks the position of the infrared bubble shown in Figure 12. The yellow dashed line marks the direction along which the cuts in Figure 13 were made. Bottom panel: close-up of column density map from *Herschel* data over the SCUBA-2 mapped region. The large-scale emission in *Herschel* bands was filtered out. The contour levels are [0.03, 0.1, 0.2, 0.4, 0.6, 0.8]×3.8 × 10^{22} cm^{-2}.

160, 250, 350, and 500 μm bands that were observed in parallel mode with 60″ s^{-1} scanning speed. We use the level 2.5 maps available in the *Herschel* Science Archive,[85] *SPIRE* data (250–500 μm) using extended source calibration, and the PACS maps (70, 160 μm) made with the UNIMAP method (Piazzo et al. 2015). The resolutions of the original maps are approximately 12″, 15″, 18.″3, 24.″9, and 36.″3, respectively. Given the fast scanning speed, the effective PACS beams are elongated.

Figure 23 presents the dust temperature and column density maps of PGCC G26.53+0.17 derived from *Herschel*/SPIRE data. The column density maps in Figure 23 are used as external masks in the below JCMT/SCUBA-2 data reduction. We fit the SEDs pixel by pixel with a modified blackbody function using the three *Herschel*/SPIRE bands. The modified blackbody function is

$$F(\nu) = F(\nu_0)\frac{B(\nu, T)}{B(\nu_0, T)}\left(\frac{\nu}{\nu_0}\right)^{\beta} = \kappa(\nu)B(T)M/d^2, \qquad (4)$$

where $F(\nu)$ is the flux density at frequency ν, ν_0 is a selected reference frequency, B stands for the *Planck* law, β is the opacity spectra index, M is the clump mass, and d is the cloud distance. The *Herschel* data were fitted with modified blackbody spectra with $\beta = 1.8$ to estimate color correction factors and to derive estimates of the dust optical depth at a common spatial resolution of 40″. The values were also converted to estimates of hydrogen column density assuming a dust opacity of $\kappa = 0.1(\nu/1000\ \mathrm{GHz})^{\beta}$ cm^2 g^{-1} (Beckwith et al. 1990).

The top panel of Figure 23 presents the dust temperature and column density maps derived from *Herschel*/SPIRE data without applying any local spatial filtering. A temperature gradient along the SE–NW direction is seen in the dust temperature map. The bottom panel in Figure 23 presents the column density map of the G26 filament derived from *Herschel*/SPIRE data with the extended emission larger than 300″ filtered out. The last closed contours in the column density maps outline the external masks used in the JCMT/SCUBA-2 data reduction in Section 6.2.

A.2. JCMT/SCUBA-2 Data Reduction

The CV Daisy observations of G26 were conducted on 2016 April 21. To test how well CV Daisy observations can recover faint and extended emission, we also conducted Pong1800 maps from 2017 May 13 to 23 for comparison. In contrast to the CV Daisy observations, the Pong1800 maps, which are designed for mapping larger fields, cover a circular area of ∼30′ diameter with a uniform sensitivity and thus better recover extended emission.

The JCMT data reduction methods are similar to those used in the JCMT Gould Belt survey and JCMT transient survey (Ward-Thompson et al. 2007; Mairs et al. 2015, 2017; Herczeg et al., submitted). The data reduction procedure was performed using the iterative mapmaking technique makemap (Chapin et al. 2013) in the SMURF package of the Starlink software (Jenness et al. 2013; Currie et al. 2014). The user can also supply an external mask that surrounds the astronomical signal to constrain the solution derived by makemap, which, together with a larger spatial filter, can better recover faint and extended structure. Generally, the largest recoverable scales are ∼600″ before atmospheric signal becomes significant. The details of JCMT data reduction can be found in Mairs et al. (2015, 2017). In this paper, we performed four individual data reductions labeled *R1, R2*, *R3*, and *R4* with different external masks and spatial filters for comparison. The parameters of makemap used in the data reductions are the same as in Mairs et al. (2015).

(1) *R1:* We first run makemap with an effective spatial filter of 200″ and no external mask. Then an external mask was constructed from the final map with S/N > 3. The external mask was used to constrain the solution derived by makemap in a second run. Therefore, the structure was filtered to 200″ in the *R1* data reduction. This data reduction is efficient to detect dense clumps and is used in the first data release of the "SCOPE" project. The top panel of Figure 24 shows the SCUBA-2 850 μm continuum emission in the *R1* data reduction.

(2) *R2:* An external mask from the *Herschel* data (the last closed contour in the bottom panel of Figure 23) was applied in the data reduction. The external mask corresponds to the contour of 3% of the peak column density value, which is the largest astronomical structure (see the blue contour in the bottom panel of Figure 24) that could be recovered in the CV

[85] http://archives.esac.esa.int/hsa

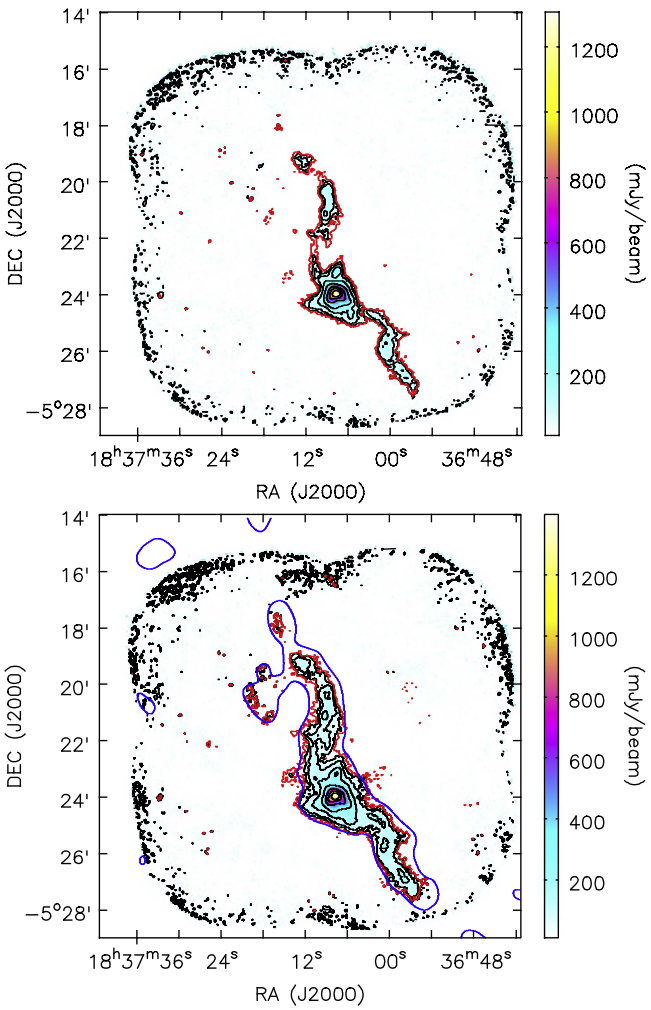

Figure 24. Top panel: SCUBA-2 850 μm continuum emission in the *R1* data reduction for G26. The contour levels are [0.03, 0.05, 0.1, 0.2, 0.4, 0.6, 0.8] × 1.35 Jy beam^{-1}. Bottom panel: SCUBA-2 850 μm continuum emission in the *R2* data reduction. The contour levels are [0.03, 0.05, 0.1, 0.2, 0.4, 0.6, 0.8] × 1.40 Jy beam^{-1}. The red contour in both panels shows the S/N level of 3.

Daisy map. Besides the external mask, an effective spatial filter of 300″ was applied in the data reduction with makemap. The bottom panel of Figure 24 shows the SCUBA-2 850 μm continuum emission in the *R2* data reduction. Compared with *R1*, *R2* better reveals not only dense clumps but also extended structures between them. The peak flux density (1.40 Jy beam^{-1}) in *R2* is slightly larger than the value (1.35 Jy beam^{-1}) in *R1*.

(3) *R3:* Same as *R1*, but with a larger effective spatial filter of 600″. Figure 25(a) shows the SCUBA-2 850 μm continuum emission in the *R3* data reduction. In contrast to *R1* and *R2*, *R3* recovers more extended emission.

(4) *R4:* Same as *R2*, but with a larger effective spatial filter of 600″. The external mask was constructed from the *Herschel* data without any spatial filtering (the last closed contour in the top panel of Figure 23). The external mask corresponds to the contour of 15% of the peak column density value, which is the largest astronomical structure (see the blue contour in Figure 25(b)) that could be recovered in the CV Daisy map. Figure 25(b) shows the SCUBA-2 850 μm continuum emission in the *R4* data reduction. Only the central coherent structure in the masked region is reliable. In general, *R4* and *R3* reveal

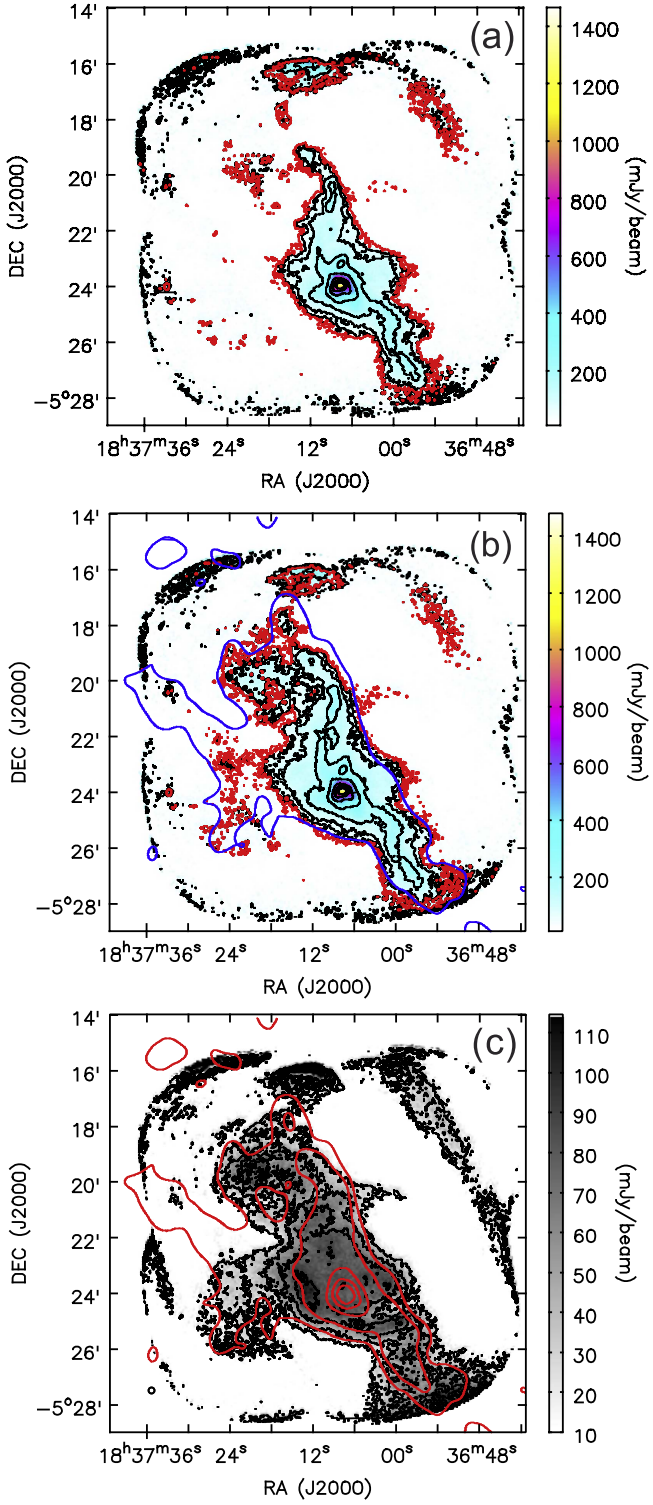

Figure 25. (a) SCUBA-2 850 μm continuum emission in the *R3* data reduction, shown in color scale and black contours. The contour levels are [0.03, 0.05, 0.1, 0.2, 0.4, 0.6, 0.8] × 1.47 Jy beam^{-1}. The red contour shows the S/N level of 3. (b) SCUBA-2 850 μm continuum emission in the *R4* data reduction, shown in color scale and black contours. The contour levels are [0.03, 0.05, 0.1, 0.2, 0.4, 0.6, 0.8] × 1.48 Jy beam^{-1}. The red contour shows the S/N level of 3. The blue contour outlines the external mask from the *Herschel* column density map. (c) Extended SCUBA-2 850 μm continuum emission (*R4–R2*), shown in gray scale and black contours. The contour levels are [0.2, 0.4, 0.6, 0.8] × 0.11 Jy beam^{-1}. The red contours show the column density derived from *Herschel*/SPIRE data. The contour levels are [0.15, 0.2, 0.4, 0.6, 0.8] × 4.8 × 10^{22} cm^{-2}.

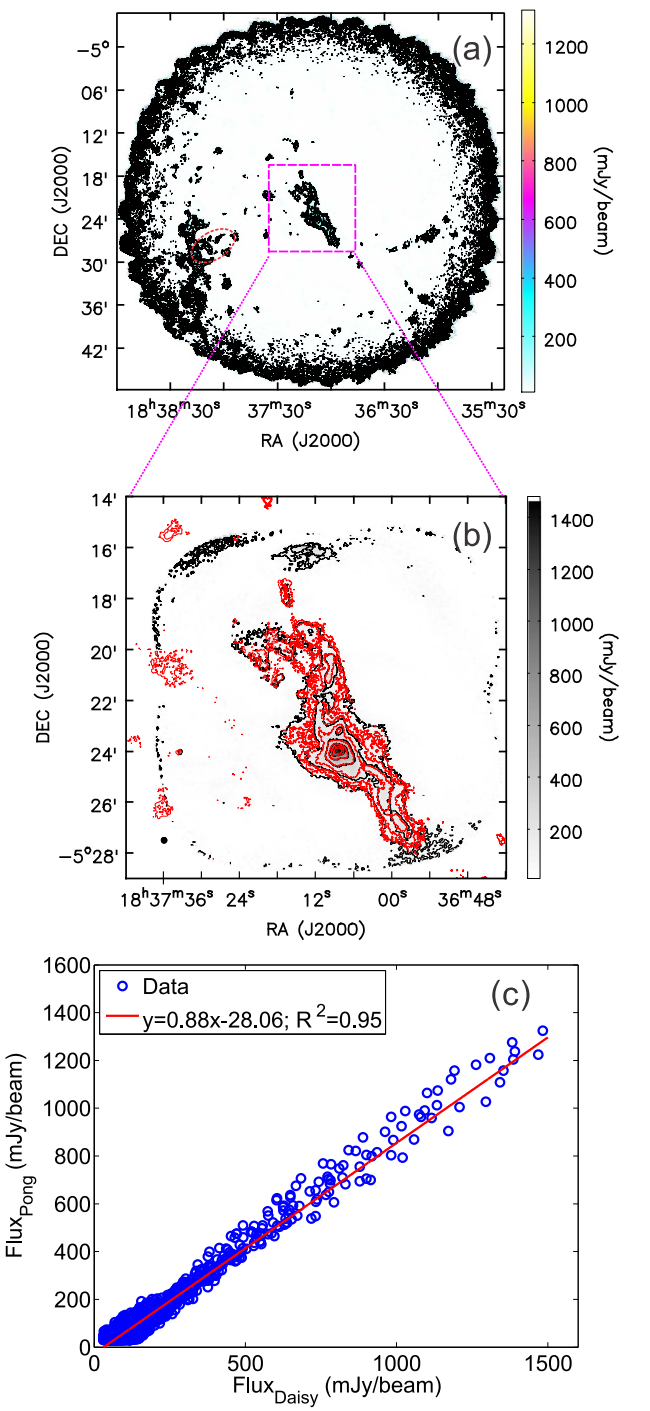

Figure 26. (a) Pong1800 SCUBA-2 850 μm map. The contours are [0.03, 0.05, 0.1, 0.2, 0.4, 0.6, 0.8] × 1.32 Jy beam^{-1}. The red dashed ellipse marks the position of the infrared bubble shown in Figure 12. (b) Close-up of the Pong1800 SCUBA-2 850 μm map in the Daisy map region, shown with red contours. The grayscale image and black contours show the CV Daisy map. The contour levels are [0.05, 0.1, 0.2, 0.4, 0.6, 0.8] × 1.48 Jy beam^{-1}. (c) Comparison of flux in the Daisy map with flux in the Pong map for pixels with S/N > 3. The red line shows the linear fit.

similar structure. With the external mask from *Herschel*, makemap, however, recovers more extended and faint structures in *R4* than in *R3*. Figure 25(c) reveals the extended emission in the difference image between *R4* and *R2*. *R4* recovers a more flattened structure with extended emission (∼50 mJy beam^{-1}) than *R2*.

In general, maps with external masks recover more flux. Therefore, we suggest to apply external masks in SCUBA-2 data reduction if *Herschel* data are available. Although *R1* was used in the first data release of the SCOPE survey, *R1* cannot recover the flux of the dense clumps as well as the other data reductions (*R2*, *R3*, and *R4*). *R3* can recover most flux but detect the least number of dense clumps. Therefore, in this paper (except in Section 4.2), we mainly use the data reductions *R2* and *R4* in the further analysis. *R2* is very efficient to reveal dense structures (e.g., dense clumps and filaments). In contrast, *R4* recovers more extended structures surrounding the dense clumps.

A.3. Comparing Daisy Map with Pong1800 Map

To verify the detection of faint and extended structure in CV Daisy maps, we compare the Daisy and Pong1800 maps, both of which are obtained with the *R4* imaging scheme. Figure 26(a) shows the Pong1800 map. In Figure 26(b), we compare Daisy and Pong1800 maps. In general, the Daisy map and the Pong1800 map show very consistent morphology, indicating that the Daisy map can recover large-scale structures as well as the Pong map. The flux recovered in the Daisy map is also linearly correlated with the flux in the Pong map as shown in Figure 26(c): $\mathrm{Flux_{Pong}} = (0.883 \pm 0.003)\mathrm{Flux_{Daisy}} - (28.062 \pm 0.532)$; $R^2 = 0.95$. The Pong1800 map will be discussed in detail in another paper.

Appendix B
"Two-layer" Models for Fitting HCO^+ $J = 1$–0 and H_2CO $2_{1,2}$−$1_{1,1}$ Lines

To investigate the properties of the expanding gas, the profiles of the HCO^+ $J = 1$–0 and H_2CO $2_{1,2} - 1_{1,1}$ lines were modeled with an enhanced version of the "two-layer" model, which is similar to the infall models used in Myers et al. (1996) and Di Francesco et al. (2001). In this model, a continuum source is located in between the two layers. Each layer has peak optical depth τ_0, velocity dispersion σ, and expanding speed $V_{\rm exp}$ with respect to the continuum source. The gas is moving away from the continuum source if $V_{\rm out}$ is positive. The line brightness temperature at velocity V is

$$\Delta T_{\rm B} = (J_f - J_{cr})[1 - \exp(-\tau_f)] + (1 - \Phi)(J_r - J_b) \times [1 - \exp(-\tau_r - \tau_f)],$$

where

$$J_{cr} = \Phi J_c + (1 - \Phi) J_r$$

and

$$\tau_f = \tau_0 \exp\left[\frac{-(V + V_{\rm out} - V_{\rm cont})^2}{2\sigma^2}\right]$$

$$\tau_r = \tau_0 \exp\left[\frac{-(V - V_{\rm out} - V_{\rm cont})^2}{2\sigma^2}\right].$$

J_c, J_f, J_r, J_b are the *Planck* temperatures of the continuum source, the "front" layer, the "rear" layer, and the cosmic background radiation, respectively. $J = \frac{h\nu}{k}\frac{1}{\exp(T_0/T) - 1}$ is related to the blackbody temperature T at frequency ν, where h is Planck's constant and k is Boltzmann's constant. Φ and $V_{\rm cont}$ are the filling factors and the systemic velocities of the continuum sources, respectively.

ORCID iDs

Tie Liu https://orcid.org/0000-0002-5286-2564
Kee-Tae Kim https://orcid.org/0000-0003-2412-7092
Ke Wang https://orcid.org/0000-0002-7237-3856
Ken'ichi Tatematsu https://orcid.org/0000-0002-8149-8546
Sheng-Yuan Liu https://orcid.org/0000-0003-4603-7119
Yuefang Wu https://orcid.org/0000-0002-5076-7520
Gary Fuller https://orcid.org/0000-0001-8509-1818
Di Li https://orcid.org/0000-0003-3010-7661
Sung-ju Kang https://orcid.org/0000-0002-5004-7216
Yuxin Lin https://orcid.org/0000-0001-9299-5479
D. Johnstone https://orcid.org/0000-0002-6773-459X
J. H. He https://orcid.org/0000-0002-3938-4393
P. M. Koch https://orcid.org/0000-0003-2777-5861
Patricio Sanhueza https://orcid.org/0000-0002-7125-7685
Sheng-Li Qin https://orcid.org/0000-0003-2302-0613
Q. Zhang https://orcid.org/0000-0003-2384-6589
Paul F. Goldsmith https://orcid.org/0000-0002-6622-8396
Neal J. Evans II https://orcid.org/0000-0001-5175-1777
Glenn J. White https://orcid.org/0000-0002-7126-691X
L. V. Toth https://orcid.org/0000-0002-5310-4212
Steve Mairs https://orcid.org/0000-0002-6956-0730
Mengyao Tang https://orcid.org/0000-0001-9160-2944
Archana Soam https://orcid.org/0000-0002-6386-2906
Harriet Parsons https://orcid.org/0000-0002-6327-3423
Jinghua Yuan https://orcid.org/0000-0001-8060-3538
Chuan-Peng Zhang https://orcid.org/0000-0002-4428-3183
Jan Wouterloot https://orcid.org/0000-0002-4694-6905
Lei Qian https://orcid.org/0000-0003-0597-0957
Siyi Feng https://orcid.org/0000-0002-4707-8409
Yuri Aikawa https://orcid.org/0000-0003-3283-6884
Graham Bell https://orcid.org/0000-0003-0438-8228
Andrew Blain https://orcid.org/0000-0001-7489-5167
L. Bronfman https://orcid.org/0000-0002-9574-8454
D.-Y. Byun https://orcid.org/0000-0003-1157-4109
Huei-Ru Chen https://orcid.org/0000-0002-9774-1846
A. Chrysostomou https://orcid.org/0000-0002-9583-8644
Jane Greaves https://orcid.org/0000-0002-3133-413X
J. Hatchell https://orcid.org/0000-0002-4870-2760
T. Hirota https://orcid.org/0000-0003-1659-095X
Izaskun Jimenez-Serra https://orcid.org/0000-0003-4493-8714
Miju Kang https://orcid.org/0000-0002-5016-050X
Koji S. Kawabata https://orcid.org/0000-0001-6099-9539
B.-C. Koo https://orcid.org/0000-0002-2755-1879
Woojin Kwon https://orcid.org/0000-0003-4022-4132
Shih-Ping Lai https://orcid.org/0000-0001-5522-486X
J.-E. Lee https://orcid.org/0000-0003-3119-2087
N. Lo https://orcid.org/0000-0002-4634-7304
Xing Lu https://orcid.org/0000-0003-2619-9305
Soojong Pak https://orcid.org/0000-0002-2548-238X
Geumsook Park https://orcid.org/0000-0001-8467-3736
Kate M Pattle https://orcid.org/0000-0002-8557-3582
K. Qiu https://orcid.org/0000-0002-5093-5088
John Richer https://orcid.org/0000-0002-9693-6860
M. Saito https://orcid.org/0000-0003-0769-8627
Takeshi Sakai https://orcid.org/0000-0003-4521-7492
Hiroko Shinnaga https://orcid.org/0000-0001-9407-6775
Dimitris Stamatellos https://orcid.org/0000-0002-4502-8344
D. Ward-Thompson https://orcid.org/0000-0003-1140-2761
Yao-Lun Yang https://orcid.org/0000-0001-8227-2816

References

Alves, J., Lombardi, M., & Lada, C. J. 2007, A&A, 462L, 17
André, P., Di Francesco, J., Ward-Thompson, D., et al. 2014, in Protostars and Planets VI, ed. B. Henrik et al. (Tucson, AZ: Univ. Arizona Press), 27
André, P., Men'shchikov, A., Bontemps, S., et al. 2010, A&A, 518, 102
Bacmann, A., Lefloch, B., Ceccarelli, C., et al. 2002, A&A, 389, L6
Bally, J., Langer, W. D., Stark, A. A., & Wilson, R. W. 1987, ApJ, 312, 45
Beckwith, S. V. W., Sargent, A. I., Chini, R. S., & Guesten, R. 1990, AJ, 99, 924
Bergin, E. A., & Tafalla, M. 2007, ARA&A, 45, 339
Berry, D. S. 2015, A&C, 10, 22
Berry, D. S., Reinhold, K., Jenness, T., & Economou, F. 2007, in ASP Conf. Ser. 376, Astronomical Data Analysis Software and Systems XVI, ed. R. A. Shaw, F. Hill, & D. J. Bell (San Francisco, CA: ASP), 425
Bintley, D., Holland, W. S., MacIntosh, M. J., et al. 2014, Proc. SPIE, 9153, 3
Busquet, G., Estalella, R., Zhang, Q., et al. 2011, A&A, 525, 141
Caselli, P. 2011, IAUS, 280, 19
Chandrasekhar, S., & Fermi, E. 1953, ApJ, 118, 116
Chapin, E. L., Berry, D. S., Gibb, A. G., et al. 2013, MNRAS, 430, 2545
Chen, M. C.-Y., Di Francesco, J., Johnstone, D., et al. 2016, ApJ, 826, 95
Contreras, Y., Garay, G., Rathborne, J. M., & Sanhueza, P. 2016, MNRAS, 456, 2041
Contreras, Y., Schuller, F., Urquhart, J. S., et al. 2013, A&A, 549, 45
Cox, N. L. J., Arzoumanian, D., André, P., et al. 2010, A&A, 590, 110
Csengeri, T., Weiss, A., Wyrowski, F., et al. 2016, A&A, 585, 104
Currie, M. J., Berry, D. S., Jenness, T., et al. 2014, in ASP Conf. Ser. 485, Astronomical Data Analysis Software and Systems XXIII, ed. N. Manset & P. Forshay (San Francisco, CA: ASP), 391
Dempsey, J. T., Friberg, P., Jenness, T., et al. 2013, MNRAS, 430, 2534
Di Francesco, J., Myers, P. C., Wilner, D. J., Ohashi, N., & Mardones, D. 2001, ApJ, 562, 770
Eden, D. J., Moore, T. J. T., Plume, R., et al. 2017, MNRAS, 469, 2163
Federrath, C. 2016, MNRAS, 457, 375
Federrath, C., & Klessen, R. S. 2013, ApJ, 763, 51
Feng, S., Beuther, H., Zhang, Q., et al. 2016, A&A, 592, 21
Fiege, J. D., & Pudritz, R. E. 2000, MNRAS, 311, 105
Fischera, J., & Martin, P. G. 2012, A&A, 542, A77
Gao, Y., & Solomon, P. M. 2004, ApJ, 606, 271
Garden, R. P., Hayashi, M., Hasegawa, T., Gatley, I., & Kaifu, N. 1991, ApJ, 374, 540
Giannetti, A., Wyrowski, F., Brand, J., et al. 2014, A&A, 570, 65
Goldsmith, P. F., Pineda, J. L., Langer, W. D., et al. 2016, ApJ, 824, 141
Holland, W. S., Bintley, D., Chapin, E. L., et al. 2013, MNRAS, 430, 2513
Inutsuka, S., Inoue, T., Iwasaki, K., et al. 2015, A&A, 580, 49
Inutsuka, S.-I., & Miyama, S. M. 1992, ApJ, 388, 392
Jackson, J. M., Finn, S. C., Chambers, E. T., Rathborne, J. M., & Simon, R. 2010, ApJL, 719, L185
Jenness, T., Chapin, E. L., Berry, D. S., et al. 2013, SMURF: SubMillimeter User Reduction Facility, Astrophysics Source Code Library, ascl:1310.007
Jiménez-Serra, I., Caselli, P., Tan, J. C., et al. 2010, MNRAS, 406, 187
Johnstone, D., Di Francesco, J., & Kirk, H. 2004, ApJ, 611L, 45
Johnstone, D., Wilson, C. D., Moriarty-Schieven, G., et al. 2000, ApJ, 545, 327
Juvela, M., Demyk, K., Doi, Y., et al. 2015a, A&A, 584, 94
Juvela, M., He, J., Pattle, K., et al. 2017, A&A, in press (arXiv:171109425J)
Juvela, M., Ristorcelli, I., Marshall, D. J., et al. 2015b, A&A, 584, 93
Juvela, M., Ristorcelli, I., Pagani, L., et al. 2012, A&A, 541, 12
Juvela, M., Ristorcelli, I., Pelkonen, V.-M., et al. 2011, A&A, 527, 111
Kainulainen, J., Stutz, A. M., Stanke, T., et al. 2017, A&A, 600, 141
Kang, M., Choi, M., Stutz, A. M., & Tatematsu, K. 2015, ApJ, 814, 31
Kauffmann, J., & Pillai, T. 2010, ApJL, 723, L7
Kennicutt, R. C., Jr. 1998, ApJ, 498, 541
Kirk, H., Johnstone, D., & Di Francesco, J. 2006, ApJ, 646, 1009
Kirk, H., Myers, P. C., Bourke, T. L., et al. 2013, ApJ, 766, 115
Klessen, R. S. 2000, ApJ, 535, 869
Könyves, V., André, P., Men'shchikov, A., et al. 2010, A&A, 518, 106
Könyves, V., André, P., Men'shchikov, A., et al. 2015, A&A, 584, 91
Kritsuk, A. G., Norman, M. L., & Wagner, R. 2011, ApJL, 727, L20
Lada, C. J., Lombardi, M., & Alves, J. F. 2010, ApJ, 724, 687
Lee, J.-E., Bergin, E. A., & Evans, N. J., II 2004, ApJ, 617, 360
Li, G.-X. 2017, MNRAS, 465, 667
Li, G.-X., Urquhart, J. S., Leurini, S., et al. 2016, A&A, 591, A5
Li, P. S., Klein, R. I., McKee, C. F., et al. 2018, MNRAS, 437, 4220
Lin, Y., Liu, H. B., Dale, J. E., et al. 2017, ApJ, 840, 22
Lin, Y., Liu, H. B., Li, D., et al. 2016, ApJ, 828, 32
Liu, H. B., Galván-Madrid, R., Jiménez-Serra, I., et al. 2015, ApJ, 804, 37
Liu, H.-L., Li, J.-Z., Wu, Y., et al. 2016, ApJ, 818, 95

Liu, H.-L., Wu, Y., Li, J., et al. 2015, ApJ, 798, 30
Liu, T., Kim, K.-T., Yoo, H., et al. 2016a, ApJ, 829, 59
Liu, T., Lacy, J., Li, P. S., et al. 2017, ApJ, 849, 25
Liu, T., Wu, Y., Mardones, D., et al. 2014, PKAS, 30, 79L
Liu, T., Wu, Y., Wu, J., Qin, S.-L., & Zhang, H. 2013a, MNRAS, 836 1335
Liu, T., Wu, Y., & Zhang, H. 2012a, ApJS, 202, 4
Liu, T., Wu, Y., & Zhang, H. 2013b, ApJL, 775, L2
Liu, T., Wu, Y., Zhang, H., & Qin, S.-L. 2012b, ApJ, 751, 68
Liu, T., Zhang, Q., Kim, K.-T., et al. 2016b, ApJS, 222, 7
Liu, T., Zhang, Q., Kim, K.-T., et al. 2016c, ApJ, 824, 31
MacLaren, I., Richardson, K. M., & Wolfendale, A. W. 1988, ApJ, 333, 821
Mairs, S., Johnstone, D., Kirk, H., et al. 2015, MNRAS, 454, 2557
Mairs, S., Lane, J., Johnstone, D., et al. 2017, arXiv:170601897M
Meng, F., Wu, Y., & Liu, T. 2013, ApJS, 209, 37
Molinari, S., Swinyard, B., Bally, J., et al. 2010, A&A, 518, L100
Montier, L. A., Pelkonen, V.-M., Juvela, M., Ristorcelli, I., & Marshall, D. J. 2010, A&A, 522, 83
Montillaud, J., Juvela, M., Rivera-Ingraham, A., et al. 2015, A&A, 584, 92
Moore, T. J. T., Plume, R., Thompson, M. A., et al. 2015, MNRAS, 453, 4264
Motte, F., Andre, P., & Neri, R. 1998, A&A, 336, 150
Myers, P. C., Mardones, D., Tafalla, M., Williams, J. P., & Wilner, D. J. 1996, ApJL, 465, L133
Ormel, C. W., Paszun, D., Dominik, C., & Tielens, A. G. G. M. 2009, A&A, 502, 845
Ostriker, J. 1964, ApJ, 140, 1056
Pagani, L., Lefèvre, C., Juvela, M., Pelkonen, V.-M., & Schuller, F. 2015, A&A, 574, L5
Planck Collaboration, Ade, P. A. R., Aghanim, N., et al. 2011a A&A, 536, 22
Planck Collaboration, Ade, P. A. R., Aghanim, N., et al. 2011b A&A, 536, 23
Planck Collaboration, Ade, P. A. R., Aghanim, N., et al. 2016, A&A, 594, A28
Palmeirim, P., André, P., Kirk, J., et al. 2013, A&A, 550, 38
Peretto, N., André, P., Könyves, V., et al. 2012, A&A, 541, 63
Peretto, N., & Fuller, G. A. , 2009, A&A, 505, 405
Peretto, N., Fuller, G. A., Duarte-Cabral, A., et al. 2013, A&A, 555, 112
Piazzo, L., Calzoletti, L., Faustini, F., et al. 2015, MNRAS, 447, 1471
Rivera-Ingraham, A., Ristorcelli, I., Juvela, M., et al. 2016, A&A, 591, 90
Rivera-Ingraham, A., Ristorcelli, I., Juvela, M., et al. 2017, A&A, 601, 94
Sadavoy, S. I., Di Francesco, J., Johnstone, D., et al. 2013, ApJ, 767, 126
Sanhueza, P., Jackson, J. M., Foster, J. B., et al. 2012, ApJ, 756, 60
Sanhueza, P., Jackson, J. M., Foster, J. B., et al. 2013, ApJ, 773, 123
Schmidt, M. 1959, ApJ, 129, 243
Schneider, N., Bontemps, S., Girichidis, P., et al. 2015, MNRAS, 453, 41
Schneider, N., Csengeri, T., Hennemann, M., et al. 2012, A&A, 540, L11
Shirley, Y. L. , 2015, PASP, 127, 299
Stephens, I. W., Jackson, J. M., Whitaker, J. S., et al. 2016, ApJ, 824, 29
Stodólkiewicz, J. S. 1963, AcA, 13, 30
Tatematsu, K., Liu, T., Ohashi, S., et al. 2017, ApJS, 228, 12
Van der Tak, F. F. S., Black, J. H., Schöier, F. L., Jansen, D. J., & van Dishoeck, E. F. 2007, A&A, 468, 627
Vázquez-Semadeni, E. 1994, ApJ, 423, 681
Wang, K., Testi, L., Burkert, A., et al. 2016, ApJS, 226, 9
Wang, K., Testi, L., Ginsburg, A., et al. 2015, MNRAS, 450, 4043
Wang, K., Zahorecz, S., Cunningham, M. R., et al. 2018, RNAAS, 2, 2
Wang, K., Zhang, Q., Testi, L., et al. 2014, MNRAS, 439, 3275
Wang, K., Zhang, Q., Wu, Y., & Zhang, H., 2011, ApJ, 735, 64
Ward-Thompson, D., Di Francesco, J., Hatchell, J., et al. 2007, PASP, 119, 855
Wilson, T. L., & Rood, R. 1994, ARA&A, 32, 191
Wu, J., Evans, N. J., II, Gao, Y., et al. 2005, ApJL, 635, L173
Wu, J., Evans, N. J., II, Shirley, Y. L., et al. 2010, ApJS, 188, 313
Wu, Y., Liu, T., Meng, F., et al. 2012, ApJ, 756, 76
Yuan, J., Li, J.-Z., Wu, Y., et al. 2018, ApJ, 852, 12
Yuan, J., Wu, Y., Liu, T., et al. 2016, ApJ, 820, 37
Zhang, Q., Wang, K., Lu, X., et al. 2015, ApJ, 804, 141
Zhang, T., Wu, Y., Liu, T., et al. 2016, ApJS, 224, 43
Zhang, Z.-Y., Gao, Y., Henkel, C., et al. 2014, ApJL, 784, L31